Novel catalyst materials for the cathode side of MEAs suitable for transportation applications				
G.A. 303492				08.08.2016
Deliverable **D1.12**	WP1	**Coordination and project management**		
Deliverable: Review Paper on the project outcome				
Description of Deliverable: Submission of a review paper on the state of the art of cathode catalyst at the end of the project, mainly focussing on the progress accomplished by the project				
PM for D1.12: 1+1	Nature: O	Dissemination Level: PU	Delivery Date: 31.12.2016	Lead Beneficiary: TUM

Relevant Sections from Description of Work

"Besides the purpose of updating the consortium, the information shall be summarized by a joint review paper by the consortium members in a scientific journal like "Fuel Cells". "

"Publication of a second, final review paper that focusses entirely on the progress in the field obtained during the contract period, and especially summarizes in detail the output of the project;"

Description of the work done

The literature was repeatedly searched for new important papers on ORR. An initial literature review was carried out early in the project (D3.1). Later this was continued and the paper draft was extended. At some point it was decided to focus more, especially in light of the multitude of review articles in the field. As the CathCat results alone might not be supporting a review paper, the project manager was asked for permission to merge the two planned reviews into a single one. A paper draft entitled "Pt-rare earth alloy catalysts and advanced support materials for Electrocatalysis of the Oxygen reduction reaction" has been prepared and was submitted

Pt-rare earth alloy catalysts and advanced support materials for electrocatalysis of the oxygen reduction reaction

Journal:	*Fuel Cells*
Manuscript ID	Draft
Wiley - Manuscript type:	Review
Date Submitted by the Author:	n/a
Complete List of Authors:	Schneider, Oliver; Technische Universitat Munchen, Institute of Informatics VI Escudero-Escribano, Maria; Danmarks Tekniske Universitet, Center for Individual Nanoparticle Functionality (CINF), Department of Physics Mostafa, Ehab; Technische Universitat Munchen, Institute of Informatics VI; Mansoura University, Chemistry Department, Faculty of Science Durante, Christian; Universita degli studi di Padova Scuola di Scienze, Department of Chemical Sciences and INSTM UNIT Velázquez-Palenzuela, Amado; Danmarks Tekniske Universitet, Center for Individual Nanoparticle Functionality (CINF), Department of Physics Martens, Sladjana; Technische Universitat Munchen, Institute of Informatics VI Ju, Wenbo; Technische Universitat Munchen, Institute of Informatics VI; Technische Universitat Munchen, Physik-Department Asen, Ludwig; Technische Universitat Munchen, Institute of Informatics VI; Technische Universitat Munchen, Fakultaet fuer Chemie Lindahl, Niklas; Chalmers University of Technology, Physics Department Luo, Yun; Universite de Poitiers UFR Sciences Fondamentales et Appliquees, IC2MP, UMR-CNRS feng, ligang; Chalmers University of Technology, Department of Physics Gennaro, Armando; Universita degli studi di Padova Scuola di Scienze, Department of Chemical Sciences and INSTM UNIT Seidl, Lukas; Technische Universitat Munchen, Institute of Informatics VI; Technische Universitat Munchen, Physik-Department Liang, Yunchang; Technische Universitat Munchen, Institute of Informatics VI; Technische Universitat Munchen, Physik-Department Wickman, Björn; Chemical Physics, Physics Department Langhammer, Christoph; Chalmers University of Technology, Physics Department Rizzi, Gian; Universita degli studi di Padova Scuola di Scienze, Department of Chemical Sciences and INSTM UNIT Tsotridis, Georgios; Institute for Energy and Transport Cerri, Isotta; Toyota Motor Europe NV/SA Grot, Stephen; Ion Power, Inc. Rossmeisl, Jan; Danmarks Tekniske Universitet, Center for Atomic Scale Materials Design (CAMD), Department of Physics; Kobenhavns Universitet Niels Bohr Instituttet, Nano-Science Center, Department of Chemistry

	Daletou, Maria; Institute of Chemical Engineering and High Temperature Chemical Processes-Foundation for Research and Technology, Neophytides, Stelios; Institute of Chemical Engineering and High Temperature Processes Alonso-Vante, Nicolas; Univ. Poitiers, UMR-CNRS 6503 Stephens, Ifan; Technical University of Denmark, Physics Granozzi, Gaetano; Universita degli studi di Padova Scuola di Scienze, Department of Chemical Sciences and INSTM UNIT Chorkendorff, Ib; Technical University Denmark, Physics Stimming, Ulrich; Newcastle University, School of Chemistry; Technische Universitat Munchen, Physik-Department
Keywords:	Platinum, rare earths, Electrocatalyst, catalyst support, Ionic Liquids, Electrodeposition, catalyst testing

Pt-rare earth alloy catalysts and advanced support materials for electrocatalysis of the oxygen reduction reaction

O. Schneider[1,*], M. Escudero-Escribano[2], E. Mostafa[1,3,4], C. Durante[5], A. Velázquez-Palenzuela[2], S. Martens[1], W. Ju[1,6], L. Asen[1,7], N. Lindahl[8], Y. Luo[9], L. Feng[8], A. Gennaro[5], L. Seidl[1,6], Y. Liang[1,6], B. Wickman[8], C. Langhammer[8], G.A. Rizzi[5], G. Tsotridis[10], I. Cerri[11], S. Grot[12], J. Rossmeisl[13], M. Daletou[14], S. Neophytides[14], N. Alonso-Vante[9], I.E.L. Stephens[2], G. Granozzi[5], I. Chorkendorff[2], U. Stimming[6, 15]

[1] Institut für Informatik VI, Electrochemical Research Group, Technische Universität München, Schleißheimerstraße 90a, 85748 Garching, Germany

[2] Center for Individual Nanoparticle Functionality, Department of Physics, Technical University of Denmark, 2800 Lyngby, Denmark

[3] current address: Institut für Physikalische und Theoretische Chemie, Universität Bonn, Römerstraße 164, 53117 Bonn, Germany

[4] permanent address: Chemistry Department, Faculty of Science, Mansoura University, 35516 Mansoura, Egypt

[5] Department of Chemical Sciences and INSTM UNIT, University of Padova, Via Marzolo 1,35131 Padova, Italy

[6] Physik-Department, Technische Universität München, James-Franck Straße 1, 85748 Garching, Germany.

[7] Fakultät für Chemie, Technische Universität München, Lichtenbergstraße 4, 85748 Garching, Germany

[8] Department of Physics, Chalmers University of Technology, SE-412 96, Goteborg, Sweden

[9] IC2MP, UMR-CNRS 7285, University of Poitiers 4 rue Michel Brunet, 86022 Poitiers, France

[10] Joint Research Centre-European Commission, Institute for Energy and Transport, 1755 LE Petten, Netherlands

[11] Toyota Motor Europe, Hoge Wei 33, 1930 Zaventem, Belgium

[12] Ion Power Inc., Governor Lea Road, New Castle, DE-19720, USA

[13] Nano-Science Center, Department of Chemistry, University of Copenhagen, 2100 Copenhagen, Denmark

[14] Foundation of Research and Technology, Hellas-Institute of Chemical Engineering and High Temperature Processes, Stadiou Str, Platani Rion, P.O. Box 1414, Patras GR-26504, Greece

[15] School of Chemistry, Bedson Building, Newcastle University, Newcastle upon Tyne NE1 7RU, United Kingdom

[*] Corresponding author: oliver_m.schneider@tum.de

Abstract

Electric mobility is a key technology for future sustainable transport. Battery and fuel cell vehicles have been introduced into the market, but have not reached a wide market penetration. Both technologies suffer from high cost and limited recharging / refueling infrastructure. Fuel cell vehicles have the advantages of larger cruising range and fast refueling. However, due to the sluggish kinetics of the oxygen reduction reaction (ORR), they contain large amounts of platinum, which represents a significant cost factor in mass production, apart from availability problems. Therefore, there are large research efforts to improve the understanding of the ORR at Pt and other materials, and to develop better catalysts. Recently, platinum-rare earth metal alloys were shown to demonstrate a much higher mass activity than pure platinum. These materials are interesting for actual fuel cells, provided they can be mass-produced at reasonable cost. In this review, the preparation and electrochemical properties of these materials are discussed. In addition, some key aspects of the state of the art of ORR electrocatalysis in PEM fuel cells, newer approaches for enhancing catalyst stability and activity, the use of advanced support materials and aspects of catalyst testing using the rotation disc electrode are briefly summarized.

Keywords: Platinum, rare earths, electrocatalysis, catalyst support, ionic liquids, electrodeposition, catalyst testing

1 Introduction

The increasing industrialization and development of many countries will lead to an increase in the world's energy demand in the next few decades. Based on an estimation from the U.S. Energy Information Administration, the total energy consumption will increase from 580 EJ in 2012 to 860 EJ in 2040 [1]. Given the limited oil resources and environmental issues there is therefore a strong need for sustainable transport modes. This can only be accomplished by electrically driven vehicles as stated by Wagner et al. [2]. For electrical driving one approach is based on rechargeable battery-powered vehicles, a technology strongly supported by many governments and pursued by most car manufacturers. However, current day battery technology – and the one of the years to come – suffers from the low energy density of the batteries, leading either to an extremely heavy battery or limited driving range of about 200 km [2, 3]. In addition, the battery costs are high: these factors slow down the wide range release of electric vehicles into the market. Fuel cells driven cars, on the other hand, allow much larger driving ranges, even though they also suffer from still high prices, the sparse refueling infrastructure and unsolved issues regarding the sustainable production of hydrogen and its storage. However, the cost for the fuel cell system will be significantly cut down by mass production, once the refueling technology is set up [3]. The research into fuel cells is not only an academic exercise. All large car manufacturers explore the development of next generation fuel cell cars, and are very active in this field. Hyundai and Toyota have released fuel cell cars produced in series [4]. A more detailed comparison of the advantages and disadvantages of battery and fuel cell driven cars was recently published by Gröger et al. [3].

With respect to cost, once manufactured in large scale, the platinum content in the low temperature proton exchange membrane fuel cells becomes an important issue [3]. In state of the art technology, the Pt loading at the cathode is with 0.4 mg cm^{-2} much larger than at the anode where 0.05 mg cm^{-2} might suffice [3, 5]. The total loading according to US Department of Energy (DOE) is 0.15-0.2 g Pt kW^{-1} [6-8] electric power, which however refers to nanostructured thin film (NSTF) type catalysts. Nanoparticle (NP) based catalysts are characterized by much higher loadings [5]. The fuel cell vehicle from Toyota has a loading of 0.26 g Pt kW^{-1} maximum power based on published Pt content [9] and the output power of the vehicle. The current cost of a fuel cell system, extrapolated to conditions of mass production, would amount to 55 \$ kW^{-1} net power, and the DOE target for 2020 is 40 \$ kW^{-1} [8]. Additional targets concern peak energy efficiency (65% 2020, 70% ultimate) and durability in an automotive drive cycle (5000 h) [8].

The major reason for the higher Pt loading at the cathode is the sluggish kinetics of the oxygen reduction reaction (ORR) [3, 10-13]. In the past 15 years, theoretical density functional theory (DFT) calculations and experiments on model systems strongly improved the understanding of the physical origins of the slow kinetics and allowed to calculate potential-dependent free energy diagrams considering all reaction intermediates formed [10, 11, 14-21] and in part even the free energies of the transition state (e.g. see Figure 1) [11, 17, 22]. The complete reduction of oxygen to water requires the transfer of four electrons and protons to the oxygen molecule. This process can take place serially (associative mechanisms, responsible also for hydrogen peroxide (H_2O_2) formation as side product for some metals) or can involve a dissociation step of adsorbed oxygen (dissociative mechanism) [10]. Depending on the metal and the applied potential, these mechanisms can occur in parallel [11]. In all cases, intermediate species like OH and OOH radicals are bound via the oxygen atom to the surface of the catalyst. The binding interaction

between the ORR intermediates and the metal catalyst determines the reaction rate and thus the activity of the catalyst [15, 16]. Differences in reactivity between different transition metals are mainly due to the contribution of the metal d-band to the interaction [23, 24]. The energy of the d-band center relative to the Fermi energy can be changed by altering the lattice constant of the metal layer, e.g. by introducing strain in the layer (pseudomorphic overlayers), or by altering the coordination number (different crystal facets) [20, 25-30]. The electronic structure of the metal also can be changed by direct electronic interaction with a second metal (surface alloy, overlayer of e.g. Pt on a second metal), resulting in the so-called ligand effect [15, 24, 25]. For the ORR, if the binding is too weak, the reaction step leading to the intermediate will be uphill in the free energy, while if it is too strong, the reaction step consuming the intermediate is uphill [10, 11, 16]. In both cases, a thermodynamic barrier for the overall reaction results, slowing down the reaction significantly [10, 11]. An ideal catalyst would have optimized binding interactions with all the intermediates. However, it was shown that no metallic two-dimensional material can be an ideal catalyst, as the binding strength of the different intermediates is correlated due to the similarity of the functional group bound to the surface [18, 23, 31]. A plot of the activity of different catalysts versus a single descriptor like the binding energy of an oxygen atom therefore results in a curve with a maximum at intermediate binding energies, the so-called volcano plot [10, 15, 16, 18]. Volcano plots have been used for a long time in catalysis, but were previously to the mentioned DFT work based on experimental descriptors like the sublimation enthalpy of the metal or adsorption enthalpies [32, 33]. From all the pure metals, platinum is closest to but not at the maximum of the volcano [10]. In more recent work, also the water molecules present on the surface and the OH coverage have been considered in the calculations [17].

However, this is only part of the story, and a number of studies have been carried out to shed additional light on the fundamentals determining the actual performance of catalyst nanoparticles. The activity of Pt nanoparticles is much lower than for extended area Pt samples, and the activity of the nanoparticles cannot simply be calculated by knowledge of the relative amount of differently oriented facets [34, 35]. The activity at defects sites was shown not to depend only on the immediate coordination number, but also on the second coordination sphere [30]. There are many in part contradictory studies on particle size effects for Pt, which is in part due to the use of samples with a wider particle size distribution, and to changes in the catalyst during testing [12, 21, 35-42]. Shape-controlled nanoparticles have been synthesized and tested, but during actual fuel cell operation there is a high chance that the shape is altered to attain the most stable one [21, 36, 43-48]. Pt and Pt NP show a rather complicated dissolution behavior, and the majority of the degradation often takes place when surface oxide present is again reduced, if the oxide has been exposed to potentials high enough to allow for place exchange between Pt and oxygen atoms [49, 50]. Impurities and spectator species have a significant impact both on performance and stability of the catalysts [51-57].

The problem of the large overpotential for the ORR and the large amount of catalyst therefore needed is addressed by two main routes of approaches: the development of noble metal-free catalysts and the use of reduced amounts of noble metal alloys [58-63]. In the latter case, different strategies can be pursued in order to reduce the amount of Pt metal required for a large oxygen reduction rate at small overpotentials: one of them is the use of Pt alloys with an activity larger than for pure Pt. The alloying can alter the interaction with the ORR intermediates and in turn enhance the overall reaction rate [5, 15, 64-67]. In many cases such alloys form a thin skin layer of Pt at the surface due to surface segregation and/or electrochemical dealloying processes

[67-73]. Examples for such alloys are the well-known and highly active Pt_3Ni and other Pt-transition metal alloys [68-70, 74-82], including the recently discussed nanoframes [83-85], but especially alloys between Pt and rare earth metals [5, 64, 86-94]. These approaches lead to catalysts closer to the maximum of the volcano plot. Another frequently employed method is the deliberate formation of core-shell compounds, where Pt is deposited on nanoparticles from a different pure metal or alloy [95-102]. A reduction in the total amount of catalyst required can also be obtained by thin film catalysts instead of nanoparticles [103-105].

Aside from research into more active catalyst materials, also advanced support materials are studied intensively [106-117]. On the one hand, the standard support carbon tends to corrode, especially at the cathode during operation at open circuit potential (OCP) and during start/stop cycles [106, 108, 118, 119]. Thermodynamically, carbon is not stable at typical cathode potentials. Support corrosion may be prevented by using other conductive materials, like different types of oxides and oxide-carbon composites [106, 115, 116, 120-127]. On the other hand, a beneficial electronic interaction between catalyst and support might cause a further increase in catalytic activity, and maybe even beat the maximum of the volcano. In that regard, also chemically modified carbon supports, *i.e.* doped carbons, and graphene-derived compounds, are under investigation [108, 110-114, 128-131].

In Europe, the Fuel Cells and Hydrogen Joint Undertaking (FCH JU), a Joint Technology Initiative of the European Commission, Industrial Companies and Research Institutions active in the field is pushing towards overcoming the obstacles towards widespread market introduction of fuel cell technologies. In their most recent multi-annual work plan, they set by 2023 ambitious targets for cost (75 € kW^{-1} for 100.000 number of units), tank to wheel efficiency (48%), and

lifetime (7000 h, all for passenger cars) [132]. Among other activities, they fund a portfolio of European research and development projects. Several of those aim at improving membrane electrode assembly (MEA) components and especially at a reduced noble metal content. One of them was the CathCat[1] project, in which the authors of the current paper collaborated in the research on alloys of Pt and Pd with rare earth elements as electrocatalyst for fuel cells and on advanced catalyst support materials.

The focus of this review is to summarize some of the most recent developments in the area of electrocatalysis of the oxygen reduction reaction, including results from the CathCat project. As several excellent reviews about the topic have been published in recent years, this review will discuss shortly some fundamental issues, only briefly mention recent activities in the area of Pt-transition alloy catalysts, and then focus entirely on the preparation of Pt-rare earth electrocatalysts and their prospects for fuel cell applications. A short section will also deal with advanced support materials. Another important topic in electrocatalysis, the reliable characterization of catalysts, will be discussed in the end.

[1] Full project title: Novel catalyst materials for the cathode side of MEAs suitable for transportation applications

2 Overview of recent review articles

Stephens et al. reviewed the ORR electrocatalysis of Pt and Pt alloys [5]. Starting from a quantitative consideration of the annual production of Pt and the current amount required for a 100 kW fuel cell, they demonstrate that only a limited number of fuel cell cars could be built under these constraints, and review briefly the historical development of Pt alloy research. Afterwards, they explain in detail the theoretical description of the catalytic activity based on the free energy of the different ORR intermediates and their dependency on applied potential, resulting in volcano plots. In order to improve the ORR activity towards the top of the volcano while reducing the Pt loading at the cathode, researchers have extensively investigated Pt-alloys during the last decades. The effect of alloying Pt is to weaken the OH binding energy, by modifying the electronic properties of the Pt surface by means of ligand or strain effects [24, 25, 27, 29, 133, 134]. Pt-Cu systems have been used to study both effects. In particular, by changing the subsurface coverage of Cu on Cu/Pt(111) near surface alloys (NSAs), the OH binding energy can be tuned by ligand effects, resulting in a volcano [65].

Stephens et al. addressed the subject of how to improve the ORR performance of nanoparticulate catalysts which could be actually used in PEMFC. For pure Pt catalysts they described the well-known particle size dependence of both activity and stability, explained in terms of the increase of the fraction of uncoordinated Pt sites as the particle size decreases. The contribution of such sites to the ORR activity is considered negligible, since they will adsorb HO* more strongly than the terraces, and only nanoparticles larger than ~10 nm are predicted to approach the specific activity of bulk Pt. Consequently, the maximum mass activity is expected for ~3 nm Pt catalysts, as derived from the model of Tritsaris et al. [39] and the experimental results of Gasteiger et al.

[12]. Regarding stability, the authors also detailed that Pt dissolution is more favored in the case of small nanoparticles (below 4 nm), given the lower average cohesive energy relative to bulk Pt, and is specially triggered when reaching high potentials, which induces surface roughening and sub-surface oxide formation.

Regarding the performance on nanoparticulate Pt alloys in proton exchange membrane fuel cells (PEMFCs), up to a 4-fold mass activity increase could be reached with Pt-late transition metal alloy nanoparticles in fuel cell configuration. A common trend for both Pt_xCu/C and Pt_xCo/C catalysts, as well as Pt/C, is that the stability could be improved by annealing at high temperature (~900^{o}C), which causes particle sintering and surface smoothing that reduce the fraction of uncoordinated sites. In the case of the alloy catalysts the main cause of diminution of specific activity is the dealloying of the non-noble metal, as consequence of the cathode potential significantly exceeding the dissolution potential of the bulk solute metal. The authors conclude that the leaching process depends on the diffusivity of the non-noble metal, the thickness and integrity of the Pt-overlayer, and the interaction between O* and HO* with subsurface non-noble metal atoms. Then, Stephens et al. describe different approaches to improve the performance of Pt-alloy nanoparticles, by optimizing the morphology, developing oriented nanoparticles, core-shell nanoparticles and hollow nanoparticles. Finally, they discuss the challenges for synthesis and implementation of Pt alloys with rare earth metals as nanoparticulate catalysts.

Rabis and co-authors also gave an excellent overview of the progress in the area of PEMFCs in the last 15 years [135]. In the introduction, they also provided a table with target specifications for applications in the different areas. Their paper is organized in sections regarding activity for both alcohol oxidation and oxygen reduction reactions, catalyst stability, and new materials.

In the section about ORR, the general mechanism according to the four and two electron pathways is summarized. It is mentioned that it is likely that the mechanism takes place via the associative mechanism, in which adsorbed molecular oxygen accepts electron and a proton, instead of via the dissociative mechanism, where the oxygen molecule would dissociate into atoms in the first step. The order of reactivity of the different crystallographic faces for Pt single crystals is given for $HClO_4$ and H_2SO_4, taken from the work of Markovic et al. [136]. In both cases the (110) facets are the most reactive. The important role of spectator species like adsorbed OH groups or adsorbed bisulfate ions on the reaction kinetics is emphasized. For Pt alloys, the different influence factors are summarized. One effect concerns the d-band vacancy mechanism, where the alloying with early transition elements creates vacancies in the d-band that in turn causes a weakening of the oxygen-oxygen bond (basically a consequence of the direct electronic interaction between Pt and the alloying element, and thus corresponding to the ligand effect). Other effects are the balancing of the binding strength of the different intermediates that can be manipulated by shifting of the center of the d-band (i.e. strain effect). In addition the surface coverage by spectator species plays a role and here, additives preventing adsorption of such species can accelerate the reaction. Some works on Pt-Ni and Pt-Co are reviewed. The importance of the composition of the first few layers is emphasized. The role of skin structures, also for alloy nanoparticles, and nanoparticles expressing certain facets are shortly touched.

In the section about Stability, the authors emphasize the importance of stability testing under technologically relevant conditions. They discuss carbon corrosion and active area loss of the catalyst as major contributing factor to fuel cell degradation. A large part is dedicated to the start-stop-cycle mechanism and the approaches for its mitigation.

The section on new materials first focusses on the NSTF catalysts, correlating its improved specific and mass activity to the morphology of the catalysts. Newer results claiming that the mass activity would not show a maximum at a certain particle size are discussed in that paragraph as well. In that context, the shift in the potential of zero charge to lower values for smaller particle size is taken as an explanation. The remainder of the chapter deals with nonprecious metal based catalysts like metal chalcogenides, but also N-doped carbons (with metal impurities), and organometallic catalysts. The latter field, based on e.g phthalocyanines and other macrocycles with N-active centers, has resulted lately in catalysts with a performance not so much worse than Pt/C catalysts. Finally, the search for improved support materials is thematized.

Wu and Yang reviewed different types of pure Pt catalysts as well as several binary alloys including core/shell catalysts [137]. They showed that Pt nanoparticles with high index facets (e.g. (730)) have a higher activity than particles with (100) and (111) facets due to a larger number of corner and edge atoms and an exponentially increasing reaction rate. The activity of bimetallic catalysts like Pt_3Ni increases with increasing percentage of exposed (111) facets. These bimetallic catalysts were synthesized with CO gas using a procedure described in [138], that is similar to the carbonyl method [139]. Due to strain effects icosahedral bimetallic nanocrystals have an even higher activity, also compared to octahedral nanocrystals. The mass activity of bimetallic nanocrystals also depends highly on the size of the crystals, because of different surface to volume ratios. Core-shell structured nanoparticles with a core consisting of Ag, Au, Cu or Pd and a Pt shell, created by wet chemistry synthesis have a much better ORR activity with respect to the mass of the Pt. When core and shell consist of metal alloys analog results are mentioned. A $FePt_3$ shell surrounding Au is reported as a highly active and durable catalyst. Preparation techniques are described. Also porous structures like PtPd nanotubes reduce

the Pt consumption, can be used as self-supporting catalyst and have promising activity and stability properties.

The review of Porter et al. focuses on Pt based bimetallic nanocrystals [140]. First different growth methods to obtain bimetallic nanocrystals and high index nanocrystals are summarized. It is shown, e.g., that the incorporation of Pd into a Pt nanocube shows maximum improvement of the catalytic activity when the cubes consist of 40-60% of Pt. For the octahedral Pt_3Ni the mass and specific ORR activity is several times higher than of Pt_3Ni nanocubes and even higher compared to Pt nanocubes. The analogous behavior of Pt_3Co emphasized the strong shape dependency of the ORR activity. Porter et al. also summed up the dependency of the ORR activity on the reaction medium. In sulfuric acid (H_2SO_4) the order is Pt(111) < Pt(100) < Pt(110) due to bisulfate anion adsorption whereas in non-adsorbing perchloric acid ($HClO_4$) the order is Pt(100) < Pt(110) << Pt(111) and in KOH Pt(100) < Pt(110) < Pt(111). Bimetallic nanocrystals show the same medium-dependency, e.g. Pt-Mn nanocubes have a higher activity in H_2SO_4 than in $HClO_4$. The best catalytic ORR activity is shown by concave Pt nanocubes due to the high index facets, here (720), and hence the high number of edge and step atoms.

Wang et al. reviewed systematic studies on the effect of particle size, shape and composition of Pt alloy nanoparticles including synthesis techniques, focusing on Pt-Ni and Pt-Co particles [67]. Antolini reviewed the possible role of Ir in anode and cathode fuel cell catalysts [141].

The review by Guo et al. gives a broad overview on shape-controlled synthesis of Pt nanoparticles through binary, core-shell to Pt-free catalyst systems [142]. In the beginning the experimental procedures for electrochemical characterization of the catalysts are reviewed. Based

on the activity of Pt single crystals of different orientations it is derived that octahedral Pt nanoparticles should have a higher ORR activity than cubic ones in $HClO_4$, whereas the cubic nanoparticles show a higher activity in H_2SO_4. Also the enhanced activity of high index faces is emphasized. The key parameters for controlled synthesis of alloy nanoparticles consisting of Pt and an early transition metal are described in detail. The influence of transition metal type, composition, particle morphology and size is discussed. Again the (111) facets showed the highest activity in $HClO_4$. These alloys however are unstable due to dealloying. On the other hand, core-shell-structures, where a thin (around 1 nm) shell of pure Pt (or a Pt alloy) surrounds a core of a different material, represent the most durable and active catalysts. Different preparation methods and examples from the literature are discussed. With graphene as a support the efficiency and especially the durability of the catalyst can be improved further due to improved binding between support and nanoparticle and a resulting lower ORR overpotential compared to standard carbon supports. A better catalytic efficiency can also be reached, when the nanoparticle is covered by a shell of ionic liquid. Synthesized Pt-free catalysts M-N-C (M=Fe, Co) have a high durability and can reach overpotentials not much worse compared to Pt (60 mV). An additional approach for Pt-free catalysts is the use of metal nanoparticles on nano-carbon supports like N-doped carbon nanotubes. These systems exhibit good catalytic activities for the ORR, especially in alkaline solution, but the catalytic mechanism is not yet clear. In acid solutions a metal free N-doped carbon nanotube graphene system shows good catalytic activities for the ORR.

Hayden accounted with different examples including carbon monoxide (CO) electrooxidation and ORR on the effect of particle size and supports on their electrocatalysis [37]. For both reactions supported on Au and Pt, it was found that the catalytic activities decrease with decreasing particle size independent of the support material with a critical particle size between 2-3 nm. For ORR,

the presumed explanation is that small particles provide a high population of low coordination surface sites that more strongly adsorb hydroxyl species and consequently block the active sites and result in lower ORR catalytic activities. A considered example to replace the carbon-support normally used in the PEMFCs is to replace it with titania or Nb-doped titania. These are more stable and it was found that the ORR catalytic activity is a function of the degree of the Niobium doping of the oxide.

A comprehensive review of the recent progress in the development of Pt-Ni bimetallic ORR catalysts was reported recently [143]. The authors were able to explain how the size of the nanoparticle directly influence the undesired nanoporosity formation affecting the ORR activity and stability. This has been achieved by controlling the particle size to ca. 10 nm resulting in the formation of solid Pt(shell)-Ni(core) nanoparticles. This is important for retaining a high Ni content and consequently a high surface reactivity. Oeszalan et al. published a detailed review on binary Pt (alloy) core shell architectures covering different preparation techniques, structure, characterization techniques and stability [144]. Their work focused on late transition metals like Co, Ni, Cu and Au.

A very new review by Shao et al. discussed the latest advances in Pt and Pd electrocatalysis [145]. Especially alloys with late transition metals, and the preparation of core-shell and shape-selected alloys are treated in great detail. The effect of carbonyl compounds in affecting the particle shape and the consequences of introduction of a third metal are explained. Alloys with rare earth metals, which are the focus of this review, are only shortly treated. After non carbon support materials, non-noble metal and metal-free catalysts are treated extensively.

3 Fundamental aspects of ORR electrocatalysis including particle size effects

A wide variety of different types of Pt-based samples has been studied experimentally and theoretically in order to reach a better understanding of the ORR electrocatalysis. These span the entire range from low index plane single crystals [146-148], higher index single crystals with enlarged number of well-oriented step edges [20], defective single crystals [30], individual grains of polycrystalline Pt [149], polycrystalline Pt disks and wires [75, 150, 151], size-selected clusters and nanoparticles supported on e.g. glassy carbon [34, 150], shape selected nanoparticles [21, 43], and commercial Pt/C samples with different particle size and a rather large particle size distribution [12, 13, 56, 152]. In the following, selected key results from both theoretical and experimental recent studies on Pt and in part on Pd will be summarized. As will be seen, there has been significant progress in understanding of the ORR mechanism on Pt including the influence of coordination, particle size and shape, and chemical impurities, and of the dissolution behavior of Pt.

3.1 Pure Platinum and Palladium

One of the most comprehensive and critical discussions of the ORR at Pt single crystals was published 2014 by the group of Feliu, considering both theory and experiment [147], expanding earlier work [146, 148]. Their paper shows that the binding interaction of the ORR intermediates with the surface is not the only factor influencing the ORR kinetics and thus the catalytic activity of Pt. They pointed out that a pure binding interaction model is not able to predict correctly the activity of different facets of Pt: Opposite to the predicted Pt(111) in reality Pt(211) is the most active in acidic solution. Also coverage by oxide and hydroxide species, and surface charge (and

thus the potential of zero total charge - PZTC) alone do not suffice to complete the picture: "…adlayer structures and the relation between adsorbed water (H_2O_{ads}), water dissociation products, OH_{ads} or O_{ads}, and PtO oxide species coverage affect the whole energetics of the adsorption processes and may determine the surface reactivity" [147]. It is shown that the catalytic activity of Pt(111) is pH independent on the reversible hydrogen electrode (RHE) scale, while this is not the case for the other orientations. Even though the PZTC for Pt(111) does not show a strong pH dependence opposite to other orientations, the pH dependence alone cannot explain the trend, as especially vicinal surfaces like Pt(111) do not follow a general tendency. However, surfaces with low PZTC would show the highest ORR activity in acidic solutions. Based on the activity changes at single crystals of different orientations when cycling to rather high potentials (1.15 V or even 1.6 V), where Pt oxide species form and finally the surface order is destroyed at 1.6 V, the authors conclude that for (110) steps disordering increases the catalytic activity while for (100) steps it is decreased – the latter having direct impact for the catalytic activity of Pt nanoparticles. With respect to volcano curves the authors show that a critical parameter is the free energy of activation $\Delta G(E^0)$ of the rate determining step at the equilibrium potential. In that case the choice of the transfer coefficient, a change of surface charge at different potentials and the inclusion of double layer effects can lead to a significant decrease in $\Delta G(E^0)$ and therefore to a shift of the current-potential curves to more positive potentials. In addition, the authors question the statement from literature that the (111) facets would be most active on Pt nanoparticles and that defect sites like steps and kinks would have little contribution, as on stepped single crystals even in the absence of faceting or reconstruction an increase in ORR catalytic activity is observed. The inclusion of solvation and electric field effects can partially improve the theoretical predictions, but still a further refinement of the models is required. It is emphasized that there is also no simple correlation between oxygen species coverage and ORR

activity, but that also the exact speciation and the role of water at the surface are of importance. The authors further discuss the hydroxide adsorption and the evolution of the surface hydroxide and oxide layers at elevated potentials including the correlated electrochemical equilibria. It is pointed out that for steps, the potentials for OH_{ads} and O_{ads} formation are not yet known. The roles of hydrogen peroxide oxidation and reduction are considered. Finally, it is speculated that not all steps of the ORR reaction might be inner sphere reactions.

The activity of stepped Pt surfaces for the ORR in 0.1 $HClO_4$ has been analyzed by Bandarenka et al. [20]. From the analysis of the normal and integrated voltammograms of Pt(111) and stepped Pt[n(111)x(111)], Pt[n(111)x(100)], the authors correlated an increasing ORR activity with an increasing step density. The main reason for such a high activity is the destabilization of adsorbed hydroxyl intermediate at the adjacent terrace induced by strong binding of adsorbed oxygen at the steps. The authors supposed that the immediate reason for this effect is an interruption of the network of co-adsorbed water and OH. As deduced from the integrated CVs, a positive potential shift up to 0.9 V vs. RHE (for surfaces with n = 2) was observed implying the proposed destabilization. A low energy barrier required to oxidize the adsorbed hydroxyl to oxygen due to a weak adsorbed hydroxyl-water interaction (solvation) explained the absence of a current and charge plateau in the range of 0.85 V – 1 V vs. RHE at stepped Pt surfaces and the otherwise monotonical current and charge increase (cf. Figure 2). This interaction is presumably high in case of Pt(111) which explains the higher energy barrier required to oxidize the adsorbed hydroxyl to oxygen and consequently plateaus in the current and charge. The fact that nanoparticles do not show an enhanced ORR activity is explained with the size of the terraces too small to establish long range ordering in the adsorbate layers.

Calle-Vallejo and co-authors introduced a new methodology for the determination of active sites of heterogeneous catalysts [30]. They suggested the construction of "coordination activity plots" for a specific material and reaction. The main part of the paper focusses on Pt(111) and the ORR reaction. The authors introduced a new geometric descriptor $\overline{cn}$ by adding up the number of nearest neighbor atoms, each one multiplied with the number of its own nearest neighbors, normalized to the maximum number of nearest neighbors in the bulk. This corresponds to considering the impact of the second nearest neighbors on the reactivity. The two potential determining steps in the ORR reaction are the reduction of O_2 to *OOH (first proton-electron transfer step) and *OH to H_2O (the final electron transfer). The activity for the ORR reaction thus depends on the Gibbs free energy of these two steps, which depend linearly on the geometric descriptor $\overline{cn}$. After conversion to electrode potential, the plot of potential versus $\overline{cn}$ represents a coordination – activity plot, from which an optimum value of $\overline{cn}$ can be obtained (cf. Figure 3). The authors thus derived a design rule pointing out that enhanced Pt(111) sites must have an increased number of second nearest neighbors, so that $\overline{cn}$ approximates 8.3. By following this rule and using three different experimental techniques such as dealloying, galvanic replacement and electrochemical destruction, they introduced specific defects to Pt(111) leading to an activity enhancement by 3.5 times. However, only specific types of defects can fulfill the design rule, others lead to under-coordination. Therefore, the authors concluded that concave nanoparticles have higher activity than convex ones. Also for other materials, similar coordination-activity plots can be constructed, but the actual best $\overline{cn}$ is material-dependent. Thus the authors showed a pathway to achieve similar specific activities as by alloying by variation of the site geometry leading to more second-nearest neighbors as compared to Pt(111).

Chen et al. used a microcapillary based method in combination with electron backscatter diffraction in order to obtain orientation dependent activity trends from measurements on a polycrystalline Pt electrode [149]. Their data confirm measurements from single crystals, indicating that orientations closer to (110) have an enhanced activity. No significant increase in activity was found for grain boundaries. A direct comparison to RDE data is not possible as the proton concentration decreased too much at the interface during ORR.

The role of the three different pathways discussed in literature – associative, dissociative and the peroxo-mechanism- were reinvestigated by Katsounaros et al. by studying the effect of different adsorbates on both the ORR as well as the hydrogen peroxide reduction and oxidation [54]. Their studies revealed that hydrogen peroxide as a side product can always be detected under conditions where the hydrogen peroxide reduction reaction is strongly impeded by surface adsorbates, no matter whether it is adsorbed hydrogen in the hydrogen underpotential deposition (H_{UPD}) region or halide ions. Supported by theoretical calculations they proposed that the dissociation reaction of adsorbed peroxide is always fast, while the adsorption is slowed down by spectator species (cf. Figure 4). While oxygen can be more easily adsorbed in the presence of other adsorbates than peroxide its dissociation is impeded. The authors therefore suggest the possibility – without ruling out the other pathways - that the ORR reaction might always proceed via the peroxo mechanism, and whether hydrogen peroxide is detected depends on the ratio between its fast reduction and its spectator-dependent desorption rate.

Bonnet et al. performed a detailed kinetic analysis of the ORR based on both available experimental and first principles results [22]. Data for oxygen surface coverages in function of the enthalpic barrier at equilibrium and other electrode potentials were derived. The article shows

that the ORR proceeds mainly through the associative pathway with reduction of adsorbed O_2 to O_2H being the rate determining step. However, it was noted that below 0.8 V the dissociative pathway can become important and play a key role in poisoning the catalyst prior to steady state. This could be another reason (besides ligand and strain effect) for the improved activity in some Pt-alloys due to reduced surface poisoning by products from water splitting and oxygen dissociation. The free energy plots for both pathways are shown in Figure 1. The actual activation barriers were considered in addition to the purely thermodynamic barriers.

Kattel et al. used first principles DFT to study the strain effect on Pt(111) on binding energies of intermediates at different surface sites as well as the activation energies of reaction steps in different ORR pathways [28]. While the geometry of the bound species was unchanged, the authors confirmed the weaker binding of intermediates due to strain, caused by widening of the d-band and the resulting shift in d-band center. The activation energies for dissociation reaction steps in the ORR were found to increase with strain while the ones of the hydrogenation reactions were lowered. On strained surfaces the dissociative mechanism was found to be less probable, while both the associative mechanism and the HOOH dissociation mechanism were active. For the former the O hydrogenation reaction was obtained as rate determining step while for the latter it was the HOOH dissociation step. However, these studies were not carried out for different potentials.

The adsorption of electrolyte anions and impurities also has a large influence on both the OH adsorption reaction and the ORR. Attard et al. investigated the influence of electrolyte on cyclic voltammetry (CV) for single crystalline Pt and found that, in contrast to common belief, specific adsorption in $HClO_4$ was not negligible and strongest on Pt(111) [51], in agreement with previous

studies by Watanabe et al. on polycrystalline Pt [153-155]. They found that adsorption of perchlorate anions inhibited ORR and recommended the use of trifluoromethanesulphonic acid (TFMSA) to eliminate specific adsorption effects, as had been studied by Berná et al. [156]. In the paper by Omura et al. it was also shown that specific adsorption of perchlorate is larger on Pt skin alloys compared to normal Pt, resulting in a shift of the onset potential of oxygen species adsorption that is not correlated to a weaker binding [154]. The authors also claimed that a reduced coverage by oxygen species was not the reason for the enhanced activity of Pt skin alloys.

In the study by Strmcnik and co-authors, the influence of different kind of impurities on the catalytic behavior of different platinum single crystal surfaces and high surface area materials was studied [52]. The reactions studied were the ORR, hydrogen oxidation (HOR) and evolution reactions (HER) and CO oxidation. As impurities ions such as Cl^-, NO_3^- and Cu^{2+} present in (sub)-μM concentration in the supporting electrolytes, but also different surface defects present on metal surfaces were chosen. It was found that even trace amounts of impurities have a huge influence on chemical transformations at electrochemical interfaces. For the ORR on Pt(111) in commercial and purified perchloric acid, no difference was seen in rotating disc electrode (RDE) polarization curve measurements, but during potential step experiments, a significant ORR current decrease was obtained with time for the commercial acid. Commercial catalysts showed a similar deactivation in the presence of added chloride impurities. The authors suggested that only a complete understanding of the structure, the chemical nature of the electrochemical interfaces and of the influence of impurities can lead to full understanding of the catalytic activity.

Bandarenka et al. applied potentiodynamic electrochemical impedance spectroscopy under ORR conditions to a Pt(111) surface and combined these measurements with DFT [157]. The aim was to resolve discrepancies between the currents / charges seen in the cyclic voltammograms and the expectations from DFT for the formation of OH and O surface adsorbate structures. It was assumed that some processes taking place at the surface were too slow to be detected by CV. The authors suggested an equivalent circuit that was capable to describe the impedance spectra very well. Between 0.6 and 0.85 V apparently high values for double layer capacitance were observed, because the technique could not resolve a fast OH adsorption separately. Both a slow and a fast electrosorption process could be identified in addition to the contribution from ORR. The data pointed, together with DFT, to the presence of three different adsorbate structures, and showed that within the plateau region in the voltammogram between the peaks for OH and O adsorption, slow formation of O_{ads} can already take place.

For practical application in fuel cells also the stability of the catalyst is of crucial importance. For a long time some of the general catalyst and fuel cell degradation mechanisms at fuel cathodes have been known, including aspects like particle ripening, particle agglomeration, support corrosion and Pt redeposition inside the membrane [118, 119]. A correlation to certain operation conditions like open circuit, current reversal and load cycles has been made [118, 119]. Nevertheless, the fundamental aspects and mechanistic details of electrochemical Pt dissolution had not been understood until recently.

In order to enhance the knowledge on Pt dissolution, Topalov and co-authors studied the behavior of polycrystalline Pt by coupling a flow-through cell to an ICP-MS system [158]. Under potentiostatic as well as potentiodynamic conditions, different experimental parameters were

applied. For different upper potential limits used it was found that the amount of dissolved Pt increased from a non-detectable value at 1.05 V to 10 ngcm^{-2} cycle^{-1} at 1.8 V vs. RHE. Both anodic and cathodic dissolution of Pt was seen. The latter one increased with increasing upper potential limit and took place during the Pt oxide reduction process. It was much more severe than the anodic dissolution process, but only after polarization to potentials above 1.15 V vs. RHE, as then subsurface oxide can be formed. Potential step experiments indicated a rapid decay in Pt dissolution rate with time, but an increase when change to a different potential initiated changes in the surface. Based on the results, the start/stop period of the fuel cell operation was recognized as the main problem due to the possibility for the cathode part of the cell to be exposed to higher potentials that the operating ones. They should not exceed +1.1 V vs. RHE but as it still occasionally happens, potential changes should be performed as fast as possible to diminish the Pt dissolution.

A comprehensive study with various experimental conditions was conducted in order to examine further the mechanism of polycrystalline platinum dissolution in acidic electrolyte [50]. The influence of the overpotential for the ORR, the timescale of the experiments and the concentration of protons and anions in perchloric and sulfuric acid on platinum dissolution in potential cycling experiments were examined. With increasing overpotential for Pt oxide reduction at constant upper potential an increase in Pt dissolution is observed, but only in experiments where a change from an oxidized to a reduced Pt surface takes place. The faster the formed surface oxide is reduced the lower the amount of Pt dissolution. The onset potential for Pt dissolution remains the same on the RHE scale, indicating proton influence. The amount of anodically dissolved Pt does not depend on the pH, but the cathodically dissolved Pt increases strongly with acid concentration. The authors concluded that during oxidation at potentials larger

than 1.1 V, place exchange processes between Pt and O take place. The majority of the Pt atoms thus getting to the surface are then passivated by additional oxygen adsorption, while some, presumably already before oxidation lower coordinated Pt atoms dissolve. In the subsequent reduction process, a larger fraction of the place-exchanged Pt atoms dissolves, in competition with redeposition, which explains both pH and scanrate dependence.

In the study carried out by Cherevko et al. the dissolution of polycrystalline Pt as well as of nanoparticulate Pt (particle size 4.8 nm) was examined further in the potential range of fuel cell operation [49]. In the case when there was enough time for the accumulation of Pt ions by applying first stagnant conditions for a fixed duration of time before turning on the flow to transfer dissolved Pt to the ICP-MS system, dissolution of Pt could be detected even at 0.85 V vs. RHE. The authors suggested that at this potential anodic dissolution is the main process whereas at more positive potentials platinum dissolves through oxide dissolution. A similar behavior was found for both types of electrodes concerning time and potential, even though the dissolution rate for the nanoparticles was slightly lower than for the polycrystalline Pt. For the dissolution of a platinum monolayer at 0.85 V vs. RHE 16000 h and at 0.95V vs. RHE 5000 h would be needed. The authors proposed that platinum dissolution at low potentials occurs via metastable, soluble hydroxide/oxide species formed for both types of electrodes, but also emphasized that more work is needed to reach a complete understanding of the processes during Pt dissolution.

In order to study the dissolution of Pt in the presence of chlorides, Geiger et al. used the Scanning Flow Cell coupled online to inductively couple plasma (ICP) coupled with mass spectrometry (MS) and explored polycrystalline Pt in electrolytes in the presence of chloride ions between 1 and 1000 µM as a model system [53]. They suggested that the mechanism of the dissolution is

similar in all used electrolytes, being dependent on the transition during surface oxidation and reduction, where a metastable Pt complex is formed. Chloride ions have an impact on the life-time of this complex and thus on the dissolution of Pt. For anodic dissolution, chloride ions are responsible for blocking the formation of the passive layer whereas the formed Pt complex leads to higher overpotentials for re-deposition during cathodic dissolution.

Aside from the Pt stability, also particle size effects are important for complete understanding of catalyst behavior under practically relevant conditions. Already in earlier work it was shown that the specific activity of Pt increases with the particle size, while the mass activity reaches a maximum around 3 nm [12, 42, 159], and explained by a change in coordination, the potential of zero total charge and a stronger adsorption of oxygenated species, blocking the surface sites. Shao et al. confirmed these findings, and explained the lower activity of nanoparticles with the presence of edge sites [40]. They grew smaller Pt nanoparticles in a layer-by-layer mode using a Cu underpotential deposition (UPD)-Pt replacement technique. Using DFT on cuboctahedral particles, they determined the change of the different surface sites with particle size and the oxygen binding energy. While the activity of (111) sites is larger than for single-crystalline Pt, the lower proportion of (111) at small particle sizes as compared to edge sites results in a surface specific activity decrease. Very similar DFT-based results were published by Tritsaris et al. [39]. Nesselberger et al. investigated the activity of well-defined, size-selected Pt clusters supported on glassy carbon for the oxygen reduction reaction [34], namely Pt_{20} (D =0.6 nm), Pt_{46} (D = 0.8 nm) and $Pt_{>46}$ (D = 2.3 nm). For both Pt_{20} and $Pt_{>46}$ the surface activity was much larger than for commercial catalysts. The mass activity of Pt_{20} was lower than expected which was explained by relative large blockage of surface sites by the interface to the carbon or a lower amount of active sites present. The surface activity of the Pt clusters deposited on the glassy carbon surface

strongly increased with decreasing distance between the particle edges (increasing coverage), and reached almost the one from bulk Pt. The mass activities of the appropriate clusters were more than 6 times higher than those ones of commercial Pt/C catalysts. The authors explained the improvement by the overlapping of the electrochemical double layers, the resulting reduced potential drop in the compact layer, leading to a lower adsorption strength of adsorbed oxygen-derived species. Therefore, this work discussed another contributing factor to the catalytic activity of Pt NP.

Already in earlier work, Nesselberger et al. had studied the influence of the Pt particle size in commercial Pt/C catalysts with different particle size on the ORR activity in three different electrolytes, namely H_2SO_4, $HClO_4$ and KOH using a thin layer RDE technique [35]. Great care was taken to correct for *IR* drop and especially for the background currents of Pt oxidation and the capacitance of the carbon support material. Due to the influence of spectator species, the surface specific activities were largest in $HClO_4$ – even though also perchlorate can be adsorbed to a certain extent on Pt [155]-, followed by KOH and then H_2SO_4. In all electrolytes, the specific activity decreases from polycrystalline Pt over unsupported Pt black particles with an average particle size of 30 nm to high surface area carbon supported Pt NP with the size between 1 and 5 nm. In the range between 1 and 5 nm, opposite to earlier expectations and measurements, where capacitive background currents had not been corrected for, there was no clear change in the specific activity, and there was no particle size where a peak in mass activity was found. The authors tried to simulate the size dependence of the nanoparticles by assuming a cubo-octahedral structure and taking for the individual facets data from single crystal measurements. In addition, they assigned arbitrary activities of step and corner atoms. None of those simulations could reflect the experimentally observed trends, indicating that a simple transfer of single crystal data

to nanoparticles is not possible. In contradiction to these results, experiments on size-selected Pt NPs on glassy carbon by Perez-Alonso et al., including background correction (which is however more facile than for a carbon powder) showed a clear particle size effect [150]. They studied Pt particles with diameters between 2 and 11 nm. From CO temperature programmed desorption (TPD), they determined that with increasing particle size the fraction of terrace atoms increases as well. The specific ORR activity increased with particle size, while the mass activity showed a peak at 3 nm.

Benedikt et al. used a finite cluster approach to model the ORR at a Pt nanoparticle (Pt_{37}) including charged species and electrochemical potential [160]. Only the dissociative mechanism was considered, as the OOH species is not stable on the cluster surface. Minute differences in mechanism between the nanoparticle and an extended surface were found. Also the reactivity of the nanoparticle was lower due to the stronger binding of intermediates at edges. The energy profile significantly differed depending on whether constant charge or constant potential simulation schemes were used. The inclusion of solvent is necessary for the more demanding constant potential calculations, which are considered to result however in a more complete description compared to constant charge models.

Tripkovic et al. carried out calculations of the activities of different particle shapes (tetrahedral, cubic, octahedral, truncated octahedral and equilibrium shaped based on a Wulff approximation) in order to theoretically evaluate the particle size effect [21]. The equilibrium shape also considered the coverage by oxygen species, different to earlier studies. The results reproduced earlier experimental findings: a decrease in surface activity with decreasing particle size and the presence of a maximum at 2-3 nm in the mass activity curve. A moderate interaction with a

support material had little effect on the predicted activity, as the area lost due to interaction with the support was partially compensated by an increase in total surface area of the particle. The tetrahedral particles showed highest activity, but are expected to change their shape towards the equilibrium one with time. The paper also states that well-defined particle shapes only occur for certain numbers of atoms, otherwise there will be more defects and a reduced activity.

Jennings et al. investigated oxygen dissociation on truncated octahedral Pt nanoparticles and Pt-Ti particles theoretically mainly through ab initio calculations. They found that on Pt_{38} the barrier depends on the facet orientation. Several interesting findings were obtained like a correlation between increase in adsorption strength and more facile dissociation, a cluster distortion by oxygen adsorption on Pt(111), and less distortion in combination with a Ti core, connected to electron transfer from Ti to Pt [161].

Li et al. studied the oxygen reduction reaction on Pt single crystals, on cubo-octahedral (polyhedral) Pt NPs with particle size ranging from 2 to 7 nm and on differently shaped (cubo-octahedral, cubic and octahedral) Pt NPs with the size of 7 to 8 nm [36]. Freshly prepared Pt(111) was more active than Pt(100) for the ORR, associated with reduced spectator species coverage. Upon cycling above 0.95 V vs. RHE, the morphology of the single crystals changed. Cycling to 1.3 V then introduced roughening and formation of step-edge sites due to oxide formation, that diminished the activity differences between the different surfaces. Similarly, nanoparticles were affected. While fresh nanoparticles showed a clear particle size effect, with an increase in specific and a decrease of mass activity with particle size, cycling to above 1 V altered the trend in mass activity, and changed the particle size distribution: samples with small particles below 5 nm suffered an increase in particle size and loss in electrochemical surface area (ECSA), while larger

particles were more stable. Also the observation of a particle shape effect was difficult, as the formation of oxide introduced a shape change of the originally cubic or octahedral (with many defects) particles towards more round particles.

Zhang et al. used cubic and octahedral Pd nanoparticles as a template for the preparation of well-defined hollow catalyst particles, i.e. nanocages [162]. They first deposited several atomic layers of Pt chemically onto the Pd particles, and then dissolved the Pd crystals. Based on DFT the authors concluded that dissolution occurs through Pd atoms embedded in the Pt coating that dissolve and leave vacancies that eventually form a channel for complete dissolution of the Pd core. The remaining Pt(-Pd alloy) hulls had well defined (100) or (111) facets. The ECSA of the nanocages was similar to those reported for the nanoframes and also to a commercial Pt/C catalyst, even though the nanocages were much larger. The mass and surface activities of the nanocages was several times larger than for Pt/C, and the octahedral nanocages showed ~2.5 times the surface specific activity of the cubic nanocages. The stability testing resulted in a 36% loss in mass activity over 10,000 cycles, and a slight enlargement in the holes in the cage walls.

Anastasopoulos et al. studied the particle size effect for both Pt and Pd [38]. They used a 10 x 10 array of 1 mm^2 Au electrodes, coated with carbon, onto which the nanoparticles were grown using a physical vapor deposition (PVD) method. For Pt, they observed maximum mass activity at 3.4-4 nm diameter. For Pd, both mass and surface specific activity were much lower, and decreased strongly with decreasing particle size.

Pd nanoparticles could represent an interesting alternative to Pt, as the metal is more abundant compared to Pt, but suffers from a somewhat lower stability. The use of advanced support

materials, alloying and morphological control might offer a solution to these problems, an idea that will be discussed later. In the work of Ju et al., Pd NPs were deposited electrochemically on highly oriented pyrolytic graphite (HOPG) by applying a potentiostatic double-pulse technique [163, 164]. The particle densities for all samples were controlled in the order of 10^9 cm^{-2}. Particles grew in a constant-current mode with a narrow size distribution. The average particle size was adjusted by the growth pulse duration showing a relation of the average height proportional to the 1/3 power of the growth time. A size-dependent hydrogen absorption behavior was observed at Pd NPs when smaller than 8 nm [164]. Smaller Pd NPs tend to have a lower hydrogen content due to the change of lattice structure. In the hydrogen evolution reaction (HER), Pd NPs showed an increased specific current density at selected potentials with decreasing particle size. The activity for HER is primarily affected by the hydrogen content in the Pd lattice [164]. The binding energies of Pd NPs with oxygen atoms and CO molecules increased with the decrease of particle sizes so that, in experiments, a higher overpotential for ORR [164] and a higher oxidation potential for CO stripping [163] were required at smaller Pd NPs. For formic acid oxidation [163], small Pd NPs showed relatively low activity and poor poisoning tolerance. If structural factors are considered with the change of particle size, small Pd NPs tend to possess more well-ordered (111) facets and a high ratio of edge and corner atoms. The stability of Pd NPs was strongly dependent on the pH value of the medium and was reduced at lower pH values (cf. Figure 5) [164].

Luo and coauthors reported the synthesis of Pd nanomaterials supported on carbon obtained via the chemical carbonyl route [165]. The Pd loading was varied between 10 and ~40 wt% Pd and was adjusted by changing the weight of the C support. The lowest and highest loading of the Pd resulted into highly agglomerated structures whereas with a loading of Pd of about ~20%

nanowires and with 30% loading nanorod-like structures were produced. The ORR activity of the formed nanostructures was examined in acidic (0.1M $HClO_4$), and alkaline (0.1M KOH) media. The agglomerated structures showed almost no improvement for ORR in comparison to commercial Pd/C catalyst. However, nanorod- and nanowire- like structures had an improved activity, probably due to an enhanced surface area.

3.2 Pt alloys

Strain and ligand effects play a decisive role in the electrocatalytic behavior of Pt alloys. Especially alloys between Pt and the transition elements Cu, Co, and Ni have been studied intensely [69, 70, 72, 74, 75, 79, 81, 82, 102, 140, 166-173]. These alloys can be prepared using relatively simple methods [78, 138, 174, 175], and show after initial dealloying improved activity towards the ORR. However, they often suffer from limited stability. In part this problem has been mitigated by adding a third alloy component [68, 176, 177]. Considering the extensive treatment of these alloys in recent review articles, only a few points will be discussed in this section: First some papers will be cited, where the effect of alloying additions was treated by well-defined single-crystalline systems and theoretical methods. Afterwards selected results concerning actual alloys of Pt with Cu, Co and Ni will be reviewed.

Brimaud et al. studied the ORR activity of structurally well-defined $Au_xPt_{1\_x}$/Pt(111) monolayer surface alloys with varying Au surface contents using a rigorous approach where STM and a flow cell attached to an ultrahigh vacuum (UHV) system were used [178]. When small amounts of Au

(<24%) are used, a behavior similar to Pt(111) was observed (full reduction to H_2O), but no lowering of the overpotential compared to Pt(111) was found, while higher Au surface contents (>24%) led to higher overpotentials. For Au rich surfaces (>50%), the catalytic properties of the surface alloys shift towards that of polycrystalline Au, with an increasing tendency for H_2O_2 formation.

Stephens et al. studied the influence of subsurface alloying on the activity of Pt(111) for the oxygen reduction reaction, employing both DFT calculations and model alloy experimental studies [65]. They prepared a near-surface alloy by electrodeposition of up to 1 monolayer (ML) of Cu onto Pt(111), followed by annealing in reducing atmosphere. This led to the formation of a subsurface Cu layer on Pt(111) covered by one Pt layer. This alloy was stable during electrochemical cycling. The OH adsorption peak was shifted with increasing Cu concentration in the subsurface layer, and from this shift a decrease of binding energy $\Delta U_{1/6\,ML\ \mathrm{OH}}$ for OH was calculated and used as a descriptor for ORR activity. Up to 0.5 ML Cu, there was good agreement between experimental and theoretical data, indicating that the Pt top layer might in fact be unstrained. The presence of Cu in the subsurface resulted in a volcano relationship between activity and Cu content, or alternatively $\Delta U_{1/6\,ML\ OH}$, and an 8-fold increase in ORR activity compared to Pt(111). Even though the activity enhancement was much lower than predicted from theory, this study nevertheless demonstrated the huge potential of the ligand effect for ORR catalysis, provided such second layer alloying can be transferred into commercial catalysts, and remain stable under the actual operation conditions. Subsequently, Bandarenka et al. applied electrochemical impedance spectroscopy to such near surface alloys [179]. While the CV of the NSA in the OH adsorption region was featureless, impedance data showed similar ORR and OH adsorption processes. However, opposite to Pt(111) [157], only one 2 D phase

transition in the adsorbate layer was observed. The modification of the electronic structure resulted in a positive potential shift as evidenced by the prefactor of the constant phase element.

Yamada et al. deposited 0.3 nm Co on Pt single crystals via molecular beam epitaxy at elevated temperatures, forming Pt-Co surface alloys [180]. Due to surface segregation an enrichment of Pt in the outer layer was observed. inducing surface segregation of Pt atoms. Especially for the (111) orientation, the alloy formation with Co resulted in a strong increase in ORR activity. During cycling, Co dissolution took place, leading to rapid loss of the improved activity.

Cheng et al. used DFT calculations to show that incorporation of a full subsurface layer of 3d transition metal atoms directly beneath a skin of Pt weakens the adsorption strength of atomic oxygen, compared to Pt-skin formed on Pt_3M alloys of the same alloying materials [181]. Both for slab and $Pt_{12}M$ cluster models, Mn and Fe were found to be promising materials for subsurface alloying.

Using DFT calculations, Escaño et al. have shown for Pt_3Co that under oxygen environment, thicker Pt-skins of 2 or 3 atomic layers are needed to suppress Co migration and to have similar stability to Pt dissolution as pure Pt(111) [80]. It was also proposed that a migration barrier layer, e.g. Os or Pd, between a monolayer of Pt and Pt_3Co would not only inhibit Co migration but also increase the stability of Pt compared to pure Pt(111).

Chi et al. carried out in-situ scanning transmission electron microscopy (STEM) measurements to study the structural and compositional development of Pt_3Co NPs during thermal annealing at the atomic scale, as such annealing steps are required to establish the correct surface properties and

lead to an increase in the catalytic activity of such nanoparticles [182]. The authors recognized five important stages in the surface rearrangements with increasing temperature: starting from an initial random elemental distribution at room temperature, surface segregation of platinum to the surface accompanied by (110)-facet formation was observed at 350 °C. At 500 °C, the Pt surface enrichment was lost. At 600 °C, a disorder-order transition took place, initiated at (110) facets and propagating then throughout the nanocrystal. At 700 °C, a completely ordered stable structure was obtained, while at 800 °C amorphization started.

In order to investigate the active sites for the ORR, Rurigaki et al. studied the high index planes of Pt_3Ni, investigating the orientation dependence of the ORR on the n(111)–(111) and n(111)–(100) series of Pt_3Ni (n = 2, 3, 5, 9 and $_\infty$) [183]; i.e. they studied (997), (553), (331), (544) and other orientations. They found a decrease in specific activity for ORR, when the step atom density on the n(111)–(111) series of Pt_3Ni was increased. However, the highest activity for the ORR in the high index planes of Pt_3Ni examined, was found for $Pt_3Ni(211)$ = 3(111)–(100) and $Pt_3Ni(322)$ = 5(111)–(100).

Different $Pt_x Ni_{1-x}$ nanoarchitectures have been synthesized recently by varying Pt/Ni precursors ratio 1:2-3:1, namely; cubic alloy nanocrystals ($PtNi_2$), cubic alloy crystals@Pt particles ($PtNi_2$@Pt), concave-tetrahedral alloy nanocrystals (Pt_2Ni) and Pt_2Ni alloy@Pt [184]. These have been characterized by transmission electron microscopy (TEM), high angle annular dark field tomography (HAADF) combined with STEM, X-Ray diffraction (XRD), and energy dispersive spectroscopy (EDS) and their ORR electrocatalytic activity have been examined. The Pt_2Ni alloy@Pt consisting of concave-tetrahedral core and extended Pt shells exhibited the highest ORR catalytic activity and durability. The extended Pt shells with Pt(111) facets showed higher

surface area, rich adsorption sites. From the unclear Pt oxidation and reduction peaks over Pt_2Ni alloy@Pt catalyst, it was concluded that the alloy crystal core suppresses the loss of Pt active sites which leads to a decreased catalytic activity.

Nucleating FePt shells on an oxidation protected Ni cores led to Ni/FePt nanoparticles which were surface activated and transferred to an active Ni/Pt ORR catalyst by washing with acetic acid [185]. Different Ni core nanoparticle sizes, ranging from 4.2 to 9 nm led to different activities when compared to the state-of-the-art benchmark Pt catalyst. RDE measurements in O_2-saturated 0.1M $HClO_4$ at 1600 rpm were done for the synthesized Ni/Pt catalysts with three different Ni nanoparticle core sizes (5.8, 8.9 and 10.6 nm) and compared to a commercial Pt catalyst. A half-wave potential shift of ca. 0.913 V vs. RHE was recorded for the 5.8 nm Ni core size catalyst compared to ca. 0.85 V vs. RHE for the commercial one. A significant increase in the specific activities was also obtained due to core-shell structure. This have been concluded from the similar activities of all synthesized Ni/FePt catalysts (1.95-2.18 mA cm^{-2}) comparing to only 0.34 mA cm^{-2} for the commercial one. The synthesized Ni/FePt catalysts showed also a good durability over ca. 10,000 potential cycles between 0.66 and 1.06 V vs. RHE in O_2-saturated electrolyte.

Xu et al. were able to synthesize multicomponent Pt-Ni alloy nanocrystals shape-selectively bounded by high-index facets, namely concave-nanocubic, nanocubic and hexoctahedral by adjusting the amount of glycine in a wet chemical reduction procedure [174]. The synthesized catalysts were characterized by scanning electron microscopy (SEM), high resolution scanning electron microscopy (HRSEM), TEM, high resolution TEM (HRTEM), HAADF-STEM, EDS, XRD, and underpotential deposition X-Ray photoelectron spectroscopy (XPS). The concave-

nanocubic and the hexoctahedral NP gave a better ORR activity when compared to Pt-Ni nanocubes and commercial Pt/C catalysts. As demonstrated by Fourier transform infrared spectroscopy (FTIR) and ultraviolet/visible spectroscopy (UV-VIS) spectra, it was concluded that glycine can control the nucleation and growth rates of the formed nanocrystals by slowing the reduction rates of Pt(IV) and Ni(II) species through the coordination to the central metal ions.

Sakamoto et al. synthesized octahedral PtNi nanoparticles chemically and tested its performance with a rotating disc electrode technique and via fuel cell testing within a MEA [175]. After spectroscopic characterization of the synthesized catalyst it was concluded that a core-shell nanostructure is developed with a Pt(111) facets-rich shell and Ni cores. From the RDE measurements, it was deduced that the prepared catalysts have a 6 times higher mass activity and 18 times higher specific activity than an (unspecified) commercial Pt/C catalyst. In the PEM fuel cell testing, the synthesized catalysts showed almost the same behavior like the commercial ones but with about 71 % lower Pt loading of the catalyst.

Pt-Ni nanooctahedra with larger Ni content ($Pt_{1.5}Ni$, PtNi, $PtNi_{1.5}$) suffer from site-specific compositional segregations. They do not form a pure Pt shell, but often show enrichment of Pt at edges and corners while Ni prevails on the (111) facets [186, 187]. This was studied in further detail by Gan et al. [188]. They synthesized octahedral $Pt_{1.5}Ni$ NPs via solvothermal reduction at 120 ° in dimethylformamide (DMF), followed by transfer to a support material. Using in situ (HR)TEM and STEM combined with electron energy loss spectroscopy (EELS), the morphological stability and surface composition evolution of the phase-segregated octahedral Pt−Ni NPs under thermal annealing at different temperatures were investigated. Isolated NPs maintained the octahedral shape up to 500°C, and started to become round above 600°C.

HRTEM showed the presence of slightly concave Ni-rich (111) surfaces. Annealing at 400-500°C caused atoms from the Pt-rich corners to diffuse into the facets causing a flattening of the facets. HRTEM confirmed the formation of Pt-rich (111) surfaces with Ni-rich subsurface layers during annealing. Particles with this surface composition are expected to be catalytically more active and more stable. However, agglomerated particles lost their shape already at 400°C, and therefore improved dispersion is necessary to verify the improved catalytic properties for ORR experimentally.

Chen et al. synthesized electrocatalysts with highly improved activity and durability by transformation of $PtNi_3$ dodecahedra synthesized by a solvothermal method into Pt_3Ni hollow nanoframes with a Pt skin surface with a thickness of at least 2 Pt monolayers [85]. The transformation was accomplished by corrosion in nonpolar solvents with added oleylamine due to exposure to air. Depending on the exact conditions, especially temperature, the duration of the process could be controlled. The nanoframe structure was formed as the edges of the original nanocrystals were enriched in Pt compared to the interior of the crystal facets, favoring faster dissolution at the latter sites, resulting eventually in the formation of Pt_3Ni at the edges and loss of Ni and Pt from the interior of the crystals. The electrocatalytic properties of the nanoframes were determined and compared to those of a PtNi/C and a commercial Pt/C electrocatalysts (TKK, 5 nm Pt). The specific activity of the Pt_3Ni structures at 0.95 V in 0.1M $HClO_4$ was found to be more than 16 times higher than the one of commercial Pt/C catalyst, and, due to the open architecture of the Pt_3Ni nanoframes the mass activity was reported to be even 22 times higher than the one of the commercial catalyst. The increased activity was explained by a combination of the strain effect and an electronic effect reducing the OH spectator species coverage on the surface. The latter effect was also used to explain the good stability of the catalysts during

longterm cycling. A further improvement of the electrocatalytic behavior was achieved by impregnation with ionic liquid, which results in an increased oxygen solubility.

In subsequent work, the same group of authors studied the atomic structure of the nanoframes by in situ X-ray absorption spectroscopy (X-ray absorption near edge structure (XANES); extended X-ray absorption fine structure (EXAFS)) in order to gain more information of the Pt-skin formation on Pt_3Ni nanoframes, as they observed that the Pt skin structure was not always formed [83]. It was recognized from the study that the critical step is significant segregation of Pt to the edges of the dodecahedra during the initial particle synthesis procedure, being the prerequisite for successful formation of the Pt-skin structure.

Huang et al. used metal dopants to increase activity and stability of PtNi nanoparticles [176]. Synthesized octahedral $Pt_3Ni(111)$ nanocatalysts of 4 nm diameter were doped by addition of different transition metal precursors into suspension. For nanoparticles doped with 1.6 at% molybdenum a specific activity 81 times and mass activity 73 times higher than commercial Pt nanoparticles at 0.9 V in 0.1M $HClO_4$ was reported (using a Surface specific activity (SA) of 0.127 mA cm^{-2} and mass activity (MA) of 0.096 A mg^{-1} for commercial catalysts, which is a benchmark clearly below the values reported by Nesselberger et al. [35]). In addition, Mo-doping led to significant improvements in stability and after stability tests only 6 % of the initial activity was lost. Calculations by DFT showed that the Mo-dopants diffused to subsurface positions at edges and corners, leading to increased stability by replacing Ni-atoms at those positions susceptible to Ni-leaching. Also, DFT-calculations were used to show that subsurface Mo decreased the binding energy of single oxygen atoms to Pt-sites close to the Mo-dopants, possibly explaining the increased activity.

Beermann et al. synthesized near surface Rh-doped Pt-Ni octahedral nanoparticles supported on carbon via a solvothermal method and compared ORR activity and stability to carbon supported Pt-Ni octahedral nanoparticles [68]. During electrochemical stability tests after 4,000 cycles the activity of the newly synthesized Pt−Rh−Ni/C catalyst is improved and almost no change in the octahedral shape of the particles was detected even after 30,000 cycles. In contrary, almost 70 % of the initial activity of Pt−Ni/C octahedral particles was lost after 4,000 cycles and after 8,000 cycles the octahedral shape of the particles was completely lost. After detailed microstructural investigations of the atomic rearrangement processes, the diffusion of the Pt atoms during cycling were found to be the reason for the shape loss of Pt−Ni/C catalyst. In the Pt−Rh−Ni/C catalyst Pt atom diffusion was hindered by the presence of Rh, preventing loss in the shape and activity.

These studies show that the controlled exploitation of ligand and strain effects, together with the control of the shape and size of nanoparticles can dramatically increase the NP activity. Innovative shapes like the nanoframes, but also hollow nanoparticles can enlarge the Pt mass activity greatly. The stability problems of many binary late transition metal – Pt alloys can be overcome by adding a third component selective enriching at certain sites of the nanoparticle and acting as a diffusion barrier.

Opposite to alloys like Pt_3Ni, alloys between Pt and rare earth metals already show large stability without addition of a third element. The preparation and electrocatalytic behavior of these alloys is discussed in detail in the next two sections.

4 Preparation of Pt-rare earth Alloys

The major complication of making alloy nanoparticles based on rare earth metals lies in the extreme sensitivity of the rare earth elements towards air and moisture, and the very low equilibrium potentials for the corresponding M/M^{3+} redox couple (as expressed by large negative free energies of formation of the oxides and halides of the rare earth elements). Thermodynamically, compounds like Pt_3Y and Pt_5Gd have been reported to have much more negative formation enthalpies compared to other binary Pt alloys like Pt_3Ni or Pt_3Fe [92]. For Pt_3Y, a Gibbs free energy of formation can be calculated according to $\Delta G_f(Pt_3Y) = -387 + 0.02 \times T$ in kJ mol^{-1} [189, 190]. This equation was experimentally established for temperatures between 1300 K and 1700 K, but can serve as a guide for lower temperatures as well. However, Y(III) oxide is even more stable, with $\Delta H_f(Y_2O_3) = -1{,}905.6 \pm 2.3$ kJ mol^{-1} at room temperature and $\Delta S_f(Y_2O_3) = -298.136$ J K^{-1} mol^{-1} [191, 192]. Considering a simple chemical gas phase reduction with hydrogen, as very common in the preparation of Pt NP from Pt precursors, and taking thermodynamic data for gaseous water (e.g. from [192]), one computes for the reaction (Eq. 1) a Gibbs free energy of reaction of +368.7 kJ mol^{-1}. This value decreases slightly at higher temperatures, but still remains above 300 kJ mol^{-1} even at 900 K. For the actual simultaneous reduction (Eq. 2), which represents a more realistic situation, one calculates thermodynamic data for $PtCl_4$ [193] and gaseous HCl [192] a Gibbs free energy of reaction of -1 MJ mol^{-1}, becoming more negative at elevated temperatures. Therefore, the formation of an alloy phase is thermodynamically feasible. However, the Gibbs free energy for the reaction of the Pt species alone (Eq. 3) is even slightly more negative, with -1.38 MJ mol^{-1}. The enthalpies of the two reactions become closer with increasing temperatures.

$$Y_2O_3 + 3H_2 + 6\,Pt \rightleftarrows 2Pt_3Y + 3H_2O \quad (1)$$

$$Y_2O_3 + 15H_2 + 6\,PtCl_4 \rightleftarrows 2Pt_3Y + 3H_2O + 24HCl \quad (2)$$

$$12H_2 + 6\,PtCl_4 \rightleftarrows 6\,Pt + 24HCl \quad (3)$$

With an yttrium halide precursor (Eq. (4)), which is easier to handle compared to the oxide due to its better solubility, the thermodynamic situation becomes even worse: $\Delta_R G$ = -858.3 KJ mol^{-1}. For all calculations, thermodynamic data refer to two moles of Pt_3Y formed.

$$2YCl_3 + 15H_2 + 6\,PtCl_4 \rightleftarrows 2Pt_3Y + 30HCl \quad (4)$$

Therefore, one can expect for gas phase reduction a large risk of keeping unreacted Y precursor in the product mixture. This can be mitigated by accurate control of the reaction conditions, rapid removal of any hydrogen chloride and water formed, and elevated reaction temperatures. Also the selection of a less stable Y precursor might be beneficial, and the use of reduction agents stronger than hydrogen. Similar considerations apply for other methods like solvothermal reduction.

In general, a number of different routes can be imagined or even have been tried in order to make Pt-rare earth metal (RE) alloys in nanoparticulate form. Not all of those have been successful so far. The methods can be roughly grouped into physical methods, chemical methods and electrochemical methods, and will be discussed below.

4.1 Physical Methods

For fundamental studies requiring only small amounts of catalyst, physical methods are most suitable. Especially evaporation and sputter-based techniques have been successfully applied. Along these lines, Chorkendorff and co-workers studied size-selected Pt-rare earth alloy nanoparticles, between 3 and 9 nm in size, supported on glassy carbon and generated using a magnetron sputter gas aggregation-based cluster source. Both Pt-Y alloys and, within the CathCat project, Pt-Gd alloys were studied [89, 93, 194]. The studies showed that specific activities of the alloy nanoparticles increase with the particle size and match the value of the corresponding bulk, polycrystalline surface (Pt_3Y and Pt_5Gd for Pt_xY and Pt_xGd, respectively) when the particle size is greater than 9 nm (cf. Figure 6). The particle-size dependence of the ORR activity was explained in terms of compressive strain effects assuming a core/shell structure for the nanoparticles, which was asserted by combination of XPS, EDS and EXAFS measurements, resulting in a thickness of the Pt shell of ~1 nm. The mass activities for the Pt_xM nanoparticles after initial dealloying treatment are much larger than for Pt nanoparticles, and they reach the maximum mass activity also at larger particle size, making them more stable towards degradation (cf. Figure 6). In particular, at 0.9 V vs. RHE for Pt_xY an activity of 3.0 A mg^{-1}_{Pt} at 9 nm particle size and for Pt_xGd of 3.6 A mg^{-1}_{Pt} at 8 nm particle size were reported, while pure Pt NP prepared with the same method showed an activity of 1 A mg^{-1}_{Pt} at 3 nm particle size. In the case of the Pt_xGd catalyst, the outstanding mass activity achieved is only surpassed in the literature by Pt_3Ni nanoframes [85] and Mo-doped Pt_3Ni nanoparticles [176]. For commercial Pt/C support a maximum activity of 0.55 A mg^{-1}_{Pt} had been reported [35]. Assuming a cathode loading of 0.4 mg cm^{-2} for the MEA, and presuming that there will be an activity decrease similar to Pt NP when making the transition from model system to carbon supported catalyst in the MEA, one

should reach a current density of 0.8 A cm^{-2} at a cathode potential of 0.9 V vs. RHE. However, Chorkendorff and co-workers also demonstrated that not only the initial performance of these alloys is excellent, but that they also possess good stability. In fact, even after potential cycling in oxygen-saturated solution for 10,000 cycles, Velázquez-Palenzuela et al. reported an activity still corresponding to 70% of the initial one (cf. Figure 7) [93]. This combination of excellent stability and activity however is critically depending on the actual size of the nanoparticles; therefore, the adjustment of the correct particle size is of utmost important for the inclusion of these materials in nanoparticulate form into an MEA. Very recently, Pt_xY alloy nanoparticles were also tested in an MEA; those particles were directly deposited by placing a specially designed MEA with the cathode side into the magnetron nanoparticle source at DTU [195]. This method represent not an option for commercial MEA fabrication, though.

With respect to actual fuel cell applications, nanoparticles on carbon support are difficult to prepare using sputtering. However, thin film approaches using special substrates like those used for the 3M whisker-based NSTF catalyst layers are an option [105, 196]. Typically Pt-Ni alloys are deposited onto such substrates by sputtering [196]. Sputtering has also been used to generate thin films of Pt-rare earth alloys and alloy nanoparticles on different substrates. Films of Pt-La alloys of various composition were prepared by co-sputtering using two targets [197]. Yoo et al. have prepared Pt_3Y alloy nanoparticles with an average particle size of 10-12 nm by RF magnetron co-sputtering using targets of pure Pt and Y metal [198]. They employed a pressure of 200 mTorr and an Ar/He mixture as gas phase. Using that method, they were able to make both samples for RDE testing and for MEA testing. In the latter case, they coated gas diffusion layers (GDLs) with a C/Nafion ink, sputtered, and repeated the coating/sputtering sequence a couple of times. In subsequent work also Pt_3La was explored, together with several Pt-transition metal

alloys [199]. It was reported that the particle size depended on the sputtering pressure, and that a larger amount of helium in the gas mixture enhances particle formation. The formation of a ~1-1.5 nm Pt skin on the particle after leaching was proven by angle resolved XPS [199].

Also electron beam evaporation can be used for the preparation of rare earth alloys. Favaro et al. used the sequential deposition of Pd and Y by electron beam evaporation followed by annealing steps in order to form Pd_3Y nanoparticles on HOPG and Nitrogen-doped HOPG (N-HOPG) [200]. Synchrotron-based XPS was used to prove the alloy formation (cf. Figure 8).

Another possibility might lie in a technique applied in literature for noble metal particles: the collection of nanoparticles generated by sputtering or other physical vapor deposition techniques in an ionic liquid (IL) [201-204]. Ionic liquids have the advantage that their vapor pressure is very low, so that they can be used even in the vacuum.

Hatakeyama et al. used the sputter deposition technique for the synthesis of Au nanoparticles and studied the influence of different experimental conditions on their size and size distribution [203]. As a capture medium for the nanoparticles the IL 1-butyl-3-methylimidazoliumtetrafluoroborate ($[C_4mim]BF_4$) was used and the obtained particles were characterized by small-angle X-ray scattering (SAXS) immediately after the synthesis. The authors found out that temperature of the Au target and applied voltage significantly affect size and size distribution of the nanoparticles whereas sputtering time, distance between the metal target and the capture medium, discharge current and Ar pressure have no or a negligible influence. For synthesizing size-controlled smaller nanoparticles a lower temperature of the target and a higher applied voltage are recommendable.

Suzuki et al. synthesized AuPt alloy nanoparticles by sputter deposition into (N,N,N-trimethyl N-propylammonium (TMPA) bis(trifluoromethanesulfonyl) imide (TFSI) [202]. They were able to control the particle size and alloy composition by adjusting the ratio of Au and Pt in the starting metal targets. For all obtained samples, the average diameter of the nanoparticles was below 2 nm with a narrow size distribution (cf. Figure 9). The methanol oxidation activity of the synthesized alloys was examined by cyclic voltammetry and the results were compared with those ones obtained from the pure Au and Pt NPs. In both directions of the CV in the case of AuPt NPs distinctive anodic peaks were observed. The results indicated that the size effect of Pt NPs on the methanol oxidation was cancelled by introducing Au atoms into the NPs.

In the work reported by Richter et al. several ionic liquids were synthesized with the aim to use them for the synthesis of different metal nanoparticles (Cu, Ag, Au) not only as the solvents but also as reducing agents [201]. For the metal nanoparticle synthesis, a chemical approach using microwave synthesis as well as physical vapor deposition methods was applied. For microwave synthesis, aprotic ammonium ILs resulted in smaller particle sizes in comparison to protic ones. Furthermore, the reducing group has an influence on the particle size. Hydroxyl compounds as rather mild reducing agents result in smaller particles as opposed to the formate ions, which are reducing more rapidly the metal ions, resulting in faster particle growth. The authors developed also a new evaporation technique in which ionic liquid covers the wall of a rotating glass flask. The metal atoms generated condensate on the surface of the IL, forming particles. For this approach to work it is critical that the diffusion of the nanoparticles into the IL happened faster than the arrival of new material from the gas phase, otherwise film formation would occur.

Platinum nanoparticles with a mean particle size between 2 and 4 nm were synthesized by sputter deposition in a trimethyl-n-propylammonium (Me_3PrN) TFSI ionic liquid as a capture medium by Tsuda and coauthors [204]. The active surface area of the nanoparticles (deposited on a glassy carbon (GC) electrode) Pt/GC was examined by CO stripping voltammetry. The activity for ORR was very dependent on the Pt/GC preparation conditions. In addition, a modified Pt/GC was prepared by rinsing Pt/GC electrodes with acetonitrile solution. These electrodes showed even better catalytic activity and no CO poisoning behavior in comparison with originally prepared Pt/GC electrodes.

Electron-beam evaporation was used by Ertas et al. in order to fabricate nanoparticles in which Gd metal is sandwiched between two SiO_2 layers for oxidation protections, using polystyrene nanobeads supported on silicon as a template [205]. After deposition of the second SiO_2 layer the polystyrene was dissolved in toluene. Diameters as low as 80 nm were achieved. Residual oxides were removed with annealing of the as-fabricated nanoparticles in hydrogen atmosphere.

4.2 Chemical Methods

The approach to prepare PtRE nanoalloys via chemical co-reduction of Pt and rare earth precursors is a great challenge, since the reduction potential for rare earth metals is as low as -2.0 V vs. RHE [122]. It was reported that the co-reduction via conventional reducing agents, e.g., $NaBH_4$ and CO, followed by heat-treatment under inert gas at 300-900 °C, finally led to Pt nanoparticles modified by rare earth oxides [122, 123, 206-208]. However, Wagner's group

claimed that rare earth metallic NPs were obtained via alkalide reduction in an inert gas filled glove box [209, 210]. The akalide used in their work was composed by the alkali metals anions and crown-ether complexed cations: $K^+(15\text{-crown-}5)_2Na^-$. This latter is one of the strongest reducing agents on Earth, able to reduce MCl_3 (M = rare earth elements) to metal. Although these particles remained stable in the glove box, they were easily oxidized under air. Recently, Wagner and co-workers reported that Gd core Au shell (Gd@Au) NPs can be obtained via alkalide reduction, confirmed by TEM, (see Figure 10) [211]. The XRD pattern under air showed diffraction peaks belonging to Au face centered cubic and Gd hexagonal structures. Such a result indicates that both Gd and Au metallic states remained stable in air. Therefore, it is possible to synthesize metallic rare earth NPs via a soft chemical route. However, the deposition of an actual alloy using that technique still needs to be demonstrated.

A recently published paper by Durante and coworkers reports the synthesis of Pt_xY nanoparticles supported on a commercial mesoporous carbon (MC) [212]. The NPs were prepared following a solid state synthesis in a quartz tubular furnace under H_2 flow. The authors tested several Pt precursors ($PtCl_2$, K_2PtCl_6, $Pt(acac)_2$ and $Pt(Phen)Cl_2$), different temperatures (250-900 °C) and reaction times (1.5-7 h) and evaluated their effect on the NPs shape and alloy formation. The reduction of $PtCl_2$ and K_2PtCl_6 in the presence of $Y(NO_3)_3{\cdot}6H_2O$ always led to Pt/Y_2O_3 NPs, whatever the reduction temperature was. Pt_xY NPs (4 nm diameter), where *ca* 41% of the Y atoms are alloyed with the Pt, were synthesized by the reduction of $Pt(acac)_2$ and $Y(NO_3)_3{\cdot}6H_2O$ by H_2/N_2 flow at 600°C for 5 h. The formation of Pt_xY was demonstrated by the analysis of the Y 3d photoemission peak, which evidences also the formation of yttrium carbide and yttrium oxide (cf. Figure 11).

Liu et al. recently claimed the synthesis of Pd-Y-Pt core-shell-shell NPs [213]. The mechanism to control the surface reaction on Pd core was explained as reaction between Pt-H_{ads} and the Y complex, which was said to result in metallic Y coverage. Then the Pt precursor was added into the system, and reduced under hydrogen gas. Finally, it was reported that Pd-Y-Pt NPs with core-shell-shell morphology were obtained, supported by TEM and HAADF tomography. XPS revealed the absence of Y^{3+}, assuming that Y presented zero-valence or lower oxidation state than Y^{3+}.

4.3 Electrochemical deposition

Due to the very low standard potentials of the rare earth elements, they typically cannot be deposited from aqueous electrolytes, even though successful deposition of Sm-Co alloy nanoparticles from aqueous electrolytes has been reported [214]. Therefore molten salts, non-aqueous electrolytes and ionic liquids seem most suitable for their deposition and the deposition of the corresponding alloys. Originally, studies on rare earth electrochemistry were in part motivated by possible applications in recycling of nuclear fuels [215-219] and by recycling of used magnets and other components ("urban mining") [220-222].

In a review by Simka et al., aside from the electrodeposition of conventional metals from non-aqueous solutions also the electrodeposition of Gd and La alloys from non-aqueous solutions was discussed [223]. Martinot et al. studied the electrodeposition of lanthanum from several organic solvents (e.g. DMF, γ-butyrolactone and mixtures thereof with THF or acetonitrile) [219]. They observed a two-stage reduction process with a quasi-reversible step from La^{3+} to La^{2+} (~-0.7 V vs. Pt quasi reference), and metal deposition at a much lower potential (< -2 V). In presence of

Li-based supporting electrolytes, Li metal was co-deposited during long-term electrolysis, in the absence of Li however a passive layer formed by reaction with the organic electrolyte. Pulse electrolysis was found to be the preferable technique for deposition. Liu et al. reported on the electrodeposition of rare-earth alloys with iron group elements and cited some early works mainly from Japan [224]. In their own experiments, they prepared Gd p-toluenesulfonate and reported the electrodeposition of Gd and a Gd-Co-phase from DMF that alloyed during heat treatment [224, 225]. The deposit quality was improved by using urea as an additive [224, 225]. Surprisingly, the potentials associated with the Gd^{3+}/Gd(0) redox reaction were only ~-1 V vs. saturated calomel electrode (SCE). Before heat treatment, the deposited phase was amorphous [224, 225].

The deposition of rare earth elements from ionic liquids has been discussed in the literature, and was corroborated by a recent patent [216, 217, 226, 227]. In 2002, Bhatt et al. reported Eu electrodeposition from a melt of tetramethylphosphonium TFSI at 160 °C [217]. Later, Bhatt et al. carried out experiments on rare earth electrochemistry in trimethyl-n-butyl-ammonium TFSI [216]. The study focused on La, Sm and Eu cations introduced as hydrated TFSI complexes. The TFSI salts were prepared by the reaction of the metal oxides with the TFSI acid in aqueous solution. The structure of these complexes was determined by IR and Raman spectroscopy and, for La ions, single crystal XRD. The results demonstrated that the TFSI coordinates with the La ions through one of its sulfonyl oxygen atoms forming “three six-membered chelate rings”. Two different crystallographic configurations were found, and the bond lengths and angles were determined. The Lewis acidity and therefore coordination strength of the TFSI ion is reported as low. Conclusions on the other two cations studied were drawn based on the comparison of the vibrational spectra. The authors also conducted initial studies on the electrochemistry of the three

ions in the ionic liquid, referring all potentials to the ferrocenium/ferrocene Fc^{+}/Fc redox couple. They assigned the single cathodic current rise at low potentials in the La system to La metal deposition, and the additional peak features seen in the voltammogram of $[Sm(TFSI)_3(H_2O)_3]$ and $[Eu(TFSI)_3(H_2O)_3]$ to the RE^{3+}/RE^{2+} redox couple. The peak potential for the La deposition was reported as -2.4 V vs. Fc^{+}/Fc, for Sm deposition -2.85 V and Eu deposition -3.0 V. Confirmation of metal dissolution by non-electrochemical methods was not provided. Analysis of the Sm^{3+}/Sm^{2+} peak couple showed charge transfer control, and permitted to derive diffusion coefficients consistent with literature, thus supporting the peak assignment. For Eu, the deposition of a grey layer rapidly oxidized in air was seen after a longterm experiment, indicating that indeed lanthanide metal had been obtained. A reaction of the metal layer with residual moisture was considered as a possible, but not probable source of the irreversibility of the deposition. Rather a very low charge transfer kinetics was considered as responsible for the absence of a dissolution reaction.

Yamagata et al. studied the electrochemical behavior of Samarium, Europium, and Ytterbium in 1-Ethyl-3-methylimidazolium (EMI) TFSI and 1-n-butyl-1-methylpyrrolidinium (BMP) TFSI [228]. Their study aimed not at metal electrodeposition. The authors used an ionic liquid based Ag/Ag+ reference electrode and calibrated it with respect to the Fc^{+}/Fc couple. The potential for Eu^{3+}/Eu^{2+} was 0.128 V vs. Fc^{+}/Fc. The Eu^{2+} ion was reported as stable in the electrolyte, as concluded from a Nernstian response after reduction of a known amount of Eu^{3+}. Low diffusion coefficients in the order of 3×10^{-8} cm^2s^{-1} were determined from potential and current step experiments, and indication for complex formation with TFSI was obtained from the Stokes-Einstein radii. Similar diffusion coefficients were also found in subsequent work [229]. The redox potential for Yb^{3+}/Yb^{2+} was more negative (~-0.57 V) than the one of the Eu system, and

the one for Sm^{3+}/Sm^{2+} much more negative (~-1.03 V) [228]. This is in line with the corresponding standard potentials in aqueous solutions [230].

Legeai et al. discussed the electrodeposition of lanthanum from octyl-1-methyl-pyrrolidinium TFSI in ambient atmosphere, using $La(NO_3)_3$ as the precursor [227]. They heated the hydrated compound for 1 week at 105 °C. Acetone was used to help with the dissolution of the precursor in the ionic liquid. The authors identified a reduction peak at -1.6 V vs. a Ag/AgCl wire pseudo-reference electrode with La deposition. At constant potential, they obtained La-containing deposits, but also saw the presence of fluorine and sulfur in the EDS. They assigned this to the formation of corresponding La compounds and the observed irreversibility of the deposit formation.

Very recently, Zhang et al. electrodeposited La metal at 60 °C from 1-butyl-3-methylimidazolium dicyanamide using a $LaCl_3$ precursor [231]. From running voltammograms in mixed ionic liquids, they could determine that four dicyanamide ions react with each La ion to form a complex. Opposite to the work by Legeai et al., in this work also a clear dissolution peak was obtained. The diffusion coefficient of the La complex was determined as $1.2 \cdot 10^{-10}$ cm^2s^{-1}. The nature of the deposit formed potentiostatically was supported by SEM, XRD and XPS measurements, even though also in this work (possibly due to oxidation after exposure to ambient air) La oxide was found. The influence of the deposition potential on the morphology of the deposits was clarified by SEM measurements (cf. Figure 12).

Ispas et al. successfully deposited samarium from 1-butyl-1-methylpyrrolidinium (BMP) TFSI at a temperature of 120 °C [232]. Again no dissolution peak was obtained, the partially metallic

nature of the obtained deposit however unequivocally proven by XRD. Otherwise, oxides were observed due to the contact with ambient atmosphere during sample transfer. Attempts to prepare Co-Sm alloys were carried out, but the results were not conclusive.

The electrodeposition of dysprosium from its triflate salt was investigated both from non-aqueous solvents and from the ionic liquid 1-Ethyl-3-methylimidazolium trifluoromethanesulfonate, as reported by Lodermeyer et al. [233]. While the deposition from dimethylformamide was successful, the one from the ionic liquid failed, as did the deposition from a propylene carbonate / dimethylcarbonate mixture, and from Tetrahydrofuran/γ-butyrolactone. Acetonitrile only gave deposits on Pt substrates. Again, even in DMF deposition was irreversible. A significant amount of oxidation was observed, though, in analysis with Auger depth profiling. For magnetic characterization, the authors therefore protected the layer by an additional Al coating.

Glukhov et al. discussed the electrodeposition of Y, Gd and Yb from ionic liquids with the triflate anion at 100 °C [234]. From ILs with the cation 1-Butyl-2,3-dimethylimidazolium the electrodeposition failed. In tributylmethylammonium triflate, no sign of reduction was seen for Gd and Y for a Pt working electrode (WE), whereas on Cu, indication of deposition was seen during the initial phase of the anodic sweep (after sweeping the potential first in the cathodic direction), and formation of a black deposit was observed. In BMP triflate cathodic peaks were observed for all three RE ions, and interpreted as metal deposition. This interpretation was supported by the formation of a black deposit during potentiostatic and galvanostatic experiments, but not corroborated by chemical analysis of the deposit layer.

In a series of papers, Hussey and coworkers discussed the electrochemical behavior of several rare earth element ions in ionic liquids [218, 220, 230]. The optical spectra of a Ce^{3+} solution in BMP TFSI, prepared by anodic dissolution of Cerium metal at 0.74 V vs. Fc^{+}/Fc, were very close to spectra in aqueous solutions, indicating weak coordination by the IL [218]. Voltammograms revealed that a reduction to Ce^{2+} occurs, but the formed species is unstable and disproportionates to Ce^{0} and Ce^{3+}. The metallic Ce however immediately reacts with the ionic liquid, in a manner analogous to solid electrolyte interface formation. Extended polarization of a Pt electrode at -1.8 V vs. Fc^{+}/Fc resulted not in metal deposition, but in the formation of a passivating layer. Addition of chloride ions even accelerated the disproportionation reaction. The half wave potentials reported by Pan and Hussey for Sm, Eu and Yb ions in BMP TFSI at 50 °C are very similar to the results obtained by Yamagata et al. [230]. While Eu^{2+} and Yb^{2+} were stable in the IL, this was not the case for Sm^{2+}. Impedance measurements revealed a relatively sluggish charge transfer kinetics for the $Eu^{3+/}Eu^{2+}$ and $Yb^{3+/}Yb^{2+}$ redox reactions. The diffusion coefficients as determined from RDE measurements were four times higher than those reported by Yamagata et al. at 25 °C [228], but this is mainly a temperature effect [230]. The addition of chloride ions could lead to the precipitation of $RECl_3$, and lowered the reduction potentials [230]. Finally Chou and Hussey demonstrated limited stability and disproportionation also for Pr^{2+} and Nd^{2+}, again in BMP TFSI, and attempts at metal electrodeposition failed [220].

Kondo et al. reported the electrodeposition of Nd from triethyl-pentyl-phosphonium bis(trifluoromethyl-sulfonyl)amide ([P2225][TFSI]), but used a rather high temperature of 150 °C to lower the viscosity of the IL [221]. The adhesion of the deposit on the substrate depended strongly on the overpotential, at larger overpotentials it was lower. The deposits formed potentiostatically were characterized by SEM (cf. Figure 13). EDS and XPS, and reported as

mainly metallic with some oxide content. Deposition from trimethyl-N-hexylammonium TFSI failed. A Nd counter electrode was used in the experiments. In the same [P2225][TFSI] electrolyte, the authors also studied the Dy system [235]. The diffusion coefficient was reported as 2 x 10^{-8} cm^2s^{-1} at room temperature in this electrolyte. A Dy film was deposited that was mainly metallic and oxidized only at the surface. Nd and Dy were also deposited in a choline-based IL in connection with recycling of magnets [236]. Later, Matsumiya et al. studied the electrodeposition of Nd from N,N-diethyl-N-methyl-N-(2-methoxyethyl) ammonium TFSI at 353 K, using $Nd(TFSI)_3$ as the precursor [237]. They obtained – similar to other authors for other RE metals – one voltammetric cathodic peak at low potentials without corresponding anodic peak. From a more detailed analysis of the data they determined a diffusion coefficient of 1.25 x 10^{-9} cm^2 s^{-1} for the Nd(III) ion, which is even lower than the diffusion coefficients reported by Yamagata and Hussey for other ionic liquids. Also the kinetic rate constant was very low, in agreement with an irreversible reaction. Material electrodeposited potentiostatically was analyzed by SEM, EDS and XPS. The material deposited contained Nd metal, but also large amounts of oxides.

Extensive research on the structure [238-241], spectroscopy [239, 241] and in part electrochemical behavior [242, 243] of rare earth ions in ionic liquids was carried out by the group of Mudring. They even prepared ionic liquids with rare earth complexes as the anion [241, 244, 245]. The focus of the work was not, however, on metal electrodeposition.

These studies show that the electrodeposition of rare earth metals is feasible from ionic liquids, even though not really simple. The electrodeposition of Pt using standard Pt precursors from ionic liquids has been accomplished in literature as well [246, 247]. Therefore, also the co-

deposition of the alloy should be doable, but requires a careful adjustment of precursors, concentrations and applied potentials.

5 Electrocatalytic behavior of Pt(Pd)-rare earth alloys

Striving for low Pt catalysts, Pt-rare earth metal alloys have been identified as highly interesting materials. In research at DTU, both theoretical calculations using DFT and experimental studies on polycrystalline bulk alloys demonstrated the significantly improved activity of alloys such as Pt_3Y, Pt_5Gd, Pt_5Tb, Pt_5La, Pt_5Ce, Pt_3Sc and many others [5, 64, 88, 92, 94]. Typically, for the bulk samples, an activity enhancement between 1.5 and 6 was found, depending on the rare earth metal. As detailed before, those alloys are characterized by an inherently large negative enthalpy of formation, rendering them more stable towards dealloying than for instance in the case of some Pt-transition metal alloys [92]. It has been shown by DFT for Pt_3M alloys that the vacancy diffusion barrier for the minor element does scale with the formation enthalpy, explaining the improved stability [248]. The source of the enlarged activity is the formation of a stable Pt overlayer with a thickness in the range of 4-6 atomic layers. This Pt overlayer is under compressive strain, which alters the oxygen binding energy and moves the material closer to the maximum of the volcano plot. A negative consequence of the strain is a slightly reduced stability of the overlayer compared to pure Pt.

The ORR activity of Pt and its alloys with early transition metals namely: Pt_3Y, Pt_5Y, Pt_2Y, Pt_3Sc, Pt_3Hf and Pt_3Zr was investigated by Stephens et al. employing cyclic voltammetry in 0.1M $HClO_4$ and angle-resolved XPS (AR-XPS) [66]. Whereas the CVs of Pt_3Y, Pt_5Y and Pt_3Sc in N_2-saturated 0.1M $HClO_4$ showed a slight suppression of the onset of the H* adsorption suggesting a weaker interaction with H* as compared to pure Pt, that of Pt_2Y were up to 100 order of magnitude larger than pure Pt. Furthermore, once the electrode came in contact with the electrolyte, gas bubbles were formed. This observation, together with the increase in the CV

currents, was explained as a result of quick Y dissolution from this surface. Pt_3Y showed the highest ORR activity enhancement (6-9 fold at 23 ^oC and 4-6 fold at 60 ^oC) as compared to pure Pt. The activity enhancement of Pt_3Y and Pt_5Y was in accordance with their steeper Tafel slopes indicating a potential dependent slope. The above results explain again the main effect of alloying Pt with another metal, i.e. weakening of the Pt-O bond as understood due to the lateral compressive strain on the surface. As depicted from the results of AR-XPS, the most active catalyst, Pt_3Y, has a thick Pt-overlayer (10-15 Å with a negligible Y amount). It was also shown, however, for Pt_3Hf and Pt_3Zr that there is no Pt-overlayer formation instead, the surface is composed from a mixture of Pt and islands of HfO_x and ZrO_x which suggested a decrease in Pt sites and consequently explains the poor ORR performance of these alloys.

The effect of preparation methods, namely sputter cleaning and UHV annealing of polycrystalline Pt_3Sc on its structure as well as ORR activity have been investigated in vacuum, following exposure to 200 mbar O_2 and following ORR conditions [91]. The formation of a Pt overlayer has been established for Pt_3Sc prepared by UHV annealing. Despite the alloy's negative enthalpy of formation, Scandium oxide is formed on the surface as a result of Sc segregation upon exposure to 200 mbar O_2 as depicted from the AR-XPS depth profile. The above observation rules out the possibility of stable Pt skin formation for alloys of Pt with early transition metals unlike its alloys with metals as Ni, Co and Cu. The loss of Sc under reaction conditions presumably initiated by the direct interactions between oxygen containing adsorbates and Sc in the subsurface layer also explains the low ORR activity of such alloys. Although the Pt-skin structure of these alloys is not stable, dealloying under real fuel cell conditions is stabilized as Pt-skeleton structure due to their negative formation enthalpy. The ORR activity of both UHV annealed and sputter cleaned Pt_3Sc were similar in accordance with the similarities in their AR-XPS depth profiles. The activity

enhancement versus pure Pt was anticipated to be due to the presence of residual amount of Sc in the subsurface layer, i.e. ligand effect according to their DFT calculations. However, the enhancement due to the compressive strain effect was not excluded.

The activity and stability of Pt_5Gd for ORR have been explored by Escudero-Escribano et al. [88]. In an O_2-saturated 0.1M $HClO_4$ electrolyte, Pt_5Gd showed a pronounced positive shift relative to Pt (cf. Figure 14). Moreover, from the Tafel plot Pt_5Gd showed a 5-fold increase in the kinetic current density as compared to Pt. According to their DFT calculations, by alloying, the increase in the ORR activity was interpreted by means of a compressive strain effect which leads to a weakening of the binding between the catalyst and the oxygen containing intermediates such as OOH*, O* and OH*. From the analysis of the AR-XPS spectra before and after ORR experiments, it was evident that Gd was partially dissolved in the acidic electrolyte and a thick-Pt overlayer was formed. This layer presumably protects the Gd alloy bulk from dissolution in spite of the strong thermodynamic dissolution driving forces. A Pt_5Gd polycrystalline electrode exhibited good durability in O_2-saturated electrolyte after 10000 cycles between 0.6-1 V and 0.05-1.6 V vs. RHE at 23 °C. A slight decrease in the activity was observed and explained by the loss in the Gd from the near-surface region as depicted from the AR-XPS data.

RDE measurements carried out by Yoo et al. on their sputter-deposited Pt_3Y films (see section 4, after initial cycling) demonstrated a positive shift of the ORR half-wave potential by almost 100 mV, and an increase in area-specific activity by a factor of 16 [198, 249]. This was explained by a downward shift and widening of the d-band. Also in MEAs, a clear increase in performance compared to pure Pt was observed. RDE measurements on Pt_3La resulted in a half wave potential of 0.94 V during ORR and a specific activity of 1.5 mA cm^{-2} [199]. The stability of a series of

Pt_3M alloys was found to be correlated with the filling of the alloys' d-bands. This was analyzed in further detail by XANES. For Pt_3La it was concluded that a significant transfer of charge from the La to the Pt atoms is taking place [197, 199]. While in earlier work the enhanced ORR activity of Pt_3La was solely explained by the influence of alloying on d-band position and filling [197], the formation of a Pt skin was acknowledged in subsequent work [199].

More recently, Malacrida et al. studied sputter-cleaned polycrystalline Pt-La and Pt-Ce alloys using a combination of electrochemical techniques, AR-XPS and low energy ion scattering (LEIS) [92]. Polycrystalline Pt_5La and Pt_5Ce exhibited more than a 3-fold activity enhancement compared to polycrystalline Pt at 0.9 V, while Pt_3La heavily corrodes in 0.1M $HClO_4$ (Figure 15). Their work demonstrates that the highly reactive lanthanide atoms are not stable in the presence of oxygen, surface oxides are formed at the surface and they are dissolved in the electrolyte. A thick Pt overlayer is formed, preventing further oxidation and dissolution in the acidic electrolyte. This evidence is not consistent with the work reported by Yoo et al. for Pt-La alloys, where La appears in an oxidized state and is present on the electrode surface [197]. In the presence of the thick Pt overlayer reported by Malacrida et al., the activity enhancement on Pt_5La and Pt_5Ce can be only explained by strain effects.

Recently, Escudero-Escribano et al. systematically studied the ORR activity and stability trends of other polycrystalline Pt-lanthanide alloys: Pt_5La, Pt_5Ce, Pt_5Sm, Pt_5Gd, Pt_5Tb, Pt_5Dy and Pt_5Tm [94]. Pt_5Tb is the most active polycrystalline Pt-based catalyst ever reported. All the materials present a 3 to 6-fold activity enhancement over Pt. Interestingly, the ORR activity (kinetic current density measured at 0.9 V vs. the reversible hydrogen electrode, j_k (0.9 V vs. RHE)) versus the bulk lattice parameter follows a "volcano" relation (cf. Figure 16). Conversely, the lanthanide

contraction results in a voltammetric shift for H adsorption region, which resembles the activity volcano, with Pt_5Tb exhibiting the maximum destabilization of adsorbed H. In summary, the work by Escudero-Escribano shows that the lanthanide contraction, *i.e.* the decreased radius of the lanthanide atoms with increased filling of the f-shell, provides the ideal lever to engineer strain effects and tune the reactivity of the Pt overlayer and hence the performance of these materials.

In parallel with the work on polycrystalline-Pt alloys, Chorkendorff, Stephens, and co-workers have investigated Y- and Gd- modified Pt(111) (Y/Pt(111) and Gd/Pt(111)) single crystals, in order to gain a further insight on both the structure and the ORR activity enhancement [86, 87, 90]. Y/Pt(111) and Gd/Pt(111) were prepared under ultra-high vacuum (UHV), simulating a bulk Pt-Y and Pt-Gd, respectively. The Y/Pt(111) and Gd/Pt(111) samples were characterized by low-energy electron diffraction (LEED), XPS, ion scattering spectroscopy (ISS) and TPD of CO [86, 90]. A Pt overlayer was formed upon annealing the Y/Pt(111) and Gd/Pt(111) single crystals. LEED shows the formation of a slightly compressed (2x2) structure [87, 90]. The samples were then taken out the UHV chamber in order to measure the electrochemical ORR activity [86, 90]. Y/Pt(111) and Gd/Pt(111) electrodes exhibit a 4-fold improvement over Pt(111). Surface sensitive X-ray diffraction reveals the formation of crystalline closely packed Pt overlayers after electrochemistry on both alloys [86].

The rather small differences between Pd and Pt as pure metals can become striking in rare earth elements alloys as very nicely highlighted in a recent study by Tripkovic et al. [250]. The authors compared the activity of polycrystalline the Pd_5Ce alloy with that of the homologous Pt_5Ce. Although DFT modelling pointed out that compressively strained Pd overlayers should be even

more active than Pt (cf. Figure 17), the electrochemical analysis in $HClO_4$ clearly showed that the activity towards ORR is even less than in the case of pure polycrystalline Pd (see Figure 18). Detailed XPS and AR-XPS analysis of the surface after the electrochemical measurements showed the expected decrease of the Ce amount with formation of an about 10 Å thick Pd-skin. This unexpected behavior was demonstrated to be due to the presence of two crystal phases, H-Pd_5Ce and L-Pd_5Ce, as verified by XRD analysis, with a strong presence of the latter in the bulk and to an even greater extent on the surface. The L-Pd_5Ce phase, stable at room temperature, is a cubic $L1_2$ structure where, the Pd overlayer that forms on top, is under tensile strain implying a decrease in activity compared to non-strained Pd. The transformation from the H-Pd_5Ce phase, that forms at high temperature and is characterized by a compressive strain of the Pd atoms, to the L-Pd_5Ce phase was shown to occur only in the case of Pd rare earth alloys and not in the case of Pt because of the slightly different arrangement of the Ce atoms in H-Pt_5Ce and H-Pd_5Ce that greatly facilitate, in the latter case, the transformation from the H-phase to the L-phase.

More recently, Brandiele et al. studied the activity and stability of Pt_xY NPs for ORR in an O_2-saturated 0.1M $HClO_4$ electrolyte [212]. The Pt_xY catalyst with *ca* 41% of the Y atoms alloyed with the Pt showed a remarkably higher half-wave potential (0.891 V vs. RHE), specific activity and mass activity (1.570 mA cm^{-2}_{Pt} and 0.586 A mg^{-1}_{Pt}, respectively) than that of a Tanaka standard. Catalyst durability was tested in accelerated degradation tests (ADT) by cycling the potentials (10000 cycles) in the range of 0.6–1.05 V (vs. RHE) in O_2-saturated 0.1M $HClO_4$ solution. The specific activity for Pt_xY after ADT (0.905 mA cm^{-2}_{Pt}) still respects the 2017 DOE target (0.7 mA cm^{-2}_{Pt} at 0.9 V vs. RHE), whereas the mass activity (0.29 A mg^{-1}_{Pt}), even though lower than the target (0.44 A mg^{-1}_{Pt}), still remains very high (Figure 19).

6 Catalyst Support Materials

Aside from the strive for catalysts with ultralow Pt loading or even noble-metal free catalysts, a topic not discussed in this review, also for Pt catalysts improvements can be expected by the use of advanced support materials. This section focusses on two types of support materials, and there the main emphasis lies on results obtained within the CathCat project. A comprehensive review is not intended.

6.1 Carbon-based

The performance of a catalyst, particularly NP catalyst, is the result of many chemical and physical properties, since it is a quite complex system: chemical composition of NPs, of the support material and of the electrolyte; physical aspects such as facets, surface defects of the support, size of NPs, and so on. Among such properties, which influence the electrocatalytic activity, selectivity and stability of catalytic NPs, the characteristics of support material and interaction between support material and catalyst appear to play a fundamental role.

The most used support material is based on carbon in its different formulation, based in any case on graphite allotropic form. In addition to carbon, the presence of purposely added heteroatoms, such as B, N, S, can modify the surface physico-chemical properties and exercise specific chemical interactions with the catalyst NPs.

As a proof of concept the most inert carbon material, i.e. glassy carbon was employed for investigating the effect of nitrogen doping on the electrocatalytic activity of Pd NPs [130]. As a case study, the electrochemical reduction of carbon-halogen (C–X) bond was investigated, since the exceptional electrocatalytic activity of Pd in the C–X bond breaking is well known and documented. Nitrogen doping was obtained through ion implantation by an ion gun with N_2 (N-GC) or, for comparison, Ar background (Ar-GC). In fact, since ion implantation produces morphological defects, it was necessary to disentangle the effects of the presence of new N functional groups from those related to the presence of defects. Pd NPs were deposited by a double step potentiostatic metod from 1mM $PdSO_4$ + 0.1M H_2SO_4. Comparison between pristine (Pd@GC), N (Pd@N-GC) and Ar (Pd@Ar-GC) doped GC, revealed that Pd NPs are smaller on Ar-GC than in pristine GC, but they resulted smaller and higher dispersed on N-GC than Ar-GC. As a result, the electrocatalytic activity in the reduction of benzyl chloride, as a sort of benchmark for the electrocatalytic reduction of C–X bond, in the case of Pd@N-GC resulted higer than Pd@Ar-GC, which was quite similar to that of Pd@GC. Furthermore, the electrocatalytic activity of Pd@N-GC was higher also than that of bulk Pd. This means that specific interactions between Pd NPs and N atoms play an important role.

The results obtained on GC induced the investigation of a more structured carbon material such as HOPG, in particular by a combined electrochemical and surface science approach. Nitrogen-doped HOPG (N-HOPG) was used as substrate to investigate the influence of nitrogen functional groups to the activity and stability of electrodeposited supported Pd NPs [251]. Five different nitrogen components have been identified by XPS, which are sp^2 C-N bonds containing pyridinic, pyrrolic and substantial nitrogen defects, -C≡N terminal groups and trapped nitrogen ions in graphite vacancies. An increased oxidation state of Pd at the interface between Pd NPs and

substrates was detected by X-ray photoelectron spectroscopy (XPS) due to the strong electron withdrawing force of nitrogen functional groups. The oxidized Pd was vulnerable at oxidation potentials such that the stability of the Pd NPs became lower. A support effect on the activity of Pd NPs for ORR was not observed in this work, actually both Pd/N-HOPG and Pd/HOPG showed nearly identical ORR behavior. Nitrogen doped HOPG, prepared by ion implantation, has been characterized by spectroscopic techniques using synchrotron radiation [200]. This allowed to tune the doping dose and the typology of the introduced chemical defects, that is to select the different functional groups by adjusting the annealing temperature adopted after the ion implantation. On doped (N-HOPG) and non-doped HOPG, electrocatalyst NPs based on the deposition of Pd and Y in well-controlled ultra-high-vacuum (UHV) conditions were investigated. The formation of Pd_3Y alloy was confirmed by a binding energy shift due to a partial *d-d* hybridization, which leads to a charge transfer between Y and Pd. Furthermore, the presence of a significant amount of yttria (Y_2O_3) was revealed, confirming the very high affinity of Y for oxygen, which was scavenged by Y also in the UHV conditions, but the presence of such an oxide is not detrimental for the electrocatalytic activity toward ORR.

Porous carbon is an interesting support material for ORR, because catalyst NPs can be well dispersed. In this framework, mesoporous carbons have been largely investigated, thanks to the very high porosity, which allows very large specific surface area, high electrical conductivity, chemical inertness and easiness of production. Much attention has been devoted to two issues: the enhancement of catalytic activity, in particular by doping MC with heteroatoms, such as N and/or S; the stability of the catalyst NPs.

MCs prepared by a hard template procedure, using porous silica as templating and an organic precursor as source of carbon, have been prepared as support for the deposition of Pt or Pd NPs. For example [110] sucrose was utilized for non-doped MC, whereas ammonia was the source of N in the N-doped MC (N-MC). On such supports, Pt or Pd NPs were deposited by chemical reduction of the corresponding salts mixed with the MC support. It was observed that the presence on N favors the formation of smaller catalyst NPs, which were less prone to aggregation. Furthermore, N-MC enhances the catalytic activity of both Pt and Pd NPs, as revealed by the higher values of onset potential E_{onset} and half wave potential $E_{½}$ of ORR, in linear sweep voltammetry with rotating disk electrode, and by the increase of the electrochemical active surface area. In any case, a four electrons ORR, leading to the direct reduction to water, was obtained as the main reduction process. XPS investigations revealed a chemical interaction between catalyst NPs and N defects in N-MC. In the case of Pt on N-MC, the performances were better than that of a commercial Vulcan XC-72 with the same loading of Pt. Moreover, catalyst NPs showed a higher stability with respect to Pt-Vulcan, thanks to a better confinement of Pt NPs in the mesoporous structure.

The doping of MCs was further extended to sulfur doped or co-doped materials, with the aim of preparing metal-free electrocatalysts [252]. In this case doping was obtained by an appropriate choice of the organic precursors for the hard template production of MCs (such as 1,10-phenantroline, carbazole and indigo carmine for N-MCs; dibenzothiophene for S-MC and phenothiazine for N,S-MC, whereas phenanthrene was employed for the synthesis of non-doped MC). Very good MCs were obtained, with a surface area >850 $m^2 g^{-1}$, mesoporosity of 3-4 nm diameter and a content in doping heteroatoms in the range 3-8% and 4-14% for nitrogen and sulfur, respectively. These doped MCs were utilized as metal-free electrocatalysts in the ORR,

showing a positive shift of E_{onset} ranging from 300 to 400 mV, with respect to commercial MC. The catalytic activity increases with increasing content of N, whereas S plays an opposite effect. In any case, all the synthetized MCs were selectively active for the two electrons ORR with the production of H_2O_2.

One of the key aspects of the use of carbon materials in electrochemical devices is related to their stability, being subject to strong electrochemical stresses. Nitrogen and sulfur doped or co-doped MCs, prepared by hard template production starting from appropriate organic precursors containing the doping heteroatoms, were tested by *ex situ* ADT, consisting in two thousand voltammetric cycles in an appropriate potential window, in Ar purged 0.5M H_2SO_4, 0.1M $HClO_4$ or 0.1M KOH solutions. After such an ADT, the MC was investigated by different spectroscopic techniques, thermal gravimetric analysis and voltammetric experiments [253]. In alkaline solution the chemical and morphological stabilities were verified, whereas in acidic solutions, a relevant modification of the nitrogen chemical groups was observed, since pyridinic and pyrrolic functional groups resulted less stable, while N-graphitic and thiophenic groups preserved their stability. After ADT tests, the electrocatalytic properties toward ORR in acidic media decreased, whereas in alkaline media the decrease was lower. Such a decrease in catalytic activity was related to the degradation of pyridinic and pyrrolic groups, which are considered the most active sites for ORR.

Graphene and graphene oxide (GO) and doped variants thereof have also been considered in recent years as potential ORR catalysts or catalyst support materials. In the framework of the CathCat project, the group at the University of Padova has explored the potential of doped GO quantum dots (QDs, often also termed a nanoplatelets) as ORR metal-free catalysts. Singly and

multiply doped GO-QDs have been synthesized by a simple electrochemical method using water as solvent [254]. The obtained materials have been characterized by XPS and scanning tunneling microscopy (STM), in order to get a detailed picture of their chemical and structural properties. The electrochemical activity toward ORR of the doped GO-QDs dots has been investigated by CV and RDE measurements, showing a clear decrease of the overpotential as a function of the dopant according to the sequence: N ~ B > B,N [255-257]. Moreover, assisted by DFT calculations of the Gibbs free energy associated with every electron transfer, it has been demonstrated that the selectivity of the reaction is controlled by the oxidation states of the dopants: as-prepared doped GO-QDs follow a two-electron reduction path that leads to the formation of hydrogen peroxide, whereas after the reduction with $NaBH_4$, the same materials favor a four-electron reduction of oxygen to water [255].

A general overview on carbon-based supports was provided by Ma and Alonso-Vante. Their review covered topics like carbon nanotubes (CNT) and nanofibers (CNF) as well as graphene and related compounds [106]. Subsequently, the review by Luo and Alonso-Vante distinguished between low- (glassy carbon electrode, GCE and carbon black, CB) and high-graphitized carbons (CNT and reduced graphene oxide, RGO) [107]. The activity of various catalysts supported on the carbon black was described. The authors emphasized that the best performing ones reported are Pt_xY/GCE, $Pt_{2.5}Ni$/CB, $Pt_{1.5}Ni$/CB and PtNi/CB. It was shown that those catalysts showed an ORR kinetics before and after stability tests that was higher than targeted by DOE for 2015/2017. When high-graphitized carbons are used as supports an improvement in the stability of the catalysts was detected with respect to CB. This was explained with higher corrosion resistance of the substrate and the strong metal substrate interaction effect (SMSI) in the case of use of high-graphitized carbon as a substrate.

6.2 Oxides

The influence of oxide-based supports has been nicely summarized by the above mentioned reviews from the group of Alonso-Vante [106, 107]. The review by Ma and Alonso-Vante already discussed the SMSI effect and its physical background involving a shift in the 4f levels of the Pt NP, also for conductive oxide and oxide/carbon composite support materials [106]. The stability and improved corrosion resistance of supports from oxides and hydroxides from "Ti, W, Sn, Nb, Ta, and Sb" under fuel cell conditions was pointed out [106, 107]. Especially materials based on TiO_2, WO_3, SnO_2, ZrO_2 and TaO_2 are of importance, but also doped oxides. Oxide carbon composites have a better conductivity than oxides alone, and Pt supported on these supports shows enhanced ORR activity and CO tolerance and in part better stability compared to Pt/C [106, 107].

S. Mokrane-Soulah et al. investigated nanostructured tungsten doped titania as a support for (photo)-electrochemical processes, especially with respect to metal deposition [258]. The titania was synthesized via a multistep sol-gel process. The tungsten content was varied between 1 and 30 at%. An increase of the W content led to the decrease in the photo-response and an increase of the electronic conductivity of the samples. Furthermore, the sample with 20 at% of tungsten, i.e. $Ti_{0.8}W_{0.2}O_2$, was used as support for platinum. The activity for the ORR reaction was examined and compared to Pt/C (Vulcan). The Tafel plots showed an enhancement of the reaction kinetics when Pt was deposited on the mixed oxide. The kinetic currents at 0.85V vs RHE for Pt/C and Pt/ $Ti_{0.8}W_{0.2}O_2$ were 15 and 29 μA cm^{-2}_{Pt}, respectively, showing a two-fold increase for the ORR activity when using $Ti_{0.8}W_{0.2}O_2$ instead of C as the Pt support.

Estudillo-Wong et al. investigated titania-carbon (TiO_2-C) and yttrium-doped titania-carbon composites (Y:TiO_2-C), synthesized via a sol-gel method and used as supports for Pt nanoparticles [259]. The photodeposition method resulted in a selective Pt deposition on the oxide and less deposition on carbon, different to other techniques. The ORR activity and stability of the modified catalysts were studied and compared to the Pt/C catalysts, prepared via the same method. The smallest particle size was found for the sample with TiO_2-C as support. From TEM the authors concluded that Pt NPs in all samples expose the same facets. The mechanism of ORR was found to be similar for all samples. The SA was highest for the Pt/Y:TiO_2-C and lowest for the Pt/TiO_2-C sample. The MA and ECSA showed the opposite trend, they were highest for the Pt/TiO_2-C and lowest for the Pt/Y:TiO_2-C sample. Further, samples with Y:TiO_2–C and TiO_2-C composites depicted better corrosion resistance. Overall, the modification of the carbon with Y:TiO_2 had a positive influence on the stability of the support and ORR kinetics of the supported catalysts.

Luo and co-authors synthesized a novel Pt/CeO_x/C nanocomposite via the carbonyl chemical route using a Ce-containing metal organic framework (MOF) as precursor [206]. The chemical synthesis was followed by a heat treatment at up to 900 °C under Ar atmosphere. Multi-walled carbon nanotubes were chosen as carbon material. For comparison, also catalyst without MOF was prepared under otherwise identical conditions. A unique nanostructure was found for the sample with MOF present and heated at 900 °C in respect to the samples without MOF or heated at lower temperatures. Almost no agglomeration and nicely dispersed ~ 5nm nanoparticles, coated by ceria layer formed from the MOF (structure impossible to be reveled without HRTEM) were detected. The ceria stabilized the Pt NPs. The electrocatalytic activity of the all prepared samples was investigated and it was found that the sample with MOF addition heated to 900 °C

has an improved performance compared to the commercial catalysts and other samples investigated. Especially, this sample had higher surface specific (SA) and mass activities (MA) for ORR than those targeted by DOE for 2015/2017. In addition, the sample showed improved stability during cycling and no agglomeration of the particles. The authors concluded that the specific interaction of Pt-CeO_x as a result of the unique Pt/CeO_x/C morphology is responsible for the catalytic and stability enhancement.

7 Catalyst testing

Whenever new cathode catalysts are developed, testing of these catalysts for activity and stability are mandatory for their evaluation. The most reliable data for catalyst performance are obtained by testing within actual MEAs. However, MEA fabrication and testing are time-consuming, require adequate instrumentation and accurate control of gas pressures, temperatures and humidities, and relatively large amounts of catalyst material. Therefore, half-cell tests in aqueous electrolytes are preferred for initial screening. The most often used technique is characterization with a rotating disc electrode, by depositing a catalyst layer through ink application onto the surface of a glassy carbon electrode embedded in a RDE holder [12, 13, 260]. The technique aims at determination of the actual kinetic current at 0.9 V vs RHE as a performance criterion, and does not permit to operate at current densities typical for the actual fuel cell application. An early review including such measurements was given in the work by Gasteiger et al. [12] using loadings between 12 and 50 μg_{Pt} cm^{-2} depending on the type of catalyst used. For analysis typically the positive going sweep was used, at low scanrates up to 20 mV s^{-1} in order to minimize capacitive background currents [12]. At 5 mV s^{-1}, however, lower activities were

observed which was explained by the larger amount of OH_{ads} on the surface [12]. The authors also mentioned the risk of impurity adsorption.

Mayrhofer et al. applied the technique at 20°C and 60°C to Pt/C catalysts of different particle size and NTSF catalysts, and studied the role of the experimental conditions, especially because a large discrepancy of findings reported in literature [42]. The determination of the active surface area by the H_{UPD} method (using the anodic sweep) resulted in lower Pt surface areas than the values determined from CO stripping, which was explained by a potential-dependent contribution of the support capacitance to the total capacitive background, that needs to be corrected for before applying the simpler correction for the Pt capacitance. In addition, the loading was crucial and different dependent on the catalyst type. Too small loadings resulted in incomplete coverage leading to reduced diffusion currents, while too large loadings introduced additional terms into the mass transport (layer thickness no longer small compared to diffusion layer thickness) and reduced the potential range where the mass transport contribution can be reliable corrected.

Recently, several groups re-evaluated the RDE method, an activity also supported by the US DOE. An up to date overview was reported by Pedersen et al. [261]. They used the RDE method and focused on ORR and hydrogen oxidation reaction (HOR) in the presence of CO employing both flame-annealed polycrystalline Pt and carbon supported nanoparticle electrodes. In benchmarking ORR catalysts, it was shown that increasing temperature from 23 to 60 °C can improve the ORR specific activity for Pt/C catalyst by up to 26% comparing to polycrystalline Pt where the activity increase was negligible within the experimental error bar. Investigating the effect of scan rate, *IR* drop compensation and capacitive current subtraction during the ORR measurements showed a remarkable activity dependence. Experimental results showed that doing

the above precautions lead to a much reliable ORR activity and the recommendation with respect to scan rate was to use 20 or 50 mV s^{-1} due to the capacitive contribution of the current density, which increases linearly with the scan rate. Crucial to the fuel cell applications the study of the CO tolerance catalytic activity at low potentials (0.1-0.4 V) is of much greater importance thus the authors also focused on the CO tolerance of different electrocatalysts including Pt/C and PtRu/C at these potentials and recommended the best experimental conditions and CO concentration for benchmarking CO poisoning during the HOR. First, using 2% instead of 100 ppm CO concentration in H_2 was recommended to achieve fast poisoning where the poisoning rate using 100 ppm CO concentration in H_2 was found to be very slow at both polycrystalline Pt and Pt/C nanoparticle catalysts presumably due to the low content of CO molecules reaching to the surface. A required poisoning time by CO was crudely calculated to be 18.1 min for polycrystalline Pt comparing to 2.7 hours for Pt/C catalyst. The PtRu/C catalyst at 0.1-0.35 V showed an order of magnitude higher CO oxidation mass and specific activities comparing to Pt/C catalyst due to the electronic effect of Ru.

A comprehensive description of the experimental precautions involving glassware cleanliness, electrode film quality, electrolyte choice and purity that should be taken in to account during benchmarking the ORR commercial catalysts were reported by Garsany et al. [262]. All glassware should be cleaned thoroughly in conc. H_2SO_4 (8 h), 1:1 mixture of H_2SO_4 + HNO_3 (2-4 h) or 1:1 mixture of H_2SO_4 + Nochromix (4 h) then thoroughly rinsed with nanopure water and boiled twice then finally rinsed with the supporting electrolyte. A cleanliness test could be done afterwards by cycling the Polycrystalline Pt electrode in the electrolyte and obtaining a specific activity at E = 0.9 V of ca. 1500-3000 μA. A freshly prepared RHE reference electrode using mesh platinized Pt is recommended and a high purity grade chemicals should be used. Fresh (not

used) 0.1M $HClO_4$ rather than 0.5M H_2SO_4 is recommended as a supporting electrolyte due to slow (negligible) ClO_4^- ion adsorption comparing to SO_4^{2-}. A thin-film of Pt ($\leq$ 0.2 μm) with a Pt loading of 7-30 μg_{Pt} cm^{2-} on well-polished Glassy carbon disc is recommended to achieve a controllable mass-transport resistance through the catalyst layer. A uniform homogeneous catalyst film on the surface of the Glassy carbon electrode should achieved by a delicate balance between alcohol content and type, Pt dispersion and drying conditions. During the electrochemical measurements, the temperature should be controlled by an external thermostat ensuring 30 °C as a fixed room temperature. The height of the working should be positioned every time the same to keep the same solution resistance between working and reference electrodes. Potential drop compensation and capacitive current background correction should be applied in order to obtain reliable results.

Based on the difficulty of obtaining a uniform electrocatalysts thin-film needed for the reliable/reproducible data for the ORR activity during benchmarking commercial Pt/C catalysts, Garsany et el. reported on a method for making reproducible smooth thin-film electrocatalysts [263]. Topology and Morphology of a thin-film Pt/C on a smooth Glassy carbon surface have been studied by Optical Microscope, SEM and 3D optical Profilometer. After preparation and well dispersion of the catalyst ink, 7.5-10 μL of the ink was drop-casted on the Glassy carbon disc and then allowed to dry either stationary or by rotating at 700 rpm. In case of stationary drying, the optical methods clearly proved the formation of non-uniform catalyst layer (coffee ring) on the disc with a dense layer on the edge and thinner layer on the center of the disc. In contrast, in case of spin-rotation drying, a uniform catalyst layer was formed and proved by the above optical techniques. The authors explained the morphology difference between the two drying methods based on the mechanism of drying: in case of stationary drying, an outward

capillary flows from the center of the disc to the edge to compensate the solvent lost due to faster evaporation at the edge. This results in accumulation of the solute in the edge and formation of highly inhomogeneous coffee ring structure. In contrast, the catalyst film formed by spin rotational drying method was highly homogeneous, dense and covered all of the disc surface. Due to the centrifugal force and centripetal acceleration, the film will spread out off of the disc edges ending with a thin uniform film with no surface defects after drying. Under these conditions, one expects a lower O_2 diffusion resistance in the electrode and therefore higher ORR kinetic current densities. Indeed, the complete picture of comparison became clearer when performing the electrochemical measurements using a glassy carbon drop-casted commercial catalysts dried by stationary or rotation methods. Although, the difference in the obtained ECSA between the two drying methods was negligible (within the error bar) presumably due the morphology independent fast cyclic voltammetry, the difference in ORR activities were very clear. The uniform catalyst film obtained by rotational drying exhibited higher ORR activates than that of stationary film. Furthermore, not only the ORR activities were higher but also the authors were able to get a fairly reproducible results with the rotational drying technique by comparing the activities of 7 consecutive rotational drop-casting trails. The main conclusion is *''it is possible that a uniform thin catalyst film be obtained by stationary drying method but it is very inconsistent''*. On the other hand, a catalyst drop-casted carefully (only on the Glassy carbon disc not the Teflon cup) and dried by rotating the disc at 700 rpm could give a uniform/reproducible catalyst film and consequently results in a more reliable benchmarking results.

Recently, the same authors reported on a detailed recommendations for the experimental and technical procedures that results in an reliable and reproducible ORR benchmarking results [264].

A catalyst ink formulation, *i.e.* water: alcohol ratio of 80:20 was recommended for Pt/C catalyst and it should be well mixed leading in the end to a homogeneous mixture. A uniform catalyst thin-film should be achieved by rotational drying technique after drop-casting and the formation of ‘’coffee ring’’ structure should be avoided which acts as an indication of the non-uniform catalyst thin-film and consequently, as discussed above, affects the ORR activities. As potential scan rates of 5 and 20 mV s^{-1} are recommended. Scan rates lower than 5 mV s^{-1} increases the chances for impurities accumulation in the electrolyte and working electrode and higher than 20 mV s^{-1} increases the capacitive current contributions. A Pt loading low enough for the formation of a thin catalyst film and in the same time enough for an accurate measurement is recommended. The authors recommended a catalyst loading of 5 to 20 μg_{Pt} cm^{-2}. A rotation speed of 1600 rpm is recommended during the RDE experiments and the mass and surface catalyst activities must be obtained from a potential near to the half-wave potential typically 0.9 V vs. RHE for Pt/C. A correction of the potential drop and the capacitive current should be done to obtain a reliable activities and finally all chemical and gases should be extra pure grades and a fresh "not used" 0.1M $HClO_4$ should be used as a supporting electrolyte due to the low adsorption of perchlorate anion.

Apart from simple electrochemical testing using a rotating disc electrode, combination with additional methods can provide more in-depth information. This concern the application of techniques like the electrochemical quartz crystal microbalance technique [265], analytical techniques like ICP, and also optical methods [266-268]. Especially techniques like direct and indirect nanoplasmonic sensing are probably suitable to learn more about actual catalyst materials [267, 268]. Wickman et al. showed for 20 and 100 nm thin Pd films, that even combining electrochemical measurements with simple in-situ UV-VIS spectroscopy permits a more in-depth

understanding of processes taking place during surface oxidation and the Pd hydride formation [266]. The authors showed that the α-phase forms homogeneously throughout the Pd film, but that the β-phase forms first at the metal/electrolyte interface. On the other hand, decomposition starts at the interface not in contact with electrolyte.

Shinozaki et al. discussed several procedures for RDE catalyst testing using polycrystalline Pt as a test system to verify the appropriateness of the selected protocols [269]. Especially in catalyst testing of alloys catalysts thorough cleaning before the next experiment is necessary. The impurity level of the perchloric acid solution is also very important. The choice of the acid concentration is determined by a compromise between conductivity and the impurity level. For initial catalyst conditioning an upper potential of at least 1.1 V was required in order to develop the characteristic Pt features in the voltammogram. For the actual ORR measurements, the authors recommend to use lower potentials below 0.1 V to completely reduce surface oxides, to evaluate the anodic sweep, and to select a scan rate of 20 mV^{-1} (compromise between build-up of oxides and impurities at low scan rates and increasing contribution of background correction at higher scan rates). The authors also considered the impact of ink composition and catalyst layer fabrication [270]. They found highest activities and most homogeneous films when omitting Nafion from the catalyst ink, but adding a non-ionic surfactant, and evaporating the solvent slowly at 40°C in an oven under isopropanol vapor.

In 2013, Zalidis and co-authors introduced a new characterization technique not suffering from the mass transport limitations of the RDE [152]. They adjusted a floating electrode technique to work with ultrathin catalyst loadings. As substrate, they used a porous, gold-coated polycarbonate membrane, onto which the catalyst was homogeneously deposited by vacuum-filtration. The

catalyst layer was immersed in the electrolyte, onto which the porous electrode floated, while the oxygen was directly supplied through the pores from the backside of the membrane, thus eliminating mass transport limitations typical for ORR. Geometric current densities of close to 200 mA cm^{-2} could therefore be obtained.

Acknowledgments

The research leading to some of the results summarized in this paper has received funding from the European Union's Seventh Framework Programme (FP7/2007–2013) for the Fuel Cells and Hydrogen Joint Technology Initiative under grant agreement no. [303492], within the CathCat project, which is gratefully acknowledged.

References

[1] *International Energy Outlook 2016,* U. S. E. I. Administration, http://www.eia.gov/forecasts/ieo/, **2016**

[2] F. T. Wagner, B. Lakshmanan, M. F. Mathias, *J. Phys. Chem. Lett.* **2010**, *1*, 2204-2219.

[3] O. Gröger, H. A. Gasteiger, J.-P. Suchsland, *J. Electrochem. Soc.* **2015**, *162*, A2605-A2622.

[4] Y. Nonobe, M. Nada, N. Watanabe, K. Umayahara, Y. Naganuma, T. Hasegawa, *Toyota Tech. Rev.* **2015**, *61*, 15-19.

[5] I. E. L. Stephens, A. S. Bondarenko, U. Gronbjerg, J. Rossmeisl, I. Chorkendorff, *Energy Environ. Sci.* **2012**, *5*, 6744-6762.

[6] *Fuel Cell technical Team Roadmap,* energy.gov/sites/prod/files/2014/02/f8/fctt_roadmap_june2013.pdf, **2013**

[7] *V.D.1 Advanced Cathode Catalysts and Supports for PEM Fuel Cells,* U. D. o. Energy, http://www.hydrogen.energy.gov/pdfs/progress12/v_d_1_debe_2012.pdf, **2012**

[8] D. Papageorgopoulos, *Fuel Cells Program,* U. D. o. Energy, https://www.hydrogen.energy.gov/pdfs/review15/fc000_papageorgopoulos_2015_o.pdf, **2015**

[9] http://www.fuelcelltoday.com/news-archive/2013/october/toyota-unveils-prototype-fuel-cell-vehicle

[10] J. K. Norskov, J. Rossmeisl, A. Logadottir, L. Lindqvist, J. R. Kitchin, T. Bligaard, H. Jonsson, *J. Phys. Chem. B* **2004**, *108*, 17886-17892.

[11] A. U. Nilekar, M. Mavrikakis, *Surf. Sci.* **2008**, *602*, L89-L94.

[12] H. A. Gasteiger, S. S. Kocha, B. Sompalli, F. T. Wagner, *Appl. Catal., B* **2005**, *56*, 9-35.

[13] U. A. Paulus, T. J. Schmidt, H. A. Gasteiger, R. J. Behm, *J. Electroanal. Chem.* **2001**, *495*, 134-145.

[14] H. A. Hansen, J. Rossmeisl, J. K. Norskov, *Phys. Chem. Chem. Phys.* **2008**, *10*, 3722-3730.

[15] V. Stamenkovic, B. S. Mun, K. J. J. Mayrhofer, P. N. Ross, N. M. Markovic, J. Rossmeisl, J. Greeley, J. K. Nørskov, *Angew. Chem., Int. Ed.* **2006**, *45*, 2897 –2901.

[16] J. Rossmeisl, G. S. Karlberg, T. Jaramillo, J. K. Nørskov, *Faraday Discuss.* **2008**, *140*, 337-346.

[17] V. Tripković, E. Skúlason, S. Siahrostami, J. K. Nørskov, J. Rossmeisl, *Electrochim. Acta* **2010**, *55*, 7975-7981.

[18] V. Viswanathan, H. A. Hansen, J. Rossmeisl, J. K. Nørskov, *ACS Catal.* **2012**, *2*, 1654-1660.

[19] V. Viswanathan, H. A. Hansen, J. Rossmeisl, J. K. Nørskov, *J. Phys. Chem. Lett.* **2012**, *3*, 2948-2951.

[20] A. S. Bandarenka, H. A. Hansen, J. Rossmeisl, I. E. L. Stephens, *Phys. Chem. Chem. Phys.* **2014**, *16*, 13625-13629.

[21] V. Tripković, I. Cerri, T. Bligaard, J. Rossmeisl, *Catal. Lett.* **2014**, *144*, 380-388.

[22] N. Bonnet, M. Otani, O. Sugino, *J. Phys. Chem. C* **2014**, *118*, 13638-13643.

[23] F. Abild-Pedersen, J. Greeley, F. Studt, J. Rossmeisl, T. R. Munter, P. G. Moses, E. Skúlason, T. Bligaard, J. K. Nørskov, *Phys. Rev. Lett.* **2007**, *99*, 016105.

[24] T. Bligaard, J. K. Nørskov, *Electrochim. Acta* **2007**, *52*, 5512-5516.

[25] M. Mavrikakis, B. Hammer, J. K. Nørskov, *Phys. Rev. Lett.* **1998**, *81*, 2819-2822.

[26] B. Hammer, J. K. Norskov, *Adv. Catal.* **2000**, *45*, 71-129.

[27] H. E. Hoster, O. B. Alves, M. T. M. Koper, *ChemPhysChem* **2010**, *11*, 1518-1524.

[28] S. Kattel, G. Wang, *J. Chem. Phys.* **2014**, *141*, 124713.

[29] J. R. Kitchin, J. K. Nørskov, M. A. Barteau, J. G. Chen, *Phys. Rev. Lett.* **2004**, *93*, 156801.

[30] F. Calle-Vallejo, J. Tymoczko, V. Colic, Q. H. Vu, M. D. Pohl, K. Morgenstern, D. Loffreda, P. Sautet, W. Schuhmann, A. S. Bandarenka, *Science* **2015**, *350*, 185-189.

[31] C. H. Kjaergaard, J. Rossmeisl, J. K. Nørskov, *Inorg. Chem.* **2010**, *49*, 3567-3572.

[32] S. Trasatti, *J. Electroanal. Chem.* **1972**, *39*, 163-184.

[33] R. Parsons, *Trans. Faraday Soc.* **1958**, *54*, 1053-1063.

[34] M. Nesselberger, M. Roefzaad, R. Fayçal Hamou, P. Ulrich Biedermann, F. F. Schweinberger, S. Kunz, K. Schloegl, G. K. H. Wiberg, S. Ashton, U. Heiz, K. J. J. Mayrhofer, M. Arenz, *Nat. Mater.* **2013**, *12*, 919-924.

[35] M. Nesselberger, S. Ashton, J. C. Meier, I. Katsounaros, K. J. J. Mayrhofer, M. Arenz, *J. Am. Chem. Soc.* **2011**, *133*, 17428-17433.

[36] D. Li, C. Wang, D. S. Strmcnik, D. V. Tripkovic, X. Sun, Y. Kang, M. Chi, J. D. Snyder, D. van der Vliet, Y. Tsai, V. R. Stamenkovic, S. Sun, N. M. Markovic, *Energy Environ. Sci.* **2014**, *7*, 4061-4069.

[37] B. E. Hayden, *Acc. Chem. Res.* **2013**, *46*, 1858-1866.

[38] A. Anastasopoulos, J. C. Davies, L. Hannah, B. E. Hayden, C. E. Lee, C. Milhano, C. Mormiche, L. Offin, *ChemSusChem* **2013**, *6*, 1973-1982.

[39] G. A. Tritsaris, J. Greeley, J. Rossmeisl, J. K. Nørskov, *Catal. Lett.* **2011**, *141*, 909-913.

[40] M. Shao, A. Peles, K. Shoemaker, *Nano Lett.* **2011**, *11*, 3714-3719.

[41] G.-F. Wei, Z.-P. Liu, *Phys. Chem. Chem. Phys.* **2013**, *15*, 18555-18561.

[42] K. J. J. Mayrhofer, D. Strmcnik, B. B. Blizanac, V. Stamenkovic, M. Arenz, N. M. Markovic, *Electrochim. Acta* **2008**, *53*, 3181-3188.

[43] R. A. Martínez-Rodríguez, F. J. Vidal-Iglesias, J. Solla-Gullón, C. R. Cabrera, J. M. Feliu, *ChemPhysChem* **2014**, *15*, 1997-2001.

[44] L. Du, S. Zhang, G. Chen, G. Yin, C. Du, Q. Tan, Y. Sun, Y. Qu, Y. Gao, *ACS Appl. Mater. Interfaces* **2014**, *6*, 14043-14049.

[45] R. Devivaraprasad, R. Ramesh, N. Naresh, T. Kar, R. K. Singh, M. Neergat, *Langmuir* **2014**, *30*, 8995-9006.

[46] A. Toge, T. Yokono, M. Saito, H. Daimon, A. Tasaka, M. Inaba, *ECS Trans.* **2011**, *41*, 2283-2288.

[47] M. T. M. Koper, *Nanoscale* **2011**, *3*, 2054-2073.

[48] T. S. Ahmadi, Z. L. Wang, T. C. Green, A. Henglein, M. A. El-Sayed, *Science* **1996**, *272*, 1924-1925.

[49] S. Cherevko, G. P. Keeley, S. Geiger, A. R. Zeradjanin, N. Hodnik, N. Kulyk, K. J. J. Mayrhofer, *ChemElectroChem* **2015**, *2*, 1471-1478.

[50] A. A. Topalov, S. Cherevko, A. R. Zeradjanin, J. C. Meier, I. Katsounaros, K. J. J. Mayrhofer, *Chem. Sci.* **2014**, *5*, 631-638.

[51] G. A. Attard, A. Brew, K. Hunter, J. Sharman, E. Wright, *Phys. Chem. Chem. Phys.* **2014**, *16*, 13689-13698.

[52] D. Strmcnik, D. Li, P. P. Lopes, D. Tripkovic, K. Kodama, V. R. Stamenkovic, N. M. Markovic, *Top. Catal.* **2015**, *58*, 1174-1180.

[53] S. Geiger, S. Cherevko, K. J. J. Mayrhofer, *Electrochim. Acta* **2015**, *179*, 24-31.

[54] I. Katsounaros, W. B. Schneider, J. C. Meier, U. Benedikt, P. U. Biedermann, A. Cuesta, A. A. Auer, K. J. J. Mayrhofer, *Phys. Chem. Chem. Phys.* **2013**, *15*, 8058-8068.

[55] N. M. Marković, H. A. Gasteiger, B. N. Grgur, P. N. Ross, *J. Electroanal. Chem.* **1999**, *467*, 157-163.

[56] T. J. Schmidt, U. A. Paulus, H. A. Gasteiger, R. J. Behm, *J. Electroanal. Chem.* **2001**, *508*, 41-47.

[57] D. Strmcnik, M. Escudero-Escribano, K. Kodama, R. StamenkovicVojislav, A. Cuesta, N. M. Marković, *Nat. Chem.* **2010**, *2*, 880-885.

[58] A. Morozan, B. Jousselme, S. Palacin, *Energy Environ. Sci.* **2011**, *4*, 1238-1254.

[59] J. Tian, A. Morozan, M. T. Sougrati, M. Lefèvre, R. Chenitz, J.-P. Dodelet, D. Jones, F. Jaouen, *Angew. Chem.* **2013**, *125*, 7005-7008.

[60] J. K. Dombrovskis, A. E. C. Palmqvist, *Fuel Cells* **2016**, *16*, 4-22.

[61] M. S. Çögenli, S. Mukerjee, A. B. Yurtcan, *Fuel Cells* **2015**, *15*, 288-297.

[62] N. Ramaswamy, U. Tylus, Q. Jia, S. Mukerjee, *J. Am. Chem. Soc.* **2013**, *135*, 15443-15449.

[63] Z. Chen, D. Higgins, A. Yu, L. Zhang, J. Zhang, *Energy Environ. Sci.* **2011**, *4*, 3167-3192.

[64] J. Greeley, I. E. L. Stephens, A. S. Bondarenko, T. P. Johansson, H. A. Hansen, T. F. Jaramillo, J. Rossmeisl, I. Chorkendorff, J. K. Nørskov, *Nat. Chem.* **2009**, *1*, 552-556.

[65] I. E. L. Stephens, A. S. Bondarenko, F. J. Perez-Alonso, F. Calle-Vallejo, L. Bech, T. P. Johansson, A. K. Jepsen, R. Frydendal, B. P. Knudsen, J. Rossmeisl, I. Chorkendorff, *J. Am. Chem. Soc.* **2011**, *133*, 5485-5491.

[66] I. E. L. Stephens, A. S. Bondarenko, L. Bech, I. Chorkendorff, *ChemCatChem* **2012**, *4*, 341-349.

[67] C. Wang, N. M. Markovic, V. R. Stamenkovic, *ACS Catal.* **2012**, *2*, 891-898.

[68] V. Beermann, M. Gocyla, E. Willinger, S. Rudi, M. Heggen, R. E. Dunin-Borkowski, M.-G. Willinger, P. Strasser, *Nano Lett.* **2016**, *16*, 1719-1725.

[69] L. Gan, M. Heggen, S. Rudi, P. Strasser, *Nano Lett.* **2012**, *12*, 5423-5430.

[70] F. Hasché, M. Oezaslan, P. Strasser, *J. Electrochem. Soc.* **2011**, *159*, B24-B33.

[71] R. Srivastava, P. Mani, P. Strasser, *J. Power Sources* **2009**, *190*, 40-47.

[72] P. Strasser, S. Koh, J. Greeley, *Phys. Chem. Chem. Phys.* **2008**, *10*, 3670-3683.

[73] S. Koh, P. Strasser, *J. Am. Chem. Soc.* **2007**, *129*, 12624-12625.

[74] J. F. Drillet, A. Ee, J. Friedemann, R. Kötz, B. Schnyder, V. M. Schmidt, *Electrochim. Acta* **2002**, *47*, 1983-1988.

[75] V. Stamenković, T. J. Schmidt, P. N. Ross, N. M. Marković, *J. Electroanal. Chem.* **2003**, *554–555*, 191-199.

[76] H. Wu, D. Wexler, G. Wang, *J. Alloys Compd.* **2009**, *488*, 195-198.

[77] V. A. Bogdanovskaya, M. R. Tarasevich, L. N. Kuznetsova, G. V. Zhutaeva, O. V. Lozovaya, *Russ. J. Electrochem.* **2010**, *46*, 925-933.

[78] M. K. Carpenter, T. E. Moylan, R. S. Kukreja, M. H. Atwan, M. M. Tessema, *J. Am. Chem. Soc.* **2012**, *134*, 8535-8542.

[79] J. Wu, H. Yang, *ChemCatChem* **2012**, *4*, 1572-1577.

[80] M. C. S. Escaño, H. Kasai, *J. Power Sources* **2014**, *247*, 562-571.

[81] M. Oezaslan, F. Hasché, P. Strasser, *J. Electrochem. Soc.* **2012**, *159*, B444-B454.

[82] M. Oezaslan, P. Strasser, *J. Power Sources* **2011**, *196*, 5240-5249.

[83] N. Becknell, Y. Kang, C. Chen, J. Resasco, N. Kornienko, J. Guo, N. M. Markovic, G. A. Somorjai, V. R. Stamenkovic, P. Yang, *J. Am. Chem. Soc.* **2015**, *137*, 15817-15824.

[84] J. R. Greer, *Science* **2014**, *343*, 1319-1320.

[85] C. Chen, Y. Kang, Z. Huo, Z. Zhu, W. Huang, H. L. Xin, J. D. Snyder, D. Li, J. A. Herron, M. Mavrikakis, M. Chi, K. L. More, Y. Li, N. M. Markovic, G. A. Somorjai, P. Yang, V. R. Stamenkovic, *Science* **2014**, *343*, 1339-1343.

[86] A. F. Pedersen, E. T. Ulrikkeholm, M. Escudero-Escribano, T. P. Johansson, P. Malacrida, C. M. Pedersen, M. H. Hansen, K. D. Jensen, J. Rossmeisl, D. Friebel, A. Nilsson, I. Chorkendorff, I. E. L. Stephens, *Nano Energy*, http://dx.doi.org/10.1016/j.nanoen.2016.05.026.

[87] E. T. Ulrikkeholm, A. F. Pedersen, U. G. Vej-Hansen, M. Escudero-Escribano, I. E. L. Stephens, D. Friebel, A. Mehta, J. Schiøtz, R. K. Feidenhansl', A. Nilsson, I. Chorkendorff, *Surf. Sci.* **2016**, *652*, 114-122.

[88] M. Escudero-Escribano, A. Verdaguer-Casadevall, P. Malacrida, U. Grønbjerg, B. P. Knudsen, A. K. Jepsen, J. Rossmeisl, I. E. L. Stephens, I. Chorkendorff, *J. Am. Chem. Soc.* **2012**, *134*, 16476-16479.

[89] P. Hernandez-Fernandez, F. Masini, D. N. McCarthy, C. E. Strebel, D. Friebel, D. Deiana, P. Malacrida, A. Nierhoff, A. Bodin, A. M. Wise, J. H. Nielsen, T. W. Hansen, A. Nilsson, I. E. L. Stephens, I. Chorkendorff, *Nat. Chem.* **2014**, *6*, 732–738.

[90] T. P. Johansson, E. T. Ulrikkeholm, P. Hernandez-Fernandez, M. Escudero-Escribano, P. Malacrida, I. E. L. Stephens, I. Chorkendorff, *Phys. Chem. Chem. Phys.* **2014**, *16*, 13718-13725.

[91] T. P. Johansson, E. T. Ulrikkeholm, P. Hernandez-Fernandez, P. Malacrida, H. A. Hansen, A. S. Bandarenka, J. K. Nørskov, J. Rossmeisl, I. E. L. Stephens, I. Chorkendorff, *Top. Catal.* **2014**, *57*, 245-254.

[92] P. Malacrida, M. Escudero-Escribano, A. Verdaguer-Casadevall, I. E. L. Stephens, I. Chorkendorff, *J. Mater. Chem. A* **2014**, *2*, 4234-4243.

[93] A. Velázquez-Palenzuela, F. Masini, A. F. Pedersen, M. Escudero-Escribano, D. Deiana, P. Malacrida, T. W. Hansen, D. Friebel, A. Nilsson, I. E. L. Stephens, I. Chorkendorff, *J. Catal.* **2015**, *328*, 297-307.

[94] M. Escudero-Escribano, P. Malacrida, M. H. Hansen, U. G. Vej-Hansen, A. Velázquez-Palenzuela, V. Tripkovic, J. Schiøtz, J. Rossmeisl, I. E. L. Stephens, I. Chorkendorff, *Science* **2016**, *352*, 73-76.

[95] K. A. Kuttiyiel, K. Sasaki, Y. Choi, D. Su, P. Liu, R. R. Adzic, *Energy Environ. Sci.* **2012**, *5*, 5297-5304.

[96] J. Hu, L. Wu, K. A. Kuttiyiel, K. R. Goodman, C. Zhang, Y. Zhu, M. B. Vukmirovic, M. G. White, K. Sasaki, R. R. Adzic, *J. Am. Chem. Soc.* **2016**, *138*, 9294-9300.

[97] C. Hsu, C. Huang, Y. Hao, F. Liu, *Phys. Chem. Chem. Phys.* **2012**, *14*, 14696-14701.

[98] M. Neergat, R. Rahul, *J. Electrochem. Soc.* **2012**, *159*, F234-F241.

[99] J. Luo, L. Wang, D. Mott, P. N. Njoki, Y. Lin, T. He, Z. Xu, B. N. Wanjana, I. I. S. Lim, C.-J. Zhong, *Adv. Mater.* **2008**, *20*, 4342-4347.

[100] Y. Chen, F. Yang, Y. Dai, W. Wang, S. Chen, *J. Phys. Chem. C* **2008**, *112*, 1645-1649.

[101] C. Koenigsmann, A. C. Santulli, K. Gong, M. B. Vukmirovic, W.-p. Zhou, E. Sutter, S. S. Wong, R. R. Adzic, *J. Am. Chem. Soc.* **2011**, *133*, 9783-9795.

[102] D. Wang, H. L. Xin, R. Hovden, H. Wang, Y. Yu, D. A. Muller, F. J. DiSalvo, H. D. Abruña, *Nat. Mater.* **2013**, *12*, 81-87.

[103] M. K. Debe, *J. Electrochem. Soc.* **2013**, *160*, F522-F534.

[104] M. K. Debe, *Nature* **2012**, *486*, 43-51.

[105] D. van der Vliet, C. Wang, M. Debe, R. Atanasoski, N. M. Markovic, V. R. Stamenkovic, *Electrochim. Acta* **2011**, *56*, 8695-8699.

[106] J. Ma, A. Habrioux, N. Alonso-Vante, *ChemElectroChem* **2014**, *1*, 37-46.

[107] Y. Luo, N. Alonso-Vante, *Electrochim. Acta* **2015**, *179*, 108-118.

[108] P. Trogadas, T. F. Fuller, P. Strasser, *Carbon* **2014**, *75*, 5-42.

[109] S. Sharma, B. G. Pollet, *J. Power Sources* **2012**, *208*, 96-119.

[110] L. Perini, C. Durante, M. Favaro, V. Perazzolo, S. Agnoli, O. Schneider, G. Granozzi, A. Gennaro, *ACS Appl. Mater. Interfaces* **2015**, *7*, 1170-1179.

[111] S. Zhang, S. Chen, *J. Power Sources* **2013**, *240*, 60-65.

[112] S. Gao, H. Fan, X. Wei, L. Li, Y. Bando, D. Golberg, *Part. Part. Syst. Charact.* **2013**, *30*, 864-872.

[113] T. Holme, Y. Zhou, R. Pasquarelli, R. O'Hayre, *Phys. Chem. Chem. Phys.* **2010**, *12*, 9461-9468.

[114] Y. Zhou, R. Pasquarelli, T. Holme, J. Berry, D. Ginley, R. O'Hayre, *J. Mater. Chem.* **2009**, *19*, 7830-7838.

[115] L. Timperman, A. S. Gago, N. Alonso-Vante, *J. Power Sources* **2011**, *196*, 4290-4297.

[116] I. Savych, J. Bernard d'Arbigny, S. Subianto, S. Cavaliere, D. J. Jones, J. Roziere, *J. Power Sources* **2014**, *257*, 147-155.

[117] Y.-J. Wang, D. P. Wilkinson, J. Zhang, *Chem. Rev.* **2011**, *111*, 7625-7651.

[118] S. Maass, F. Finsterwalder, G. Frank, R. Hartmann, C. Merten, *J. Power Sources* **2008**, *176*, 444-451.

[119] R. Borup, J. Meyers, B. Pivovar, Y. S. Kim, R. Mukundan, N. Garland, D. Myers, M. Wilson, F. Garzon, D. Wood, P. Zelenay, K. More, K. Stroh, T. Zawodzinski, J. Boncella, J. E. McGrath, M. Inaba, K. Miyatake, M. Hori, K. Ota, Z. Ogumi, S. Miyata, A. Nishikata, Z. Siroma, Y. Uchimoto, K. Yasuda, K. Kimijima, N. Iwashita, *Chem. Rev.* **2007**, *107*, 3904-3951.

[120] Y.-J. Wang, D. P. Wilkinson, V. Neburchilov, C. Song, A. Guest, J. Zhang, *J. Mater. Chem. A* **2014**, *2*, 12681-12685.

[121] V. T. Thanh Ho, K. C. Pillai, H.-L. Chou, C.-J. Pan, J. Rick, W.-N. Su, B.-J. Hwang, J.-F. Lee, H.-S. Sheu, W.-T. Chuang, *Energy Environ. Sci.* **2011**, *4*, 4194-4200.

[122] Y. Luo, A. Habrioux, L. Calvillo, G. Granozzi, N. Alonso-Vante, *ChemPhysChem* **2014**, *15*, 2136–2144.

[123] Y. Luo, A. Habrioux, L. Calvillo, G. Granozzi, N. Alonso-Vante, *ChemCatChem* **2015**, *7*, 1573–1582.

[124] D.-e. Jiang, S. H. Overbury, S. Dai, *J. Phys. Chem. C* **2012**, *116*, 21880-21885.

[125] N. R. de Tacconi, C. R. Chenthamarakshan, K. Rajeshwar, W.-Y. Lin, T. F. Carlson, L. Nikiel, W. A. Wampler, S. Sambandam, V. Ramani, *J. Electrochem. Soc.* **2008**, *155*, B1102-B1109.

[126] N. R. de Tacconi, K. Rajeshwar, W. Chanmanee, V. Valluri, W. A. Wampler, W.-Y. Lin, L. Nikiel, *J. Electrochem. Soc.* **2010**, *157*, B147-B153.

[127] J. Shim, C.-R. Lee, H.-K. Lee, J.-S. Lee, E. J. Cairns, *J. Power Sources* **2001**, *102*, 172-177.

[128] K. Gong, F. Du, Z. Xia, M. Durstock, L. Dai, *Science* **2009**, *323*, 760-764.

[129] P. L. Kuo, C. H. Hsu, H. M. Wu, W. S. Hsu, D. Kuo, *Fuel Cells* **2012**, *12*, 649-655.

[130] L. Perini, C. Durante, M. Favaro, S. Agnoli, G. Granozzi, A. Gennaro, *Appl. Catal., B* **2014**, *144*, 300-307.

[131] Y. Zhou, T. Holme, J. Berry, T. R. Ohno, D. Ginley, R. O'Hayre, *J. Phys. Chem. C* **2010**, *114*, 506-515.

[132] http://www.fch.europa.eu/page/multi-annual-work-plan

[133] J. R. Kitchin, J. K. Nørskov, M. A. Barteau, J. G. Chen, *J. Chem. Phys.* **2004**, *120*, 10240-10246.

[134] M. Lischka, C. Mosch, A. Groß, *Electrochim. Acta* **2007**, *52*, 2219-2228.

[135] A. Rabis, P. Rodriguez, T. J. Schmidt, *ACS Catal.* **2012**, *2*, 864-890.

[136] N. M. Markovic, H. A. Gasteiger, P. N. Ross, *J. Phys. Chem.* **1995**, *99*, 3411-3415.

[137] J. Wu, H. Yang, *Acc. Chem. Res.* **2013**, *46*, 1848-1857.

[138] J. Wu, A. Gross, H. Yang, *Nano Lett.* **2011**, *11*, 798-802.

[139] N. Alonso-Vante, *Fuel Cells* **2006**, *6*, 182-189.

[140] N. S. Porter, H. Wu, Z. Quan, J. Fang, *Acc. Chem. Res.* **2013**, *46*, 1867-1877.

[141] E. Antolini, *ChemElectroChem* **2013**, *1*, 318-328.

[142] S. Guo, S. Zhang, S. Sun, *Angew. Chem.* **2013**, *125*, 8686-8705.

[143] L. Gan, C. Cui, S. Rudi, P. Strasser, *Top. Catal.* **2014**, *57*, 236-244.

[144] M. Oezaslan, F. Hasché, P. Strasser, *J. Phys. Chem. Lett.* **2013**, *4*, 3273-3291.

[145] M. Shao, Q. Chang, J.-P. Dodelet, R. Chenitz, *Chem. Rev.* **2016**, *116*, 3594-3657.

[146] A. M. Gomez-Marin, R. Rizo, J. M. Feliu, *Beilstein J. Nanotechnol.* **2013**, *4*, 956-967, 912 pp.

[147] A. M. Gomez-Marin, R. Rizo, J. M. Feliu, *Catal. Sci. Technol.* **2014**, *4*, 1685-1698.

[148] A. M. Gómez-Marín, J. M. Feliu, *ChemSusChem* **2013**, *6*, 1091-1100.

[149] C.-H. Chen, K. E. Meadows, A. Cuharuc, S. C. S. Lai, P. R. Unwin, *Phys. Chem. Chem. Phys.* **2014**, *16*, 18545-18552.

[150] F. J. Perez-Alonso, D. N. McCarthy, A. Nierhoff, P. Hernandez-Fernandez, C. Strebel, I. E. L. Stephens, J. H. Nielsen, I. Chorkendorff, *Angew. Chem., Int. Ed.* **2012**, *51*, 4641-4643.

[151] U. A. Paulus, A. Wokaun, G. G. Scherer, T. J. Schmidt, V. Stamenkovic, N. M. Markovic, P. N. Ross, *Electrochim. Acta* **2002**, *47*, 3787-3798.

[152] C. M. Zalitis, D. Kramer, A. R. Kucernak, *Phys. Chem. Chem. Phys.* **2013**, *15*, 4329-4340.

[153] K. Kunimatsu, H. Hanawa, H. Uchida, M. Watanabe, *J. Electroanal. Chem.* **2009**, *632*, 109-119.

[154] J. Omura, H. Yano, D. A. Tryk, M. Watanabe, H. Uchida, *Langmuir* **2014**, *30*, 432-439.

[155] J. Omura, H. Yano, M. Watanabe, H. Uchida, *Langmuir* **2011**, *27*, 6464-6470.

[156] A. Berná, J. M. Feliu, L. Gancs, S. Mukerjee, *Electrochem. Commun.* **2008**, *10*, 1695-1698.

[157] A. S. Bondarenko, I. E. L. Stephens, H. A. Hansen, F. J. Pérez-Alonso, V. Tripkovic, T. P. Johansson, J. Rossmeisl, J. K. Nørskov, I. Chorkendorff, *Langmuir* **2011**, *27*, 2058–2066.

[158] A. A. Topalov, I. Katsounaros, M. Auinger, S. Cherevko, J. C. Meier, S. O. Klemm, K. J. J. Mayrhofer, *Angew. Chem., Int. Ed.* **2012**, *51*, 12613-12615.

[159] Y. Takasu, N. Ohashi, X. G. Zhang, Y. Murakami, H. Minagawa, S. Sato, K. Yahikozawa, *Electrochim. Acta* **1996**, *41*, 2595-2600.

[160] U. Benedikt, W. B. Schneider, A. A. Auer, *Phys. Chem. Chem. Phys.* **2013**, *15*, 2712-2724.

[161] P. C. Jennings, H. A. Aleksandrov, K. M. Neyman, R. L. Johnston, *Nanoscale* **2014**, *6*, 1153-1165.

[162] L. Zhang, L. T. Roling, X. Wang, M. Vara, M. Chi, J. Liu, S.-I. Choi, J. Park, J. A. Herron, Z. Xie, M. Mavrikakis, Y. Xia, *Science* **2015**, *349*, 412-416.

[163] W. Ju, R. Valiollahi, R. Ojani, O. Schneider, U. Stimming, *Electrocatalysis* **2016**, *7*, 149-158.

[164] W. Ju, T. Brülle, M. Favaro, L. Perini, C. Durante, O. Schneider, U. Stimming, *ChemElectroChem* **2015**, *2*, 547 – 558.

[165] Y. Luo, J. M. Mora-Hernández, L. A. Estudillo-Wong, E. M. Arce-Estrada, N. Alonso-Vante, *Electrochim. Acta* **2015**, *173*, 771-778.

[166] V. Stamenković, T. J. Schmidt, P. N. Ross, N. M. Marković, *J. Phys. Chem. B* **2002**, *106*, 11970-11979.

[167] V. R. Stamenkovic, B. Fowler, B. S. Mun, G. Wang, P. N. Ross, C. A. Lucas, N. M. Marković, *Science* **2007**, *315*, 493-497.

[168] J. Zhang, H. Yang, J. Fang, S. Zou, *Nano Lett.* **2010**, *10*, 638-644.

[169] P. Mani, R. Srivastava, P. Strasser, *J. Power Sources* **2011**, *196*, 666-673.

[170] W. Roh, J. Cho, H. Kim, *Catal. Lett.* **1996**, *37*, 41-46.

[171] B. C. Beard, P. N. Ross, *J. Electrochem. Soc.* **1990**, *137*, 3368-3374.

[172] U. A. Paulus, A. Wokaun, G. G. Scherer, T. J. Schmidt, V. Stamenkovic, V. Radmilovic, N. M. Markovic, P. N. Ross, *J. Phys. Chem. B* **2002**, *106*, 4181-4191.

[173] L. Bu, S. Guo, X. Zhang, X. Shen, D. Su, G. Lu, X. Zhu, J. Yao, J. Guo, X. Huang, *Nat. Commun.* **2016**, *7*.

[174] X. Xu, X. Zhang, H. Sun, Y. Yang, X. Dai, J. Gao, X. Li, P. Zhang, H.-H. Wang, N.-F. Yu, S.-G. Sun, *Angew. Chem., Int. Ed.* **2014**, *53*, 12522-12527.

[175] R. Sakamoto, K. Omichi, T. Furuta, M. Ichikawa, *J. Power Sources* **2014**, *269*, 117-123.

[176] X. Huang, Z. Zhao, L. Cao, Y. Chen, E. Zhu, Z. Lin, M. Li, A. Yan, A. Zettl, Y. M. Wang, X. Duan, T. Mueller, Y. Huang, *Science* **2015**, *348*, 1230-1234.

[177] Y. Li, F. Quan, L. Chen, W. Zhang, H. Yu, C. Chen, *RSC Adv.* **2014**, *4*, 1895-1899.

[178] S. Brimaud, A. K. Engstfeld, O. B. Alves, R. J. Behm, *J. Electroanal. Chem.* **2014**, *716*, 71-79.

[179] A. S. Bondarenko, I. E. L. Stephens, L. Bech, I. Chorkendorff, *Electrochim. Acta* **2012**, *82*, 517-523.

[180] Y. Yamada, K. Miyamoto, T. Hayashi, Y. Iijima, N. Todoroki, T. Wadayama, *Surf. Sci.* **2013**, *607*, 54-60.

[181] D. Cheng, X. Qiu, H. Yu, *Phys. Chem. Chem. Phys.* **2014**, *16*, 20377-20381.

[182] M. Chi, C. Wang, Y. Lei, G. Wang, D. Li, K. L. More, A. Lupini, L. F. Allard, N. M. Markovic, V. R. Stamenkovic, *Nat. Commun.* **2015**, *6*.

[183] T. Rurigaki, A. Hitotsuyanagi, M. Nakamura, N. Sakai, N. Hoshi, *J. Electroanal. Chem.* **2014**, *716*, 58-62.

[184] Y. Zhang, T. Han, J. Fang, P. Xu, X. Li, J. Xu, C.-C. Liu, *J. Mater. Chem. A* **2014**, *2*, 11400-11407.

[185] S. Zhang, Y. Hao, D. Su, V. V. T. Doan-Nguyen, Y. Wu, J. Li, S. Sun, C. B. Murray, *J. Am. Chem. Soc.* **2014**, *136*, 15921-15924.

[186] C. Cui, L. Gan, M. Heggen, S. Rudi, P. Strasser, *Nat. Mater.* **2013**, *12*, 765-771.

[187] A. Oh, H. Baik, D. S. Choi, J. Y. Cheon, B. Kim, H. Kim, S. J. Kwon, S. H. Joo, Y. Jung, K. Lee, *ACS Nano* **2015**, *9*, 2856-2867.

[188] L. Gan, M. Heggen, C. Cui, P. Strasser, *ACS Catal.* **2016**, *6*, 692-695.

[189] H. Kleykamp, *J. Nucl. Mater.* **1993**, *201*, 193-217.

[190] L. Hellwig, Ph.D. thesis, Kernforschungszentrum Karlsruhe (Karlsruhe), **1978**.

[191] in *Landolt-Börnstein - Group IV Physical Chemistry 19A4, Vol. 19A4*, Springer Verlag, Berlin-Heidelberg, **2001**, p. 335.

[192] D. R. Lide, G. Baysinger, L. I. Berger, R. N. Goldberg, H. V. Kehiaian, K. Kuchitsu, G. Rosenblatt, D. L. Roth, D. Zwillinger, *CRC Handbook of Chemistry and Physics* **2003**, 3485.

[193] in *Landolt-Börnstein - Group IV Physical Chemistry 19A3, Vol. 19A3*, Springer Verlag, Berlin-Heidelberg, **2000**, p. 63.

[194] F. Masini, P. Hernandez-Fernandez, D. Deiana, C. E. Strebel, D. N. McCarthy, A. Bodin, P. Malacrida, I. Stephens, I. Chorkendorff, *Phys. Chem. Chem. Phys.* **2014**, *16*, 26506-26513.

[195] P. Malacrida, H. G. Sanchez Casalongue, F. Masini, S. Kaya, P. Hernandez-Fernandez, D. Deiana, H. Ogasawara, I. E. L. Stephens, A. Nilsson, I. Chorkendorff, *Phys. Chem. Chem. Phys.* **2015**, 10.1039/C5CP00283D, doi: 10.1039/C1035CP00283D.

[196] A. J. Steinbach, D. van der Vliet, A. E. Hester, J. Erlebacher, C. Duru, I. Davy, M. Kuznia, D. A. Cullen, *ECS Trans.* **2015**, *69*, 291-301.

[197] S. J. Yoo, S. J. Hwang, J.-G. Lee, S.-C. Lee, T.-H. Lim, Y.-E. Sung, A. Wieckowski, S.-K. Kim, *Energy Environ. Sci.* **2012**, *5*, 7521-7525.

[198] S. J. Yoo, K.-S. Lee, S. J. Hwang, Y.-H. Cho, S.-K. Kim, J. W. Yun, Y.-E. Sung, T.-H. Lim, *Int. J. Hydrogen Energy* **2012**, *37*, 9758-9765.

[199] S. J. Yoo, Y.-E. Sung, *Surf. Sci.* **2015**, *631*, 272-277.

[200] M. Favaro, G. A. Rizzi, S. Nappini, E. Magnano, F. Bondino, S. Agnoli, G. Granozzi, *Surf. Sci.* **2016**, *646*, 132-139.

[201] K. Richter, P. S. Campbell, T. Baecker, A. Schimitzek, D. Yaprak, A.-V. Mudring, *Phys. Status Solidi B* **2013**, *250*, 1152-1164.

[202] S. Suzuki, T. Suzuki, Y. Tomita, M. Hirano, K.-i. Okazaki, S. Kuwabata, T. Torimoto, *CrystEngComm* **2012**, *14*, 4922-4926.

[203] Y. Hatakeyama, K. Onishi, K. Nishikawa, *RSC Adv.* **2011**, *1*, 1815-1821.

[204] T. Tsuda, K. Yoshii, T. Torimoto, S. Kuwabata, *J. Power Sources* **2010**, *195*, 5980-5985.

[205] Y. N. Ertas, N. N. Jarenwattananon, L.-S. Bouchard, *Chem. Mater.* **2015**, *27*, 5371-5376.

[206] Y. Luo, L. Calvillo, C. Daiguebonne, M. K. Daletou, G. Granozzi, N. Alonso-Vante, *Appl. Catal., B* **2016**, *189*, 39-50.

[207] M. K. Jeon, P. J. McGinn, *J. Power Sources* **2011**, *196*, 1127-1131.

[208] K. G. Nishanth, P. Sridhar, S. Pitchumani, *Electrochem. Commun.* **2011**, *13*, 1465-1468.

[209] J. A. Nelson, M. J. Wagner, *Chem. Mater.* **2002**, *14*, 915-917.

[210] O. Zivkovic, K. E. Mooney, M. J. Wagner, *Chem. Mater.* **2007**, *19*, 3419-3424.

[211] C. Yan, M. J. Wagner, *Nano Lett.* **2013**, *13*, 2611-2614.

[212] R. Brandiele, C. Durante, E. Gradzka, G. A. Rizzi, J. Zheng, D. Badocco, P. Centomo, P. Pastore, G. Granozzi, A. Gennaro, *J. Mater. Chem. A* **2016**, *4*, 12232-12240.

[213] X. Liu, E. H. Yu, K. Scott, *Appl. Catal., B* **2015**, *162*, 593-601.

[214] J. Zhang, P. Evans, G. Zangari, *J. Magn. Magn. Mater.* **2004**, *283*, 89-94.

[215] I. A. Shkrob, T. W. Marin, M. P. Jensen, *Ind. Eng. Chem. Res.* **2014**, *53*, 3641-3653.

[216] A. I. Bhatt, I. May, V. A. Volkovich, D. Collison, M. Helliwell, I. B. Polovov, R. G. Lewin, *Inorg. Chem.* **2005**, *44*, 4934-4940.

[217] A. I. Bhatt, I. May, V. A. Volkovich, M. E. Hetherington, B. Lewin, R. C. Thied, N. Ertok, *J. Chem. Soc., Dalton Trans.* **2002**, 4532-4534.

[218] L.-H. Chou, W. E. Cleland, C. L. Hussey, *Inorg. Chem.* **2012**, *51*, 11450-11457.

[219] L. Martinot, L. Lopes, J. Marien, C. Jérôme, *J. Radioanal. Nucl. Chem.* **2002**, *253*, 407-412.

[220] L.-H. Chou, C. L. Hussey, *Inorg. Chem.* **2014**, *53*, 5750-5758.

[221] H. Kondo, M. Matsumiya, K. Tsunashima, S. Kodama, *Electrochim. Acta* **2012**, *66*, 313-319.

[222] H. Kondo, M. Matsumiya, K. Tsunashima, S. Kodama, *ECS Trans.* **2013**, *50*, 529-538.

[223] W. Simka, D. Puszczyk, G. Nawrat, *Electrochim. Acta* **2009**, *54*, 5307-5319.

[224] P. Liu, Q. Yang, Y. Tong, Y. Yang, *Electrochim. Acta* **2000**, *45*, 2147-2152.

[225] G.-p. Zheng, Y. Zhan, P. Liu, *J. Alloys Compd.* **2003**, *358*, 65-70.

[226] M. Ruehrig, G. Schmid, G. Suppan, A. Kanitz, W. Kantlehner, G. Maas, M. Arkhipova, Siemens Ag (Siei-C) Siemens Ag (Siei-C), **2014**, p. 32.

[227] S. Legeai, S. Diliberto, N. Stein, C. Boulanger, J. Estager, N. Papaiconomou, M. Draye, *Electrochem. Commun.* **2008**, *10*, 1661-1664.

[228] M. Yamagata, Y. Katayama, T. Miura, *J. Electrochem. Soc.* **2006**, *153*, E5-E9.

[229] N. Tachikawa, Y. Katayama, T. Miura, *Electrochemistry* **2009**, *77*, 642-644.

[230] Y. Pan, C. L. Hussey, *Inorg. Chem.* **2013**, *52*, 3241-3252.

[231] Q. B. Zhang, C. Yang, Y. X. Hua, Y. Li, P. Dong, *Phys. Chem. Chem. Phys.* **2015**, *17*, 4701-4707.

[232] A. Ispas, M. Buschbeck, S. Pitula, A. Mudring, M. Uhlemann, A. Bund, F. Endres, *ECS Trans.* **2009**, *16*, 119-127.

[233] J. Lodermeyer, M. Multerer, M. Zistler, S. Jordan, H. J. Gores, W. Kipferl, E. Diaconu, M. Sperl, G. Bayreuther, *J. Electrochem. Soc.* **2006**, *153*, C242-C248.

[234] L. M. Glukhov, A. A. Greish, L. M. Kustov, *Russ. J. Phys. Chem. A* **2010**, *84*, 104-108.

[235] A. Kurachi, M. Matsumiya, K. Tsunashima, S. Kodama, *J. Appl. Electrochem.* **2012**, *42*, 961-968.

[236] M. Ishii, M. Matsumiya, S. Kawakami, *ECS Trans.* **2013**, *50*, 549-560.

[237] M. Matsumiya, M. Ishii, R. Kazama, S. Kawakami, *Electrochim. Acta* **2014**, *146*, 371-377.

[238] A.-V. Mudring, A. Babai, S. Arenz, R. Giernoth, *Angew. Chem., Int. Ed.* **2005**, *44*, 5485-5488.

[239] A. Babai, A.-V. Mudring, *Chem. Mater.* **2005**, *17*, 6230-6238.

[240] A. Babai, A.-V. Mudring, *Z. Anorg. Allg. Chem.* **2008**, *634*, 938-940.

[241] S. Tang, A. Babai, A.-V. Mudring, *Angew. Chem., Int. Ed.* **2008**, *47*, 7631-7634.

[242] A. Babai, S. Pitula, A.-V. Mudring, *Eur. J. Inorg. Chem.* **2010**, *2010*, 4933-4937.

[243] A. Babai, G. Kopiec, A. Lackmann, B. Mallick, S. Pitula, S. Tang, A.-V. Mudring, *J. Mol. Liq.* **2014**, *192*, 191-198.

[244] A. S. R. Chesman, M. Yang, B. Mallick, T. M. Ross, I. A. Gass, G. B. Deacon, S. R. Batten, A.-V. Mudring, *Chem. Commun.* **2012**, *48*, 124-126.

[245] A. S. R. Chesman, M. Yang, N. D. Spiccia, G. B. Deacon, S. R. Batten, A.-V. Mudring, *Chem. - Eur. J.* **2012**, *18*, 9580-9589.

[246] P. He, H. Liu, Z. Li, J. Li, *J. Electrochem. Soc.* **2005**, *152*, E146-E153.

[247] D. Zhang, W. C. Chang, T. Okajima, T. Ohsaka, *Langmuir* **2011**, *27*, 14662-14668.

[248] U. G. Vej-Hansen, J. Rossmeisl, I. E. L. Stephens, J. Schiotz, *Phys. Chem. Chem. Phys.* **2016**, *18*, 3302-3307.

[249] S. J. Hwang, S.-K. Kim, J.-G. Lee, S.-C. Lee, J. H. Jang, P. Kim, T.-H. Lim, Y.-E. Sung, S. J. Yoo, *J. Am. Chem. Soc.* **2012**, *134*, 19508-19511.

[250] V. Tripkovic, J. Zheng, G. A. Rizzi, C. Marega, C. Durante, J. Rossmeisl, G. Granozzi, *ACS Catal.* **2015**, *5*, 6032-6040.

[251] W. Ju, M. Favaro, C. Durante, L. Perini, S. Agnoli, O. Schneider, U. Stimming, G. Granozzi, *Electrochim. Acta* **2014**, *141*, 89-101.

[252] V. Perazzolo, C. Durante, R. Pilot, A. Paduano, J. Zheng, G. A. Rizzi, A. Martucci, G. Granozzi, A. Gennaro, *Carbon* **2015**, *95*, 949-963.

[253] V. Perazzolo, E. Grądzka, C. Durante, R. Pilot, N. Vicentini, G. A. Rizzi, G. Granozzi, A. Gennaro, *Electrochim. Acta* **2016**, *197*, 251-262.

[254] M. Favaro, S. Agnoli, M. Cattelan, A. Moretto, C. Durante, S. Leonardi, J. Kunze-Liebhäuser, O. Schneider, A. Gennaro, G. Granozzi, *Carbon* **2014**, *77*, 405-415.

[255] M. Favaro, L. Ferrighi, G. Fazio, L. Colazzo, C. Di Valentin, C. Durante, F. Sedona, A. Gennaro, S. Agnoli, G. Granozzi, *ACS Catal.* **2015**, *5*, 129-144.

[256] M. Favaro, F. Carraro, M. Cattelan, L. Colazzo, C. Durante, M. Sambi, A. Gennaro, S. Agnoli, G. Granozzi, *J. Mater. Chem. A* **2015**, *3*, 14334-14347.

[257] J. Ma, A. Habrioux, Y. Luo, G. Ramos Sanchez, L. Calvillo, G. Granozzi, P. B. Balbuena, N. Alonso-Vante, *J. Mater. Chem. A* **2015**, *3*, 11891-11904.

[258] S. Mokrane-Soualah, A. S. Gago, A. Habrioux, N. Alonso-Vante, *Appl. Catal., B* **2014**, *147*, 756-763.

[259] L. A. Estudillo-Wong, Y. Luo, J. A. Díaz-Real, N. Alonso-Vante, *Appl. Catal., B* **2016**, *187*, 291-300.

[260] T. J. Schmidt, H. A. Gasteiger, G. D. Stäb, P. M. Urban, D. M. Kolb, R. J. Behm, *J. Electrochem. Soc.* **1998**, *145*, 2354-2358.

[261] C. M. Pedersen, M. Escudero-Escribano, A. Velázquez-Palenzuela, L. H. Christensen, I. Chorkendorff, I. E. L. Stephens, *Electrochim. Acta* **2015**, *179*, 647–657.

[262] Y. Garsany, O. A. Baturina, K. E. Swider-Lyons, S. S. Kocha, *Anal. Chem.* **2010**, *82*, 6321-6328.

[263] Y. Garsany, I. L. Singer, K. E. Swider-Lyons, *J. Electroanal. Chem.* **2011**, *662*, 396-406.

[264] Y. Garsany, J. Ge, J. St-Pierre, R. Rocheleau, K. E. Swider-Lyons, *J. Electrochem. Soc.* **2014**, *161*, F628-F640.

[265] R. Frydendal, E. A. Paoli, B. P. Knudsen, B. Wickman, P. Malacrida, I. E. L. Stephens, I. Chorkendorff, *ChemElectroChem* **2014**, *1*, 2075-2081.

[266] B. Wickman, M. Fredriksson, L. Feng, N. Lindahl, J. Hagberg, C. Langhammer, *Phys. Chem. Chem. Phys.* **2015**, *17*, 18953-18960.

[267] E. M. Larsson, C. Langhammer, I. Zoric, B. Kasemo, *Science* **2009**, *326*, 1091-1094.

[268] C. Langhammer, E. M. Larsson, B. Kasemo, I. Zoric, *Nano. Lett.* **2010**, *10*, 3529-3538.

[269] K. Shinozaki, J. W. Zack, R. M. Richards, B. S. Pivovar, S. S. Kocha, *J. Electrochem. Soc.* **2015**, *162*, F1144-F1158.

[270] K. Shinozaki, J. W. Zack, S. Pylypenko, B. S. Pivovar, S. S. Kocha, *J. Electrochem. Soc.* **2015**, *162*, F1384-F1396.

Figure Captions

Figure 1. Free-energy diagrams of ORR (top) associative and (bottom) dissociative pathways. Reprinted with permission from Ref. [22]. Copyright 2014, American Chemical Society.

Figure 2. Cyclic voltammograms of Pt[n(111) x (111)] stepped single crystals, where n = 3, 5, 10 is the number of Pt atoms at (111) terraces, compared with the Pt(111) electrode. All data correspond to 0.1M $HClO_4$. v =50 mVs^{-1}. Reproduced from Ref. [20] with permission from the PCCP Owner Societies.

Figure 3. Coordination-activity plot. (A)Potentials for the two limiting steps on extended surfaces and NPs. Points B and C (in light blue) are given for two cavities on Pt(111).The potential-determining step on the left (low coordination – strong binding) and right (high coordination – weak binding) sides of the volcano are indicated.Theoretical overpotentials (hORR) are the vertical difference between the points and the equilibrium potential (red dashed line). Optimal catalysts have CN ≈ 8:3and *OH adsorption energies ~0.15 eV weaker than Pt(111) (area in gray). (B) Top view of a six-atom cavity on Pt(111) with CN=(6x10+3x12)/12 = 8.00. (C) Five-atom cavity on Pt(111) with CN = (4x10+2x11+3x12)/12 =8.17. Reproduced from Ref. [30]. Reprinted with permission from AAAS.

Figure 4. Energy diagram for the dissociation of H_2O_2 on the Pt(111) surface model with (a) no, (b) two and (c) three adsorbed chlorine atoms. The energies are given relative to H_2O_2 in the gas

phase (dashed line). The grey bar corresponds to H_2O_2 in solution. Reproduced from Ref. [54] - Published by the PCCP Owner Societies.

Figure 5. Stability measurement of one Pd/HOPG sample (prepared with a nucleation pulse of 10 ms and a growth pulse of 20 s) in three Ar-purged electrolytes with different pH values. Five potential cycles were applied to the sample each time in one electrolyte. The surface area is evaluated from the transferred charge of PdO reduction. Potential ranges were 0.3–1.45 V vs. SHE in 0.1M H_2SO_4 (pH 1), 0.182–1.332 Vvs. SHE in 0.1M Na_2SO_4+x mM H_2SO_4 (pH 3) and 0.102–1.252 V vs. saturated hydrogen electrode in 0.1M Na_2SO_4 (pH 4.35). Reproduced from Ref. [164] with permission from Wiley. Copyright 2015, John Wiley & Sons.

Figure 6. (a) Specific activity and (b) mass activity of Pt_xGd nanoparticles (blue). Data taken at 0.9 V from cyclic voltammetry recorded at 50 mV s^{-1}, 1600 rpm, and 23 ± 1 °C in O_2-saturated 0.1M $HClO_4$. For comparison, the previously published mass and specific activities of mass-selected Pt_xY (red) and pure Pt nanoparticles (black) are also plotted. Additionally, the specific activities obtained under the same conditions of sputter-cleaned polycrystalline Pt_5Gd and Pt_3Y extended surface electrodes, as well as sputter-cleaned polycrystalline Pt, are presented. Each data point corresponds to the mean value from at least two independent electrochemical tests. The horizontal error bars show the standard deviation in the particle size distribution (PSD) whereas the vertical error bars show the standard deviation in electrochemical measurements. The lines serve as a guide for the eye. Reprinted from Ref. [93] with permission from Elsevier.

Figure 7. The initial mass activity of Pt_xGd nanoparticles (blue), and after 1000 cycles (green) and 10,000 cycles (violet) of stability test under ORR conditions. The initial performance of the most active Pt_xY catalyst (red) and after 9000 cycles of stability test (orange) is also displayed. For a suitable comparison, the maximum activity reported for mass-selected Pt NPs is also plotted (black). Data taken at 0.9 V from cyclic voltammetry recorded at 50 mV s^{-1}, 1600 rpm, and 23 ± 1 °C in O_2-saturated 0.1M $HClO_4$. Stability test carried out by potential cycling between 0.6 and 1.0 V at 100 mV s^{-1}, 0 rpm, and 23 ± 1 °C in O_2-saturated 0.1M $HClO_4$ solution. Reprinted from Ref. [93] with permission from Elsevier.

Figure 8. Pd (a) and Y (b) 3d spectra (area normalized) acquired in normal emission mode for 1.0 MLE of Pd or stacked Y/Pd ultrathin films (after annealing at 750 °C) on HOPG and N-HOPG (using a photon energy of 595 eV). The reported difference spectra in (a) have been obtained by the subtraction of dark and bright blue curves from the black and gray curve, respectively. Reproduced from Ref. [200] with permission from Elsevier.

Figure 9. TEM images and size distributions of NPs obtained by sputter deposition on TMPA-TFSA: (a) Au NPs (fraction of Au area on sputter target $f_{Au} = 1.0$), (b) AuPt NPs ($f_{Au} = 0.33$) and (c) Pt NPs ($f_{Au} = 0$). Reproduced from Ref. [202] with permission of The Royal Society of Chemistry.

Figure 10. TEM image of Gd@Au nanocrystals. Reprinted with permission from Ref. [211]. Copyright (2013) American Chemical Society.

Figure 11. Y 3d peak deconvolution for a Pt_xY sample prepared for 3 h at 650 °C. Reproduced in part from Ref. [212] with permission of The Royal Society of Chemistry.

Figure 12. SEM images of lanthanum electrodeposited on Pt foil in 0.08M $LaCl_3$/BMI-DCA IL at the applied potentials of -1.1 V for 2 h at 333 K. Reproduced in part from Ref. [231] with permission of the PCCP Owner Societies.

Figure 13. The microscopic morphology of the neodymium deposited sample on a Cu substrate by potentiostatic condition at −3.1 V in 0.5 mol dm^{-3} Nd(III)/$[P_{2225}]$[TFSA] at 150°C. Reproduced from Ref. [221] with permission from Elsevier.

Figure 14. (a) RRDE polarization curves at 1600 rpm and 50 mV s^{-1} for the ORR on Pt_5Gd (red curve), Pt (black curve), and Pt_3Y (dotted gray curve) polycrystalline electrodes in O_2-saturated 0.1M $HClO_4$. (b) Tafel plots showing the kinetic current density (j_k) of Pt_5Gd, Pt, and Pt_3Y as a function of the potential (U), based on data from (a). Reprinted with permission from Ref. [88]. Copyright (2012) American Chemical Society.

Figure 15. Tafel plots showing the kinetic current density (j_k) normalized per geometric surface area of Pt_5Ce, Pt_5La, Pt_3La, Pt and Pt_5Gd_{33} as a function of the potential (U). Reproduced from Ref. [92] with permission of The Royal Society of Chemistry.

Figure 16. Experimental volcano- type relationships between activity, H adsorption, and Pt-Pt distance. (A) Kinetic current density at 0.9 V on polycrystalline Pt_5M electrocatalysts versus the lattice parameter a of bulk Pt_5M (lower axis) and bulk $d_{Pt\text{-}Pt}$ (upper axis), respectively. The figure shows the kinetic current density, j_k, of the alloys after the initial ORR activity (dark gray squares) and after 10,000 cycles of the stability test (colored circles). The dotted and dashed lines represent the experimental trends resulting after initial ORR activity and after stability, respectively. The activity of Pt_5Ca after 10,000 cycles has been normalized to account for the increase of area after the stability test. (B) Relation between the potential necessary to adsorb 1/8, 1/6, 1/4, and 1/3 monolayers (ML) of H (U_H) from the cyclic voltammograms (CVs) in the H adsorption region in N_2-saturated 0.1M $HClO_4$ on Pt_5M and $d_{Pt\text{-}Pt}$. From Ref. [94]. Reprinted with permission from AAAS.

Figure 17. Estimated activities of strained Pd(111) surfaces (red circles) as a function of the OH binding energy. Labels designate different strains, where "+" is expansive and "–" compressive strain. Reprinted in part with permission from Ref. [250]. Copyright (2015) American Chemical Society.

Figure 18. Polarization curves at 2400 rpm, 20 mV s^{-1} for the ORR on polycrystalline Pd and Pd_5Ce electrodes in O_2-saturated 0.1M $HClO_4$ solution. Reprinted in part with permission from Ref. [250]. Copyright (2015) American Chemical Society.

Figure 19. Mass activity and specific activity before and after an accelerated stress test in 0.1 $HClO_4$, 1600 rpm for a Pt/C benchmark catalyst and a Pt_xY alloy sample. Reproduced in part from Ref. [212] with permission of The Royal Society of Chemistry.

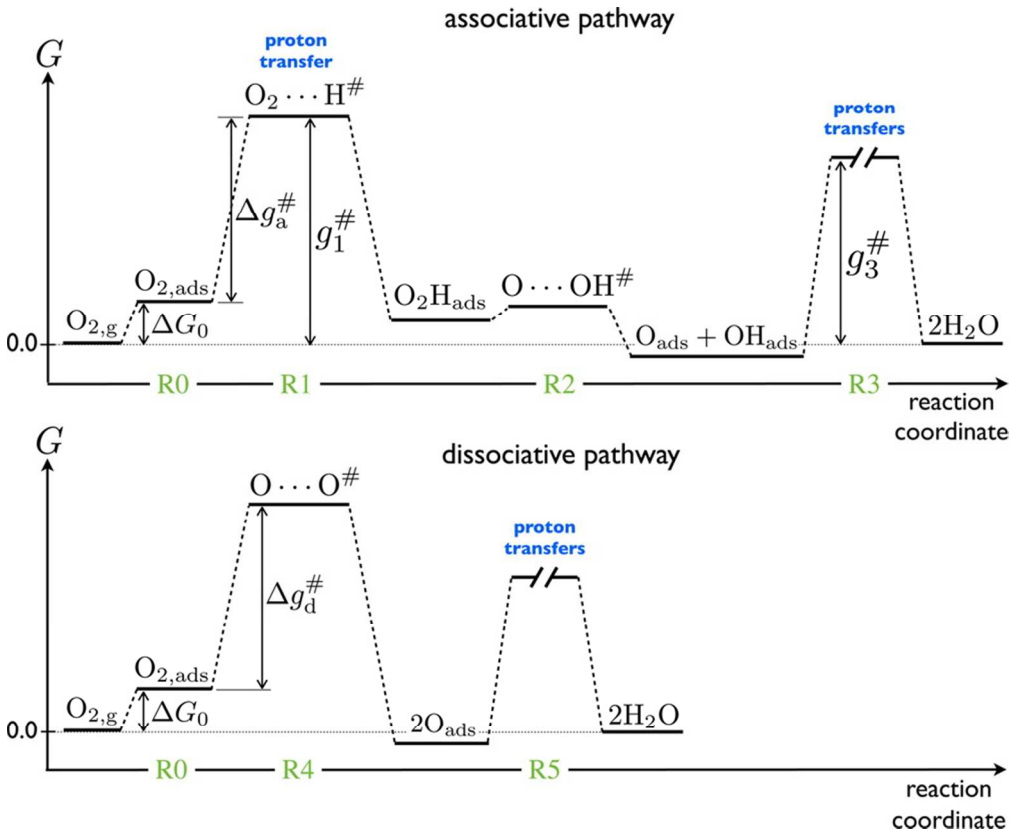

Figure 1
84x69mm (300 x 300 DPI)

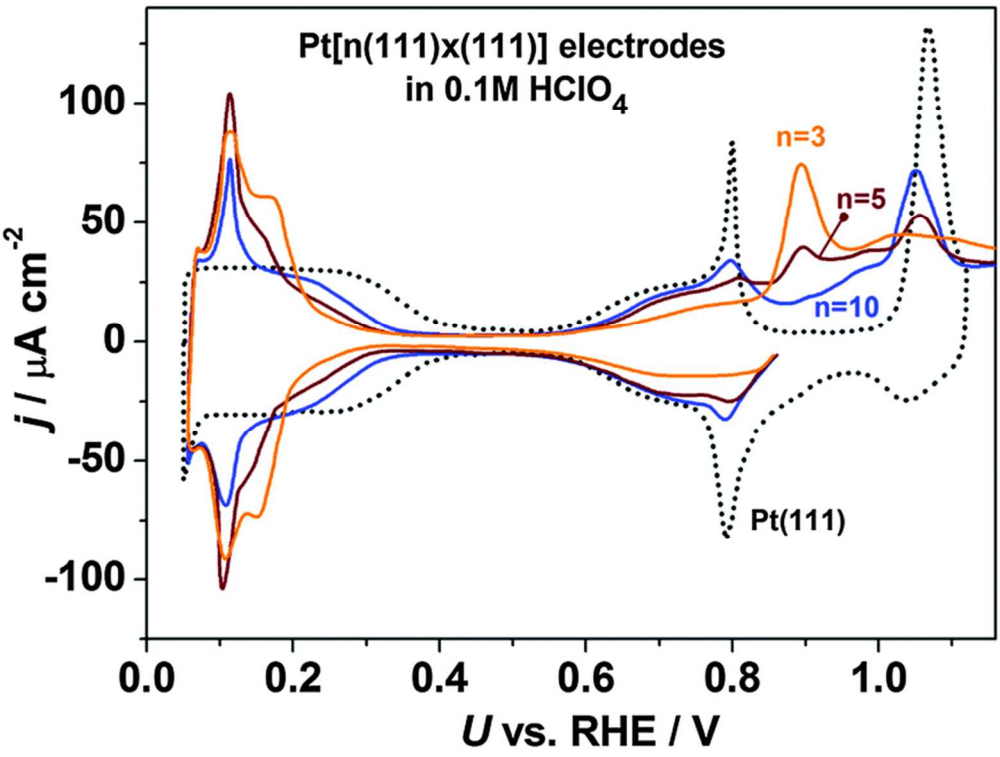

Figure 2
307x229mm (72 x 72 DPI)

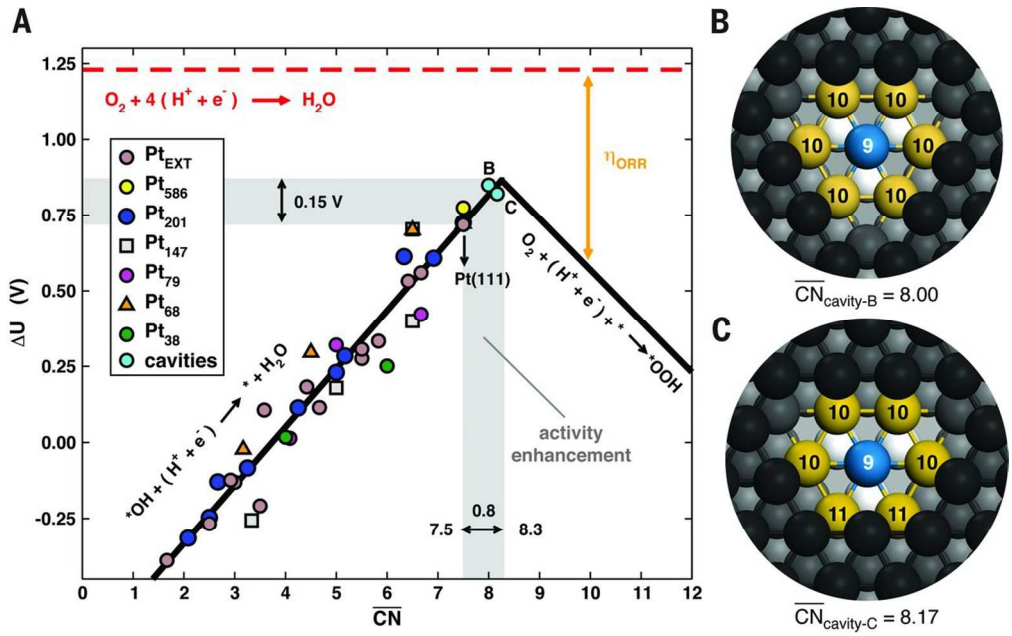

Figure 3
108x67mm (300 x 300 DPI)

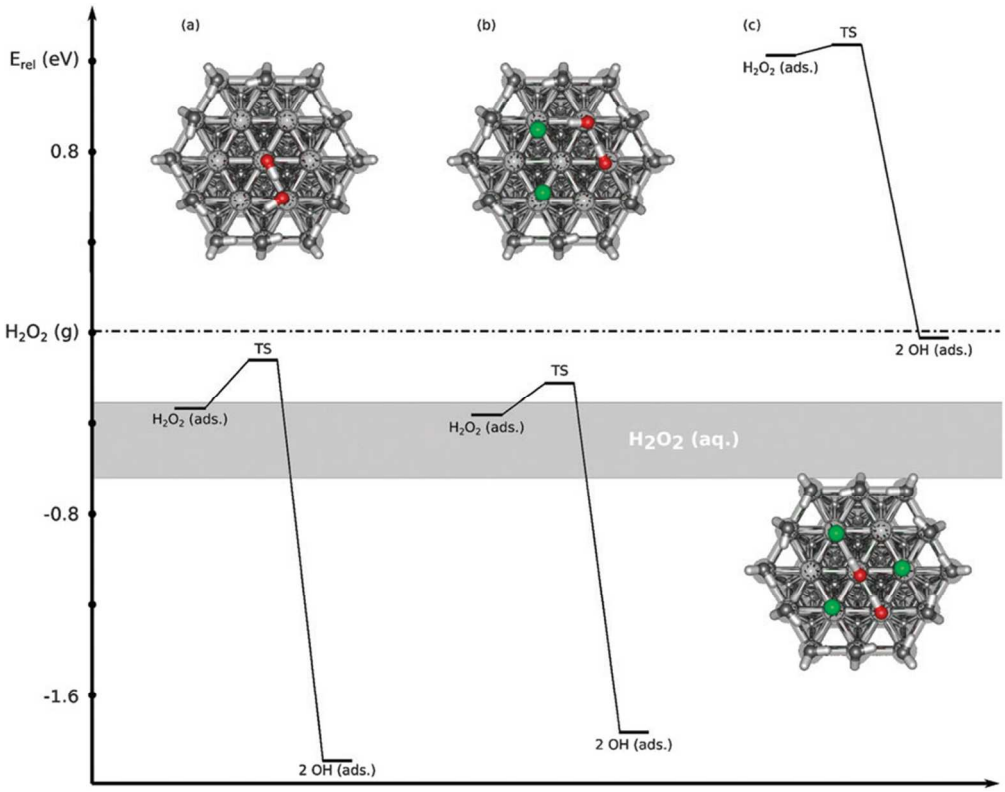

Figure 4
251x197mm (96 x 96 DPI)

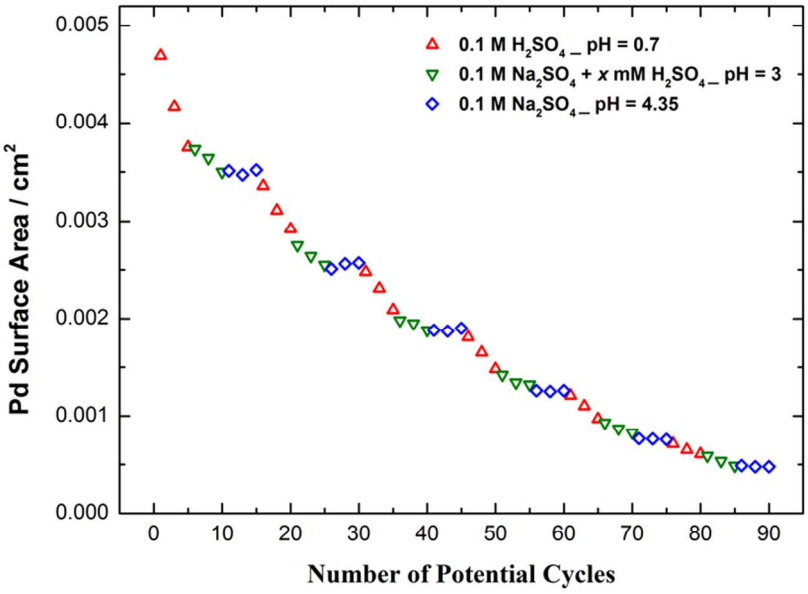

Figure 5
85x60mm (300 x 300 DPI)

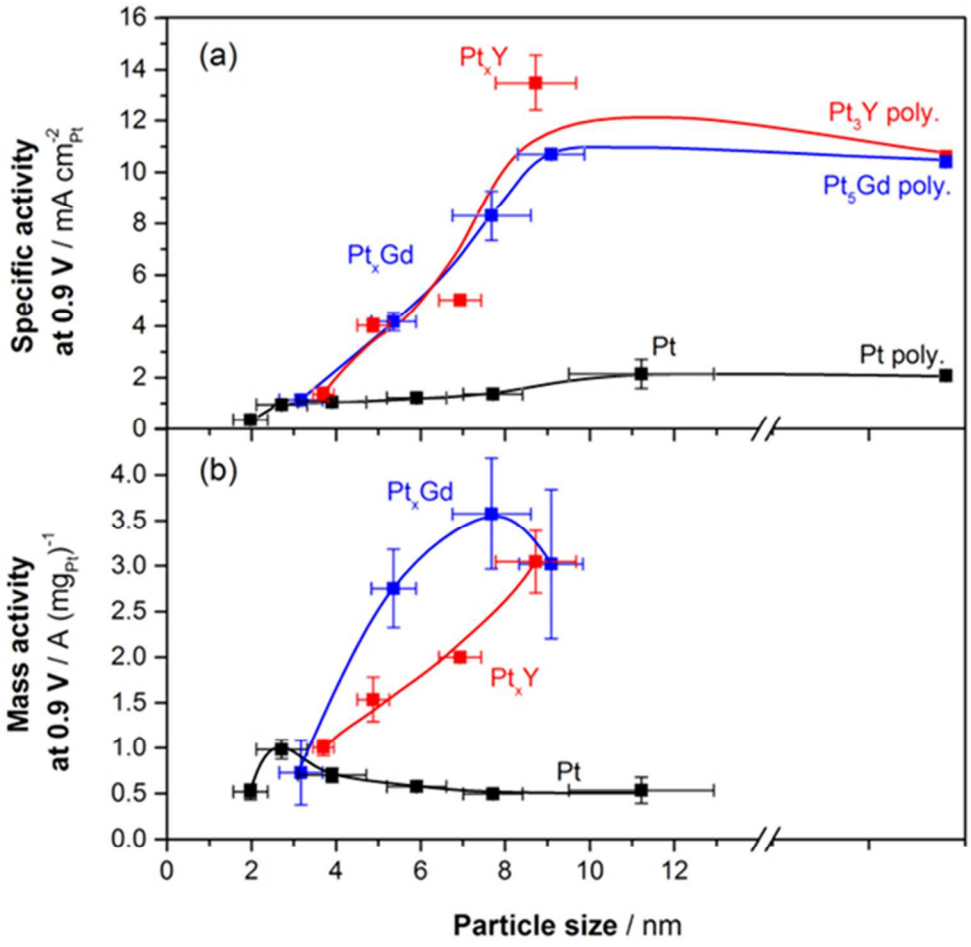

Figure 6
165x159mm (96 x 96 DPI)

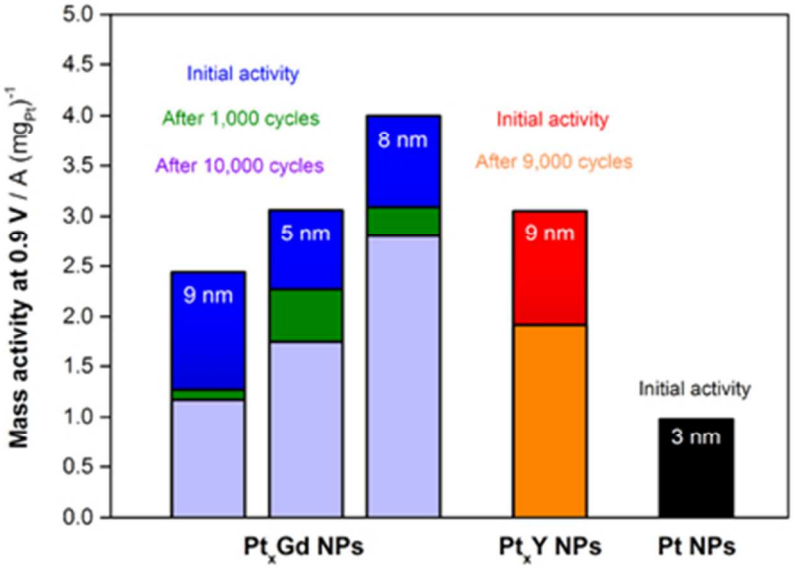

Figure 7
138x97mm (96 x 96 DPI)

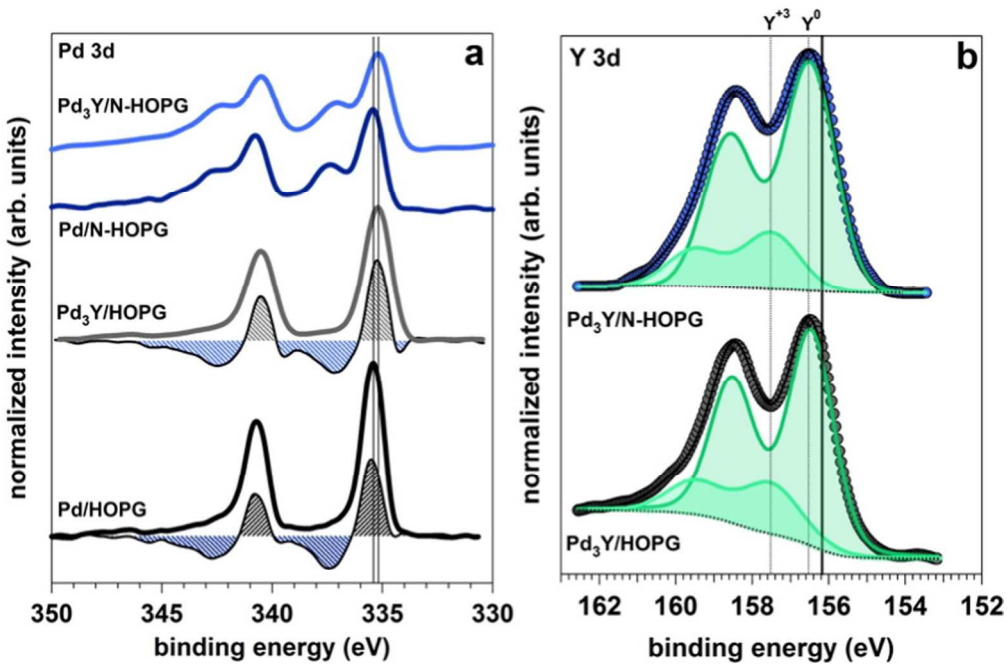

Figure 8
110x73mm (300 x 300 DPI)

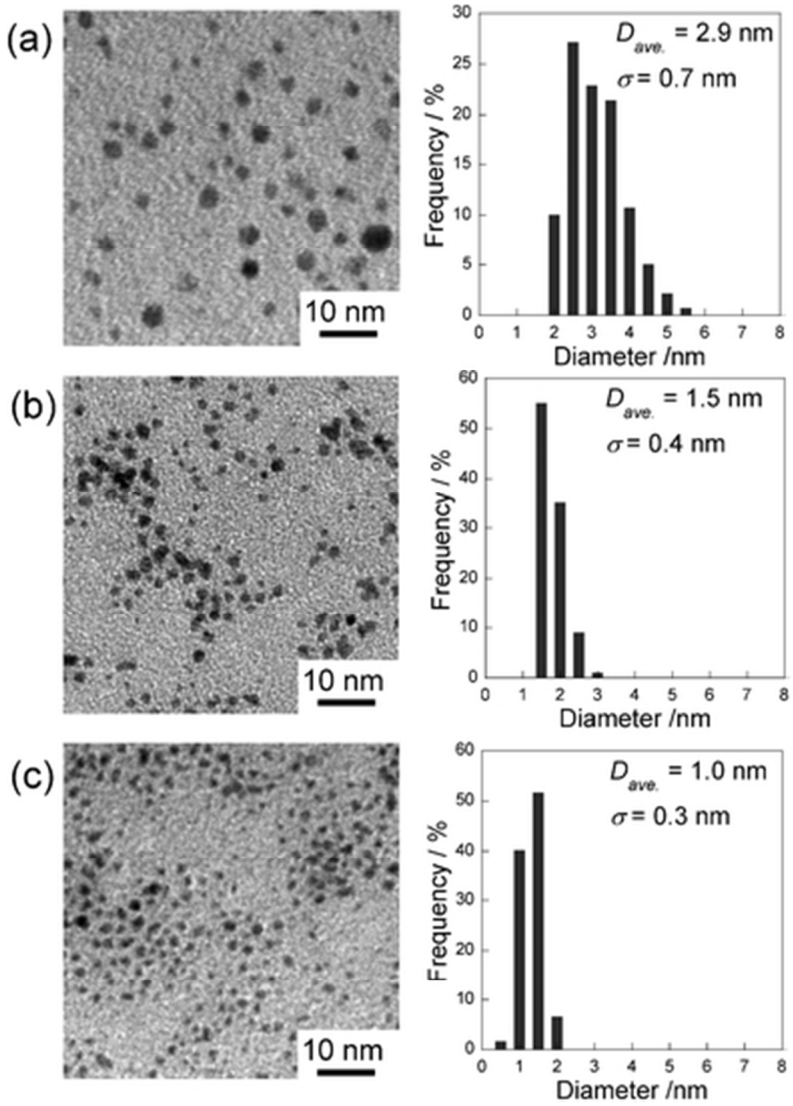

Figure 9
138x193mm (72 x 72 DPI)

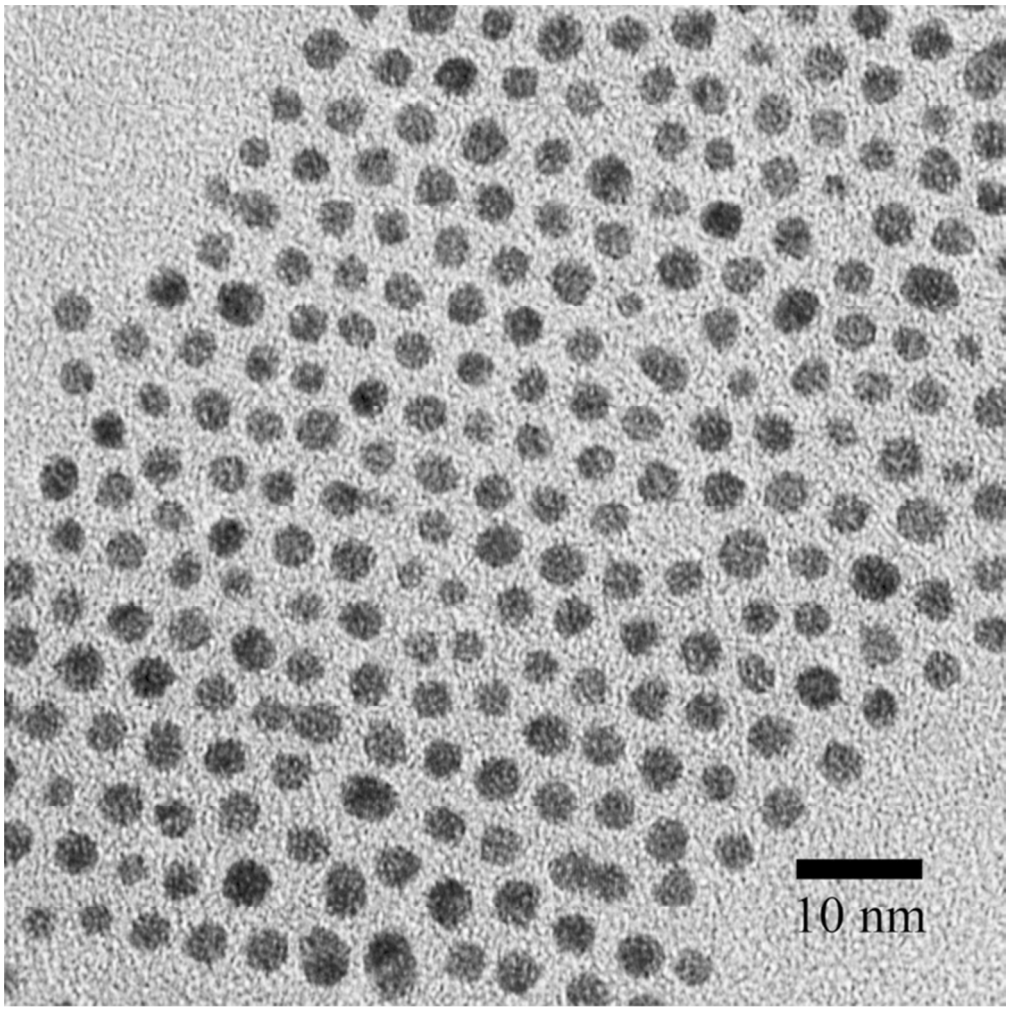

Figure 10
71x71mm (300 x 300 DPI)

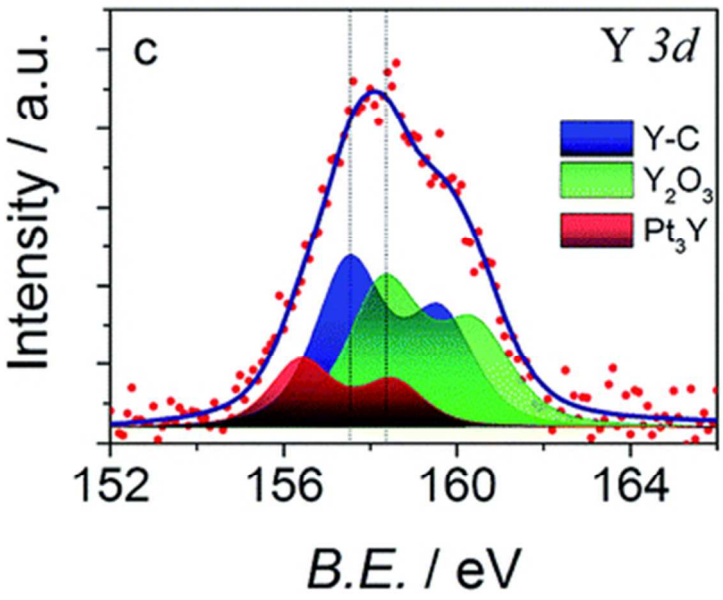

Figure 11
96x78mm (96 x 96 DPI)

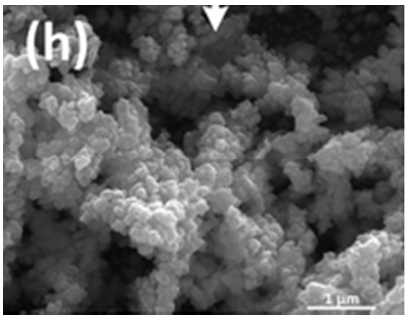

Figure 12
52x40mm (96 x 96 DPI)

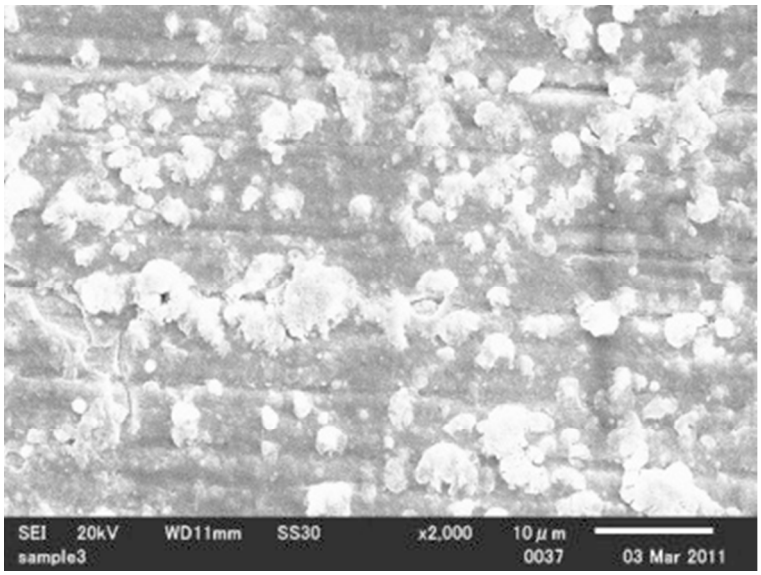

Figure 13
84x63mm (113 x 113 DPI)

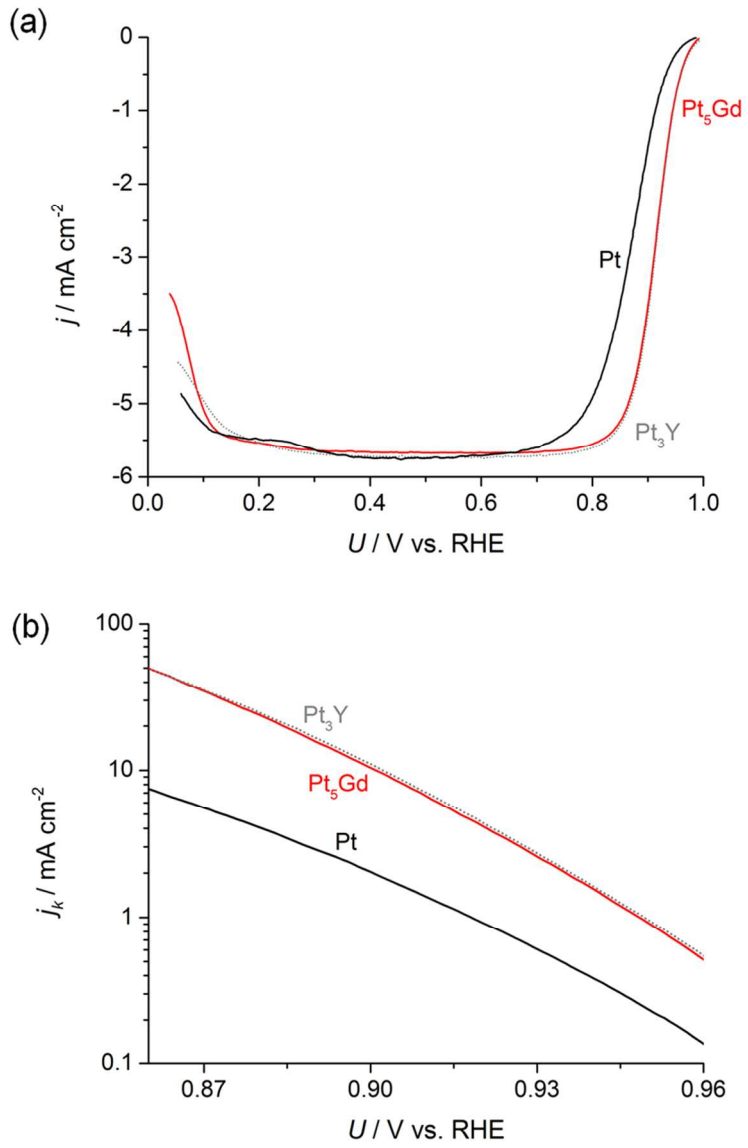

Figure 14
280x405mm (96 x 96 DPI)

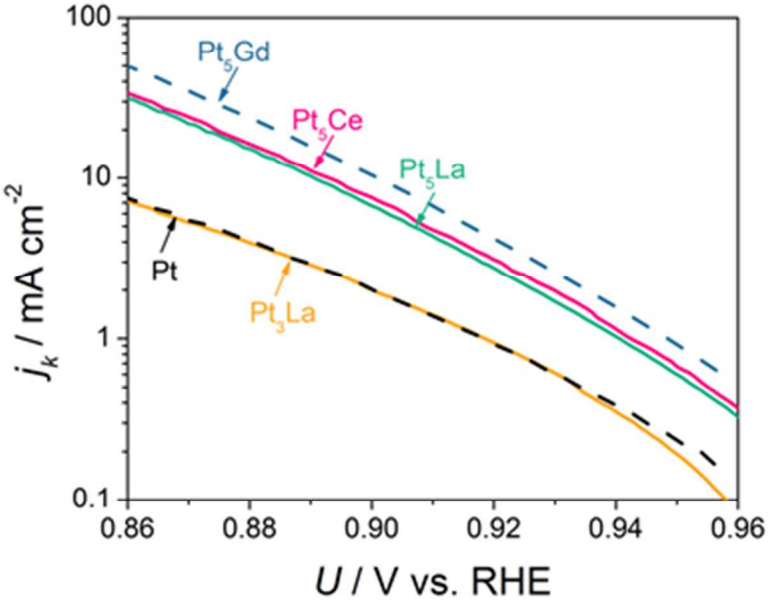

Figure 15
118x88mm (96 x 96 DPI)

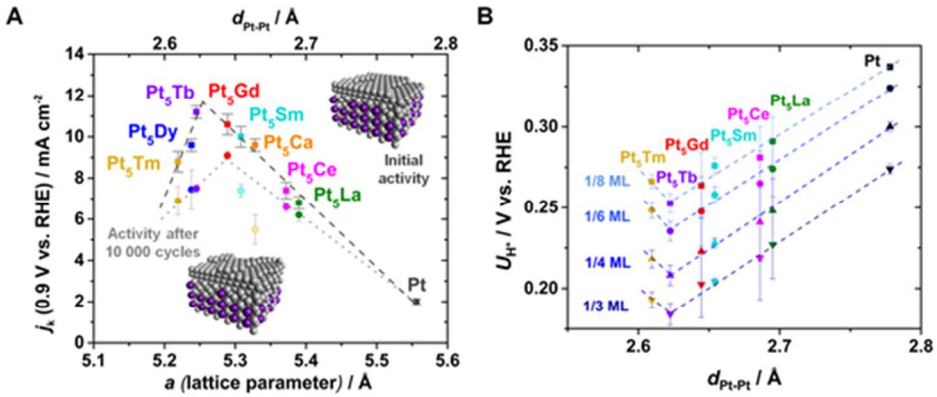

Figure 16
165x68mm (96 x 96 DPI)

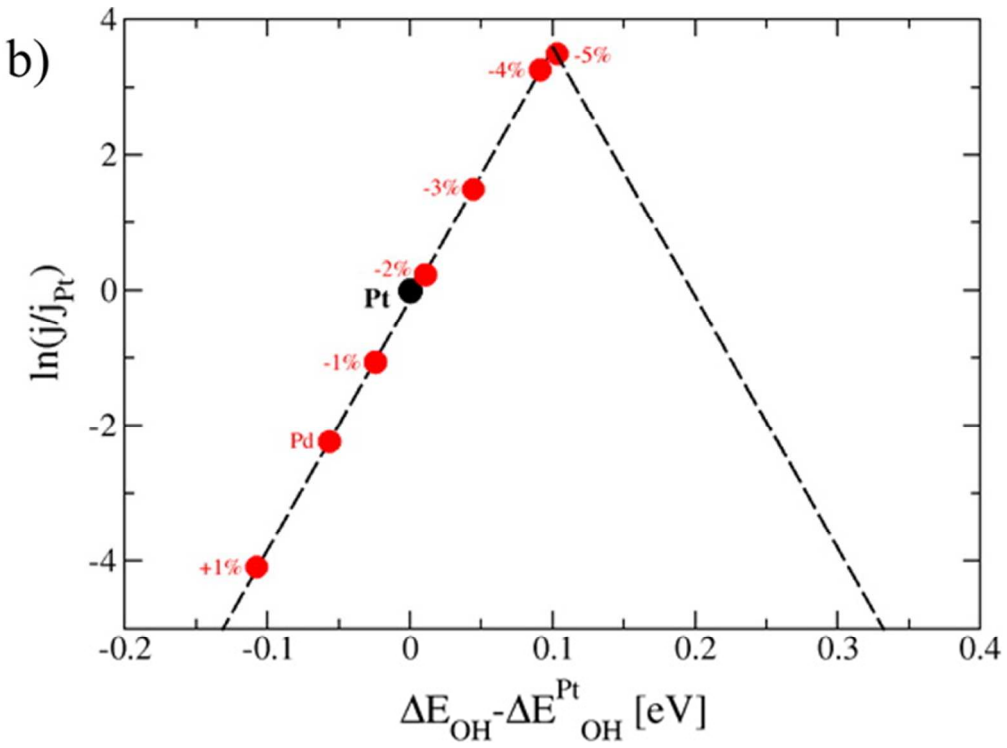

Figure 17
65x48mm (300 x 300 DPI)

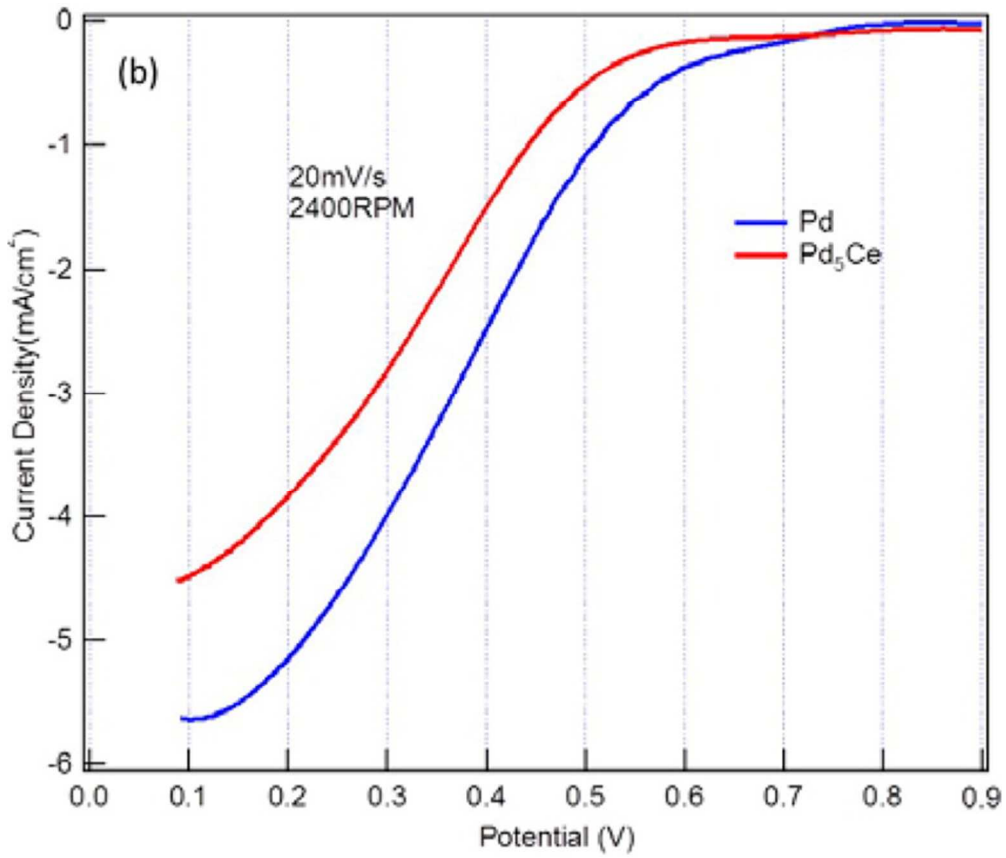

Figure 18
74x65mm (300 x 300 DPI)

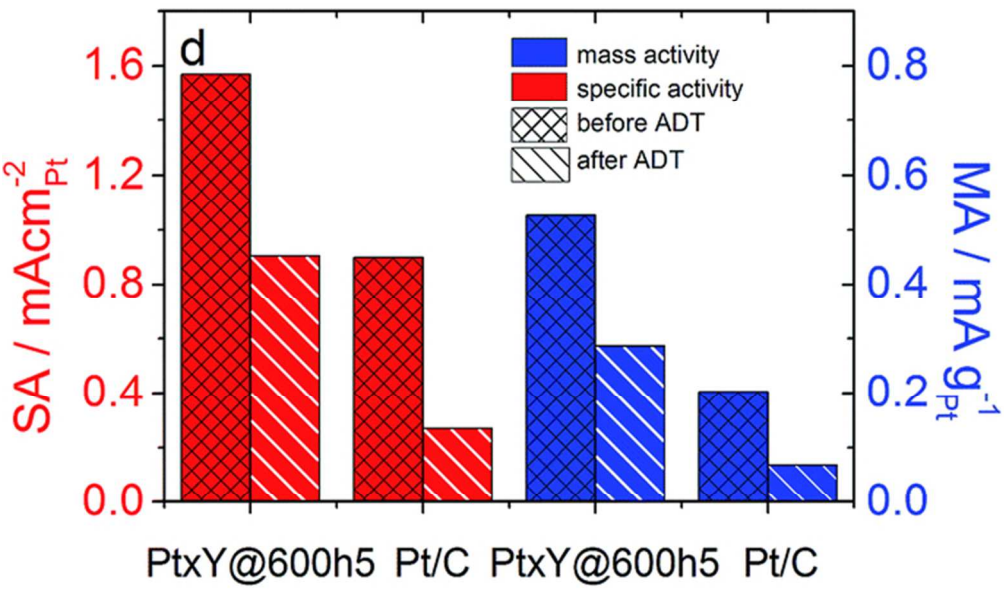

Figure 19
181x106mm (96 x 96 DPI)